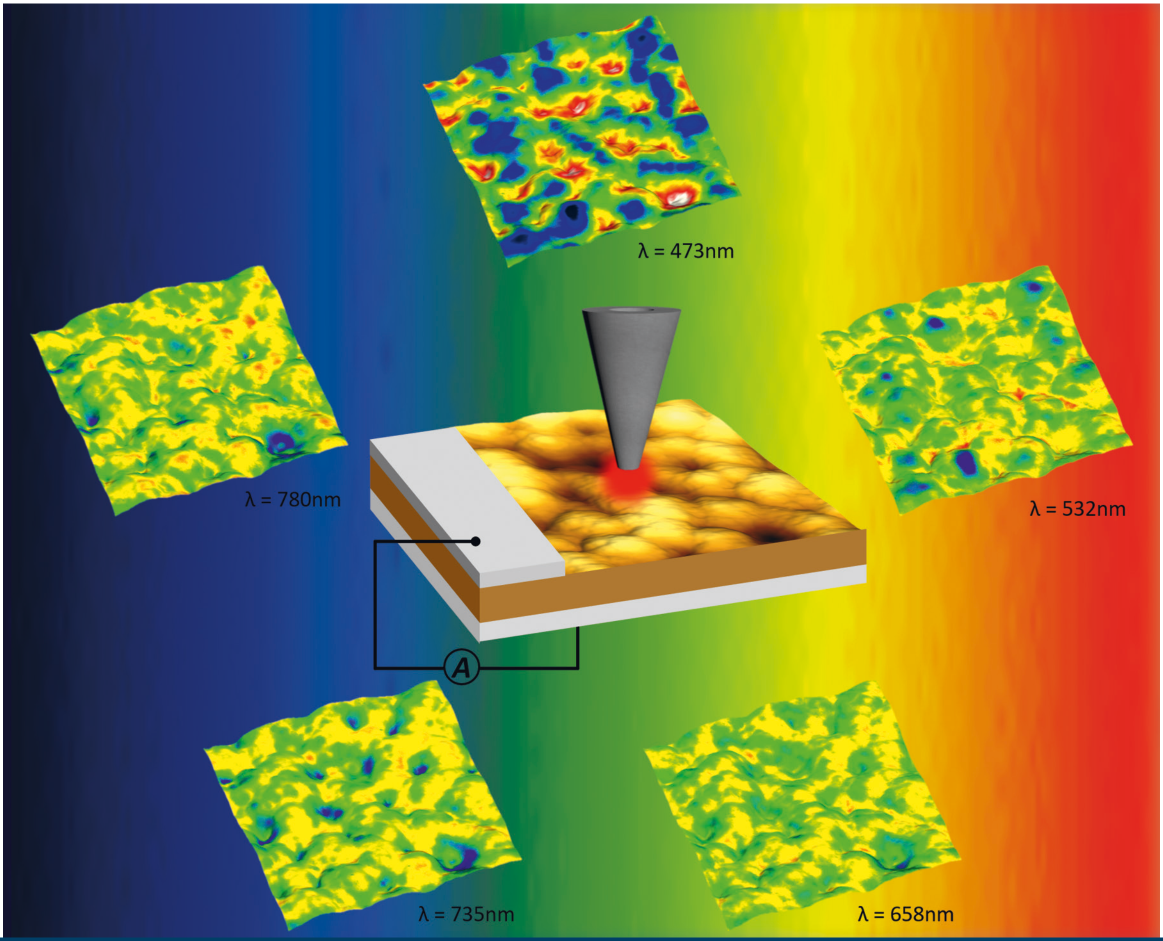

High-Resolution Photocurrent Mapping of Thin-Film Silicon Solar Cells Using Scanning Near-Field Optical Microscopy

Zhao Cao

Energie & Umwelt / Energy & Environment
Band / Volume 536
ISBN 978-3-95806-548-2

Mitglied der Helmholtz-Gemeinschaft

JÜLICH
Forschungszentrum

Schriften des Forschungszentrums Jülich
Reihe Energie & Umwelt / Energy & Environment Band / Volume 536

Forschungszentrum Jülich GmbH
Institut für Energie- und Klimaforschung
IEK-5 Photovoltaik

High-Resolution Photocurrent Mapping of Thin-Film Silicon Solar Cells Using Scanning Near-Field Optical Microscopy

Zhao Cao

Schriften des Forschungszentrums Jülich
Reihe Energie & Umwelt / Energy & Environment Band / Volume 536

ISSN 1866-1793 ISBN 978-3-95806-548-2

Bibliografische Information der Deutschen Nationalbibliothek.
Die Deutsche Nationalbibliothek verzeichnet diese Publikation in der
Deutschen Nationalbibliografie; detaillierte Bibliografische Daten
sind im Internet über http://dnb.d-nb.de abrufbar.

Herausgeber und Vertrieb: Forschungszentrum Jülich GmbH
Zentralbibliothek, Verlag
52425 Jülich
Tel.: +49 2461 61-5368
Fax: +49 2461 61-6103
zb-publikation@fz-juelich.de
www.fz-juelich.de/zb

Umschlaggestaltung: Grafische Medien, Forschungszentrum Jülich GmbH

Druck: Grafische Medien, Forschungszentrum Jülich GmbH

Schriften des Forschungszentrums Jülich
Reihe Energie & Umwelt / Energy & Environment, Band / Volume 536

D 82 (Diss. RWTH Aachen University, 2021)

ISSN 1866-1793
ISBN 978-3-95806-548-2

Vollständig frei verfügbar über das Publikationsportal des Forschungszentrums Jülich (JuSER)
unter www.fz-juelich.de/zb/openaccess.

Abstract

A solar cell is used to directly convert the sunlight into electrical energy. The key indicator for the performance of a solar cell, hence for its competitiveness compared with other forms of renewable energies is the conversion efficiency. The conversion efficiency of a solar cell strongly depends on its local optoelectronic properties, such as local light coupling efficiency or local material inhomogeneity, on the microscopic or even nanoscopic length scales. Therefore, an accurate understanding and assessment of the specific effects of these factors on the photogenerated current would provide valuable information for the improvement of the solar cell performance. This work presents local photocurrent measurements of various thin-film silicon solar cells with subwavelength spatial resolution by using an aperture-type scanning near-field optical microscope (a-SNOM) as the illumination source. The measurement method allows for direct access to the local optoelectronic properties. With the support of finite-difference time-domain (FDTD) simulations, their individual contributions to the photocurrent generation are analyzed.

Starting with the flat microcrystalline silicon (μc-Si:H) thin-film solar cell, the SNOM photocurrent measurements are conducted with five different wavelengths ranging from 473 nm to 780 nm. The measurement results show a distinct correlation between the local photocurrent signal and the local topography, which is observed for all wavelengths. Corresponding FDTD simulations with an idealized topography reveal that the origin of this correlation is the topography-dependent local light coupling efficiency, which can be $\sim 30\%$ higher at local topographic minimums than that at local topographic maximums. In addition, the effect of the light polarization on the local light coupling is investigated with a periodically textured amorphous silicon (a-Si:H) thin-film solar cell. Both, the SNOM photocurrent measurements and FDTD simulations show that, at topographic structures with high rotational asymmetry, the difference of the light coupling efficiencies can be as large as 30% between two perpendicular polarizations.

Next, SNOM photocurrent measurement results of the flat polycrystalline silicon (poly-Si) thin-film solar cell fabricated by liquid phase crystallization (LPC) are presented. Due to the absence of significant topographic structures, the measured photocurrent is mainly the result of the local material inhomogeneity: a grain boundary in the presented case. In order to derive information of characteristic electrical parameters, i.e. the minority carrier diffusion length L_D and the grain boundary recombination velocity S_gb, electrical simulations are performed and fitted to the photocurrent profiles extracted from the recorded photocurrent maps. The determined values, $L_\mathrm{D} = 4.6\,\mu\mathrm{m}$ and $S_\mathrm{gb} = 5.2 \times 10^5\,\mathrm{cm/s}$, are in good agreement with the figures found in other references.

The last investigated sample is a solar cell with more complex structure where both, topographic structures and local material inhomogeneity would have a considerable impact on the measured photocurrent: a randomly textured μc-Si:H thin-film solar cell. The corresponding SNOM photocurrent measurement results exhibit reversed correlations of the photocurrent signal to the local topography between short and long wavelengths: while this correlation remains the same for the short wavelengths as in the case of flat μc-Si:H thin-film solar cell, higher photocurrent signal is measured at local topographic maximum for long wavelengths. FDTD simulations with the real topography acquired from the atomic force microscopy predict however, still the same correlation for all wavelengths. This leads to the conclusion that, the reversed trend observed at long wavelengths is probably caused by the electrical defects below the surface, which are commonly formed at sharp micro-valleys, i.e. at local topographic minimums. As a consequence, the photocurrent response is strongly reduced at local topographic minimums, which results in the observed reversal of the correlation between the photocurent signal and local topography at long wavelengths.

This work clearly demonstrates the power of the SNOM photocurrent measurements for the nanoscale optoelectronic characterization of solar cells. In particular, the combination with supporting FDTD simulations facilitates the specific analysis of the individual effects of the local topography variations and the local material inhomogeneity on the photocurrent generation. Consequently, the presented techniques will allow for more specific, hence more efficient approaches when exploring concepts for the improvement of the solar cell efficiency.

Kurzfassung

Eine Solarzelle wird eingesetzt, um das Sonnenlicht direkt in elektrische Energie umzuwandeln. Ein Schlüsselindikator für die Leistung einer Solarzelle und somit für ihre Konkurrenzfähigkeit gegenüber anderen Formen der erneuerbaren Energien ist die Umwandlungseffizienz. Die Effizienz einer Solarzelle hängt stark von ihren lokalen optoelektronischen Eigenschaften, wie z. B. lokaler Lichteinkopplungseffizienz oder lokaler Materialinhomogenität, auf der mikroskopischen oder sogar nanoskopischen Längenskala ab. Daher wird ein genaues Verständnis und Assessment der spezifischen Effekte dieser Faktoren auf den photogenerierten Strom wertvolle Informationen zur Steigerung der Solarzellenleistung liefern. Diese Arbeit präsentiert Messungen des lokalen Photostroms an diversen Silizium-Dünnschichtsolarzellen mit Subwellenlängen-Auflösung, welche durch die Verwendung eines optischen Nahfeldmikroskops mit Aperturspitze (a-SNOM) als Beleuchtungsquelle realisiert wird. Die Messmethode ermöglicht den direkten Zugriff auf die lokalen optoelektronischen Eigenschaften, deren individuelle Beiträge zur Photostromerzeugung dann mithilfe der FDTD-Simulationen analysiert werden.

Mit der flachen mikrokristallinen Silizium-Dünnschichtsolarzelle (μc-Si:H) beginnend werden SNOM-Photostrommessungen mit fünf verschiedenen Wellenlängen von 473 nm bis 780 nm durchgeführt. Die Messergebnisse zeigen für alle Wellenlängen eine ausgeprägte Korrelation zwischen dem lokalen Photostromsignal und der lokalen Topographie. Entsprechende FDTD-Simulationen mit einer idealisierten Topographie führen diese Korrelation auf die topographieabhängige lokale Lichteinkopplungseffizienz zurück, welche an lokalen topographischen Minima $\sim 30\%$ höher sein kann als an lokalen topographischen Maxima. Zusätzlich wird der Effekt der Lichtpolarisation auf die lokale Lichteinkopplung mit einer periodisch texturierten amorphen Silizium-Dünnschichtsolarzelle (a-Si:H) untersucht. Sowohl die SNOM-

Photostrommessungen, als auch die FDTD-Simulationen ergeben, dass die Differenz der Lichteinkopplungseffizienzen zwischen zwei senkrechten Polarisationen an topographischen Strukturen mit hoher Rotationsasymmetrie bis zu 30% betragen kann.

Als nächstes werden die Ergebnisse der SNOM-Photostrommessungen von der flachen polykristallinen Silizium-Dünnschichtsolarzelle (poly-Si) vorgestellt, die mit der Flüssigphasen-Kristallisation hergestellt wurde. Aufgrund der vernachlässigbaren topographischen Strukturen ist der gemessene Photostrom hauptsächlich die Folge der lokalen Materialinhomogenität, in diesem Fall einer Korngrenze. Um Kenntnis über charakteristische elektrische Parameter, nämlich die Diffusionslänge L_D der Minoritätsträger sowie die Rekombinationsgeschwindigkeit S_gb an der Korngrenze, herzuleiten, werden elektrische Simulationen durchgeführt und an die aus den Messergebnissen extrahierten Photostromprofile angefittet. Die ermittelten Werte $L_\mathrm{D} = 4.6\,\mu\mathrm{m}$ und $S_\mathrm{gb} = 5.2 \times 10^5\,\mathrm{cm/s}$ stimmen gut mit den Zahlen aus der Literatur überein.

Die letzte untersuchte Probe ist eine Solarzelle mit komplexerer Struktur, wobei sowohl die topographischen Strukturen, als auch die lokale Materialinhomogenität einen erheblichen Einfluss auf den gemessenen Photostrom haben: eine stochastisch texturierte μc-Si:H Dünnschichtsolarzelle. Die dazugehörigen Ergebnisse der SNOM-Photostrommessungen weisen umgekehrte Korrelationen des Photostromsignals zu der lokalen Topographie zwischen kurzen und langen Wellenlängen auf: während diese Korrelation erhalten bleibt für kurze Wellenlängen wie im Falle von der flachen μc-Si:H Dünnschichtsolarzelle, wird nun höherer Photostrom gemessen an lokalen topographischen Maxima für lange Wellenlängen. FDTD-Simulationen mit der echten Topographie, die mit einem Rasterkraftmikroskop aufgenommen wurde, zeigen jedoch für alle Wellenlängen die gleiche Korrelation. Dies führt zu der Schlussfolgerung, dass die umgekehrte Korrelation bei langen Wellenlängen wahrscheinlich durch die elektrischen Defekte unter der Oberfläche hervorgerufen wird, welche häufig in den Mikro-Valleys, d. h. in lokalen topographischen Minima entstehen. Folglich wird das Photostromsignal an lokalen topographischen Minima stark reduziert, welches zu der beobachteten Umkehrung der Korrelation zwischen dem Photostromsignal und der lokalen Topographie bei langen Wellenlängen führt.

Diese Arbeit demonstriert deutlich die Leistungsfähigkeit der SNOM-Photostrommessungen für die nanoskalige optoelektronische Charakterisierung der Solarzellen. Insbesondere die Kombination mit unterstützenden FDTD-Simulationen erlaubt die spezifische Analyse der individuellen Auswirkungen der lokalen Änderungen der Topographie sowie der lokalen Materialinhomogenität auf der Photostromerzeugung. Folglich ermöglichen die präsentierten Methoden eine gezieltere, somit effizientere Herangehensweise bei der Erforschung nach Konzepten für die Steigerung der Solarzelleneffizienz.

Contents

1 Introduction

More than five decades after its first theoretical description by Synge [1], the aperture-type scanning near-field optical microscopy (a-SNOM) was experimentally realized at the beginning of the 1980s [2–4]. This provided a unique access to nanoscale characterization of a plethora of species. By bringing the aperture of the scanning probe to the proximity of the sample surface, subwavelength optical resolution, which is not limited by diffraction but only depends on the size of the aperture, is achieved. In combination with its non-invasive nature and the ability for the simultaneous recording of the topography image of the sample, a-SNOM has been successfully applied in a broad spectrum of scientific fields covering plasmonics [5–8], waveguiding [9–11], single molecule study [12–14], thin-film analysis [15–18], *etc.*

Compared to the scattering-type SNOM, where a sharp metallic probe is applied instead of the aperture probe [19, 20], the a-SNOM has the great advantage of providing local illumination through the aperture with nearly no background. This capability makes the a-SNOM a powerful tool for the characterization of a large number of optoelectronic materials and devices. By scanning an electrically contacted sample, photocurrent generated by the local irradiation can be detected and exactly attributed to the individual probe position, i.e. the local topography. In other words, local photocurrent measurements with a-SNOM as the illumination source, or SNOM photocurrent measurements for short, allow for the extraction of local optoelectronic information with sub-100 nm spatial resolution. So far, SNOM photocurrent measurements have been conducted to investigate a variety of electronic and photonic samples including semiconductor nanowires/nanorods [21–23], quantum well structures [24, 25] and graphene transistors [26, 27]. Optoelectronic devices, especially solar cells, are predestined for the characterization with SNOM photocurrent measurements. Firstly, the basic function of a solar cell is to convert electromagnetic radiation into electrical energy, i.e. to generate photocurrent upon light illumination. The working principle of the SNOM photocurrent measurement perfectly imitates that of the solar cell, with the major advantage that the measured photocurent signal primarily results from the local optoelectronic properties of illuminated spot. Moreover, the absorber of a solar cell, particularly those of thin-film solar cells, often comprise of materials with local inhomogeneities on the microscopic or even nanoscopic length scales. Potential origins of these local material inhomogeneities can be local variation of chemical composition, defects, local crystallinity or grain formation. The quality, i.e. the efficiency of a solar cell strongly depends on these local material properties. Therefore, SNOM photocurrent measurements of solar cells can provide valuable information for the improvement of solar cell efficiency by directly relating the optoelectronic performance of the solar cell to the local material properties.

Up to date, SNOM photocurrent measurements on a variety of solar cells have been reported [28–38]. Most of them focused their investigations on the relation between the photocurrent generation and the local material inhomogeneity. For instance, it was shown for organic solar cells that, micron-sized domains containing various chemical compositions exhibit large differences in the photocurrent signal [32, 33]. For CdS/CdTe and CdTe polycrystalline solar cells, enhancement of the photocurrent signal at grain boundaries due to local variation of the bandgaps was observed [28, 35]. However, local material inhomogeneity usually leads to local variation of the surface topography. For instance, grains are naturally formed during the growth of polycrystalline thin-film solar cells such as copper indium gallium selenide (CIGS) solar cells [36] or CdS/CdTe solar cells [35], which will cause surface roughness in the dimensions of the grain sizes. The effects of topographic features on the photocurrent signal have been rarely discussed so far. However, as will be demonstrated later, topographic features can have a significant impact on the local photocurrent signal, which might even oppose the contribution of the pure material inhomogeneity. The present work aims to achieve a good understanding of the individual influence of the local topography variation and the material inhomogeneity on the photocurrent response, which is essential for the accurate interpretation and evaluation of SNOM photocurrent measurement results. By separate studies of selected solar cells through both, experimental measurements and theoretical simulations, the respective effects of the topography variation and the material inhomogeneity are identified and explained. On this basis, the SNOM photocurrent measurement results of a solar cell with more complex structure, which contains contributions from both effects, are demonstrated and analyzed.

This thesis consists of six chapters. Following this introduction, Chapter 2 provides the theoretical basics for this work. Aside from the fundamentals of classical optics, basics of the near-field optics and solar cells are briefly illustrated. Chapter 3 gives an overview of the experimental setup and the simulation methods. Main components of the a-SNOM and extensions for the recording of the local photocurrent signal are introduced. The optical simulations base on the finite-difference time-domain (FDTD) method and are performed with a home-developed FDTD software. Chapter 4 focuses on the investigation of the effect of local topography on the photocurrent signal. Starting with the discussion of the SNOM photocurrent measurement results of a hydrogenated microcrystalline silicon (μc-Si:H) thin-film solar cell with minor topographic features, FDTD simulation results are presented and compared to the measurement results to solidify the interpretation of the measurement results. In addition, the effect of light polarizations with regard to the topographic features is discussed. Chapter 5 deals with the effect of local material inhomogeneity on the photocurrent signal. The sample used for the SNOM photocurrent measurement is a flat polycrystalline silicon thin-film solar cell fabricated by liquid phase crystallization (LPC). Furthermore, electrical simulations are performed where the results are fitted to the photocurrent signal in order to extract characteristic material parameters. Chapter 6 shows the SNOM photocurrent measurement results of a more complex sample, where both, the local topography and the local material inhomogeneity have a considerable contribution to the photocurrent signal: a μc-Si:H thin-film solar cell with distinctive, random surface texture. A discussion of the measurement results is given, where the insights gained from the previous chapters and the results from supporting FDTD simulations are taken into account. At last, Chapter 7 summarizes the main results and illustrates potential directions for future work.

2 Fundamentals

This chapter covers the theoretical basics for this work. Section 2.1 introduces fundamental theories of classical optics, which provide the basis for the understanding of the subsequent sections about near-field optics and solar cells. Starting with the Maxwell equations, expressions for light as electromagnetic waves are derived. Subsequently, refraction and absorption of light in medium are described. Afterwards, the phenomenon of evanescent waves is introduced and conditions for their generation are derived. Evanescent waves are of key relevance for the near-field optics which is briefly illustrated in Section 2.2. This section elucidates the origin of diffraction limit in far-field optics and explains how this limit can be overcome by the application of near-field optics. Finally, Section 2.3 gives an overview of the fundamental physical processes taking place in a solar cell. Particularly, the absorption coefficients of the absorber materials and the recombination mechanisms of charge carriers are described with special regards to silicon solar cells. At last, light trapping as an important concept for the increase of light absorptance in the absorber, hence solar cell efficiency is introduced.

2.1 Fundamentals of optics

2.1.1 Maxwell equations

The Maxwell equations are a set of coupled differential equations, which were developed by James Clerk Maxwell during the years 1861 – 1864 . The Maxwell equations constitute the fundamentals of the classical electrodynamics and are the foundation of many areas in physics, especially of optics. In differential form, the

Maxwell equations are written as [39–41]

$$\nabla \cdot \boldsymbol{D} = \rho \qquad \text{(Coulomb's law)} \tag{2.1a}$$

$$\nabla \cdot \boldsymbol{B} = 0 \tag{2.1b}$$

$$\nabla \times \boldsymbol{H} = \boldsymbol{J} + \frac{\partial \boldsymbol{D}}{\partial t} \qquad \text{(Ampère's law)} \tag{2.1c}$$

$$\nabla \times \boldsymbol{E} = -\frac{\partial \boldsymbol{B}}{\partial t} \qquad \text{(Faraday's law)} \tag{2.1d}$$

where $\boldsymbol{E}$ and $\boldsymbol{H}$ are the electric field and the magnetic field, respectively. $\boldsymbol{D}$ denotes the electric displacement, $\boldsymbol{B}$ the magnetic flux density, ρ the charge density and $\boldsymbol{J}$ the current density. The macroscopic fields $\boldsymbol{E}$ and $\boldsymbol{D}$ are connected to each other via the electric polarization $\boldsymbol{P}$ of the medium

$$\boldsymbol{D} = \epsilon_0 \boldsymbol{E} + \boldsymbol{P} \tag{2.2}$$

where $\epsilon_0 \approx 8.854 \times 10^{-12}\,\mathrm{F/m}$ denotes the vacuum permittivity. For linear and isotropic medium, $\boldsymbol{P}$ is parallel to $\boldsymbol{E}$ and can be written as $\boldsymbol{P} = \epsilon_0 \chi \boldsymbol{E}$, where χ denotes the electric susceptibility of the medium. Inserting into Eq. 2.2 yields the constitutive relation between $\boldsymbol{D}$ and $\boldsymbol{E}$

$$\boldsymbol{D} = \epsilon_0 (1+\chi) \boldsymbol{E} = \epsilon_0 \epsilon_r \boldsymbol{E} \tag{2.3}$$

where $\epsilon_r = 1 + \chi$ is referred to as the relative permittivity. Analogously, for the magnetic field, the following constitutive relation between $\boldsymbol{B}$ and $\boldsymbol{H}$ applies:

$$\boldsymbol{B} = \mu_0 (\boldsymbol{H} + \boldsymbol{M}) = \mu_0 (1 + \chi_M) \boldsymbol{H} = \mu_0 \mu_r \boldsymbol{H} \tag{2.4}$$

with $\mu_0 = 4\pi \times 10^{-7}\,\mathrm{H/m}$ denoting the vacuum permeability, χ_M the magnetic susceptibility of the medium, $\boldsymbol{M}$ the magnetization and μ_r the relative permeability. In a medium with non-zero conductivity σ, the relation between $\boldsymbol{J}$ and $\boldsymbol{E}$ can be expressed by [42]

$$\boldsymbol{J} = \sigma \boldsymbol{E} \tag{2.5}$$

The equations 2.3, 2.4 and 2.5 are also referred to as the material equations [42]. Furthermore, by forming the divergence of Eq. 2.1c and using the vector identity that the divergence of a curl is zero, one obtains

$$\nabla \cdot \boldsymbol{J} + \nabla \cdot \frac{\partial \boldsymbol{D}}{\partial t} = 0 \tag{2.6}$$

Inserting the Coulomb's law in Eq. 2.1a into the equation above yields the continuity equation

$$\boldsymbol{\nabla}\cdot\boldsymbol{J}+\frac{\partial\rho}{\partial t}=0 \tag{2.7}$$

which implies the charge conservation [39]

2.1.2 Electromagnetic plane waves

In the absence of sources, i.e. $\rho=0$ and $\boldsymbol{J}=0$, as in the case of an uncharged and nonconducting material, the Maxwell equations transform to

$$\boldsymbol{\nabla}\cdot\boldsymbol{D}=0 \tag{2.8a}$$

$$\boldsymbol{\nabla}\cdot\boldsymbol{B}=0 \tag{2.8b}$$

$$\boldsymbol{\nabla}\times\boldsymbol{H}=\frac{\partial\boldsymbol{D}}{\partial t} \tag{2.8c}$$

$$\boldsymbol{\nabla}\times\boldsymbol{E}=-\frac{\partial\boldsymbol{B}}{\partial t} \tag{2.8d}$$

Forming the curl on both sides of the Eq. 2.8d yields

$$\boldsymbol{\nabla}\times\boldsymbol{\nabla}\times\boldsymbol{E}=-\boldsymbol{\nabla}\times\frac{\partial\boldsymbol{B}}{\partial t}\overset{(2.4)}{=}-\mu_0\mu_r\boldsymbol{\nabla}\times\frac{\partial\boldsymbol{H}}{\partial t} \tag{2.9}$$

Applying Eq.2.8c in Eq. 2.9 and subsequently using Eq. 2.3 delivers

$$\boldsymbol{\nabla}\times\boldsymbol{\nabla}\times\boldsymbol{E}=-\epsilon_0\epsilon_r\mu_0\mu_r\frac{\partial^2\boldsymbol{E}}{\partial t^2} \tag{2.10}$$

With the vector identity

$$\boldsymbol{\nabla}\times\boldsymbol{\nabla}\times\boldsymbol{E}=\boldsymbol{\nabla}(\boldsymbol{\nabla}\cdot\boldsymbol{E})-\boldsymbol{\nabla}^2\boldsymbol{E} \tag{2.11}$$

and the fact that $\boldsymbol{\nabla}\cdot\boldsymbol{E}=0$ for the source-free case, one obtains

$$\boldsymbol{\nabla}^2\boldsymbol{E}-\epsilon_0\epsilon_r\mu_0\mu_r\frac{\partial^2\boldsymbol{E}}{\partial t^2}=0 \tag{2.12}$$

Analogously, a similar relation can be derived for the magnetic field:

$$\boldsymbol{\nabla}^2\boldsymbol{H}-\epsilon_0\epsilon_r\mu_0\mu_r\frac{\partial^2\boldsymbol{H}}{\partial t^2}=0 \tag{2.13}$$

Equation 2.12 and Eq. 2.13 have the form of a wave equation, which typically can be written as

$$\frac{\partial^2 y}{\partial x^2}-\frac{1}{v^2}\frac{\partial^2 y}{\partial t^2}=0 \tag{2.14}$$

for the one-dimensional case, where v denotes the phase velocity of the wave. By comparing Eq. 2.14 with Eq. 2.12 or Eq. 2.13, one obtains the phase velocity

$$v = \frac{1}{\sqrt{\epsilon_0 \epsilon_r \mu_0 \mu_r}} \tag{2.15}$$

for the electromagnetic wave. In case of vacuum, where $\epsilon_r = \mu_r = 1$, the phase velocity of the electromagnetic wave then becomes $v = \frac{1}{\sqrt{\epsilon_0 \mu_0}} \approx 2.998 \times 10^8\,\mathrm{m/s}$, which corresponds to the velocity of light c in vacuum. It was this identity, which brought Maxwell to the brilliant conclusion, that the light itself is an electromagnetic wave [43].

One solution of the wave equations is the plane wave. In case of the electric field $\boldsymbol{E}$, the solution can be written as [40]

$$\boldsymbol{E} = \boldsymbol{E}_0\, e^{i(kx - \omega t)} \tag{2.16}$$

for the one-dimensional case, where $\boldsymbol{E}_0$ denotes the amplitude of the wave, k is the wave vector, x is the propagation direction and ω denotes the angular frequency. The angular frequency is defined as $\omega = \frac{2\pi c}{\lambda}$, where c is the light velocity and λ denotes the light wavelength. By inserting the plane wave solution 2.16 into Eq. 2.14, the relation between the wave vector and the angular frequency, i.e. the wavelength is derived:

$$k = \frac{\omega}{v} \tag{2.17}$$

The energy flow of the electromagnetic wave is described by the Poynting vector

$$\boldsymbol{S} = \boldsymbol{E} \times \boldsymbol{H} \tag{2.18}$$

which is perpendicular to the electric field and the magnetic field. The absolute value of the Poynting vector $|\boldsymbol{S}|$ has the dimension of power per unit area ($\mathrm{W/m^2}$) and is equal to the intensity I of the electromagnetic wave. Furthermore, the intensity I is proportional to the square of the electric field $I \propto |\boldsymbol{E}|^2$ [40, 43].

2.1.3 Refractive index

The refractive index n of a medium is defined as the ratio of the light velocity c in vacuum and its phase velocity v in the medium [39,40]:

$$n = \frac{c}{v} \tag{2.19}$$

Inserting the phase velocity v from Eq. 2.15 and the light velocity in vacuum $c = \frac{1}{\sqrt{\epsilon_0 \mu_0}}$ into Eq. 2.19 yields

$$n = \sqrt{\epsilon_r \mu_r} \tag{2.20}$$

At optical frequencies, the relative permeability μ_r can be set to 1 [40], therefore the refractive index can be written as

$$n = \sqrt{\epsilon_r} \tag{2.21}$$

which relates the refractive index to the relative permittivity of a medium.

In general, the refractive index of a medium is a complex function of the angular frequency ω. In order to distinguish from the real part of the refractive index n, We introduce the complex refractive index $\tilde{n}$:

$$\tilde{n}(\omega) = n(\omega) + i\kappa(\omega) \tag{2.22}$$

where the real part n determines the phase velocity of light in the medium and the imaginary part κ, which is referred to as the extinction coefficient, is related to the absorption of light in the medium. The dependence of the refractive index on the light frequency is called dispersion. Due to the definition of the angular frequency, $\tilde{n}$ is also a function of the wavelength λ.

As the refractive index is a complex function, the relative permittivity ϵ_r is also complex according to Eq. 2.21:

$$\epsilon_r(\omega) = \epsilon_1(\omega) + i\epsilon_2(\omega) \tag{2.23}$$

Consequently, the relations between the quantities n, κ, ϵ_1 and ϵ_2 can be explicitly calculated as [40]

$$\epsilon_1 = n^2 - \kappa^2 \tag{2.24a}$$

$$\epsilon_2 = 2n\kappa \tag{2.24b}$$

$$n = \frac{1}{\sqrt{2}}(\epsilon_1 + \sqrt{\epsilon_1^2 + \epsilon_2^2})^{1/2} \tag{2.24c}$$

$$\kappa = \frac{1}{\sqrt{2}}(-\epsilon_1 + \sqrt{\epsilon_1^2 + \epsilon_2^2})^{1/2} \tag{2.24d}$$

If the imaginary part ϵ_2 of the complex relative permittivity is set to 0, the equations 2.24c and 2.24d are reduced to

$$n = \sqrt{\epsilon_1} \tag{2.25a}$$

$$\kappa = 0 \tag{2.25b}$$

which describes a purely refractive, non-absorbing medium.

2.1.4 Absorption

In an absorbing optical medium, the attenuation $\mathrm{d}I(x)$ of light within the propagation distance $\mathrm{d}x$ is described by [40]

$$-\mathrm{d}I(x) = \alpha(\lambda)\mathrm{d}x\, I(x) \tag{2.26}$$

where $I(x)$ denotes the light intensity at position x and $\alpha(\lambda)$ denotes the absorption coefficient of the medium. $\alpha(\lambda)$ quantifies the fraction of power absorbed by the medium in a unit length and usually strongly depends on the light wavelength λ. For simplicity, the explicit dependence of α on λ is omitted in the following discussion.

The integration of Eq. 2.26 yields Lambert-Beer law [40, 41]:

$$I(x) = I_0\, e^{-\alpha x} \tag{2.27}$$

where I_0 denotes the light intensity at position $x = 0$. The reciprocal of α is called the absorption length L_{abs}, which is the characteristic length, where the light intensity is attenuated by a factor of e.

As mentioned above, the imaginary part of the complex refractive index $\tilde{n}$, i.e. the extinction coefficient κ, is related to the absorption of light in the medium, therefore also related to the absorption coefficient α. This relation is derived in the following according to [40].

The wave vector k in Eq. 2.17 can be written as

$$k = \tilde{n}\,\frac{\omega}{c} = (n + i\kappa)\,\frac{\omega}{c} \tag{2.28}$$

by using Eq. 2.19 for an absorbing medium with the complex refractive index $\tilde{n}$. Inserting Eq. 2.28 into the electric field in Eq. 2.16 yields

$$\boldsymbol{E} = \boldsymbol{E}_0\, e^{-\kappa\,\frac{\omega}{c}\,x}\, e^{i(n\,\frac{\omega}{c}x - \omega t)} \tag{2.29}$$

The intensity of the electromagnetic wave is proportional to the square of the electric field, accordingly:

$$I(x) \propto \boldsymbol{E}_{\boldsymbol{0}}^2\, e^{-2\kappa\,\frac{\omega}{c}\,x} \tag{2.30}$$

where the factor $2\kappa\,\frac{\omega}{c}$ defines the decaying constant of the intensity $I(x)$. Comparing this equation with Lambert-Beer law yields

$$\alpha = 2\kappa\,\frac{\omega}{c} = \frac{4\pi}{\lambda}\,\kappa \tag{2.31}$$

consequently, κ is directly proportional to the absorption coefficient α.

2.1.5 Evanescent waves

The propagation of light from one medium with the refractive index n_i into another medium with the refractive index n_r is described by the Snell's law [42]

$$\sin\theta_i n_i = \sin\theta_r n_r \tag{2.32}$$

where θ_i denotes the angle of incidence in the medium with n_i and θ_r denotes the refraction angle of the light in the medium with n_r, respectively. Figure 2.1 illustrates the propagation of light from the medium n_i into the medium n_r in the xz-plane with the respective incidence angle and refraction angle. In the depicted case, the medium with n_i is optically denser than the medium with n_r, i.e. $n_i > n_r$. It is then obvious from the Snell's law that $\theta_r > \theta_i$. Furthermore, the interface of the two media is set at the plane $z = 0$.

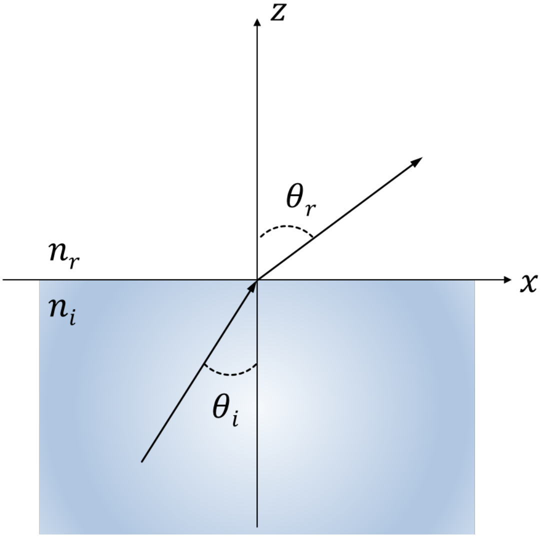

Figure 2.1: Sketch illustrating the Snell's law. The light propagates from one medium with the refractive index n_i into another medium with the refractive index n_r, with θ_i being the incidence angle and θ_r being the refraction angle, respectively.

According to the Snell's law, a critical incidence angle $\theta_{i,0}$ exists, so that θ_r becomes $\pi/2$, i.e. the light is not transmitted into the optically less dense medium, but propagates parallel to the interface. This critical angle is easily determined as

$$\theta_{i,0} = \arcsin\left(\frac{n_r}{n_i}\right) = \arcsin n_{ri} \tag{2.33}$$

where $n_{ri} = \frac{n_r}{n_i}$ is introduced for simplification.

In case of $n_i \approx 1.5$ for glass and $n_r \approx 1$ for air, the critical angle for the incident light at the glass/air-interface accounts for roughly 41.8 °. For incidence angles exceeding the critical angle $\theta_{i,0}$, the light cannot enter the optically thinner medium and is fully reflected at the interface. This phenomenon is therefore referred to as the total internal reflection (TIR). We then obtain [42]

$$\sin\theta_r = \frac{\sin\theta_i}{n_{ri}} \tag{2.34a}$$

$$\cos\theta_r = \pm i\sqrt{\frac{\sin^2\theta_i}{n_{ri}^2} - 1} \tag{2.34b}$$

using $\sin^2\theta_r + \cos^2\theta_r = 1$ and the condition $\sin\theta_i \,/\, n_{ri} > 1$ for $\theta_i > \theta_{i,0}$.

Now, recall that the electric field of a plane wave has the form

$$\boldsymbol{E} = \boldsymbol{E}_0\, e^{i(\boldsymbol{kr}-\omega t)} \tag{2.35}$$

where $\boldsymbol{kr} = k_x x + k_z z = k\sin\theta_r\, x + k\cos\theta_r\, z$ in the xz-plane. Inserting the equations in 2.34 into $\boldsymbol{kr}$ then yields

$$\boldsymbol{kr} = k\,\frac{\sin\theta_i}{n_{ri}}\,x \pm i\,k\,z\sqrt{\frac{\sin^2\theta_i}{n_{ri}^2} - 1} \equiv k\,\frac{\sin\theta_i}{n_{ri}}\,x \pm i\beta\, z \tag{2.36}$$

where we set $k\sqrt{\sin^2\theta_i / n_{ri}^2 - 1} \equiv \beta$ for simplification. Consequently, the electric field can be written as

$$\boldsymbol{E} = \boldsymbol{E}_0\, e^{-\beta z}\, e^{i(k\,\frac{\sin\theta_i}{n_{ri}}\,x - \omega t)} \tag{2.37}$$

where the solution with $e^{+\beta z}$ is omitted as it is unphysical.

According to Eq. 2.37, in case of a total internal reflection, the light wave is propagating along the interface in x-direction, while it decays exponentially in z-direction, i.e. in the optically less dense medium beyond the interface. This exponentially decaying wave is referred to as the evanescent wave. The quantity $\beta = k\sqrt{\sin^2\theta_i / n_{ri}^2 - 1}$ corresponds to the decay constant of the electric field. Furthermore, the penetration depth of the electric field into the optically less dense medium, defined as $\delta = \frac{1}{\beta}$, can be calculated as

$$\delta = \frac{1}{k\sqrt{\sin^2\theta_i / n_{ri}^2 - 1}} = \frac{\lambda_0}{2\pi\, n_r}\,\frac{1}{\sqrt{\sin^2\theta_i / n_{ri}^2 - 1}} = \lambda_0 \cdot \frac{1}{2\pi\sqrt{n_i^2 \sin^2\theta_i - n_r^2}} \tag{2.38}$$

where the relations $n_{ri} = \frac{n_r}{n_i}$ and $k = \frac{2\pi\, n_r}{\lambda_0}$ are used and λ_0 denotes the light wavelength in vacuum.

Equation 2.38 indicates that the penetration depth of the electric field into the optically less dense medium decreases with increasing incidence angle, as well as with increasing difference of the refractive indices between the two media. Moreover, although varying with the refractive indices and the incidence angle, the penetration depth is approximately of the order of a wavelength. Therefore, the evanescent field is also referred to as the near-field. As an example, for the total internal reflection of light at the glass/air-interface with an incidence angle of 45° (critical angle $\theta_{i,0} = 41.8\,^{\circ}$), the penetration depth accounts only for $\approx 0.45\,\lambda_0$. Furthermore, following the relationship between the intensity and the electric field $I \propto |\boldsymbol{E}|^2$, the intensity decays twice as fast as the electric field.

Although the electric field penetrates into the second medium, there is, however, no net energy transport across the interface. This can be proven by calculating the z-component of the time-averaged Poynting vector $\langle \boldsymbol{S} \rangle_z$, which yields 0 [39, 42, 44]. However, if a third medium with an appropriate refractive index n_3 is brought into the range of the evanescent field of the second medium, the evanescent waves can be partly converted into propagating radiation in the third medium upon interaction with the third medium [43–45]. This effect is referred to as the frustrated total internal reflection (FTIR). For a layer system with three media with the respective refractive index n_1, n_2 and n_3, arranged as in Fig. 2.2, the conditions for FTIR to occur are [44]

$$\begin{aligned} n_2 < n_3 < n_1 \qquad & \text{for the refractive indices} \\ \arcsin\left(\frac{n_2}{n_1}\right) < \theta_i < \arcsin\left(\frac{n_3}{n_1}\right) \qquad & \text{for the incidence angle } \theta_i \end{aligned} \tag{2.39}$$

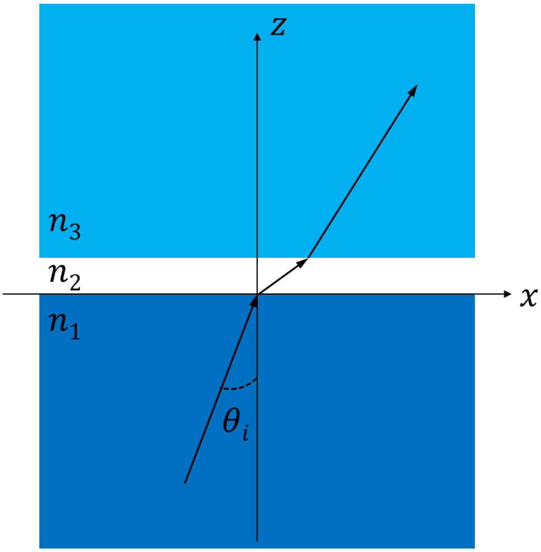

Figure 2.2: Sketch illustrating a layer system of three different media with the refractive indices n_1, n_2 and n_3, respectively. The light propagates in the medium n_1 and strikes the interface of medium n_1 and medium n_2 with angle of θ_i. If the relations between n_1, n_2, n_3 and θ_i satisfy the equations in 2.39, and the gap width between medium n_1 and n_3 is within the decay length of the evanescent waves in medium n_2, the light undergoes a frustrated total internal reflection.

Under FTIR, energy can be transported across the gap from medium n_1 to medium n_3, which is an analog to the electron-tunneling through a potential barrier in the quantum mechanics. These propagating waves, which contain subwavelength spatial optical information from the evanescent field, can then be detected in the far-field. The scattering of evanescent waves into propagating radiation by immersing a medium with appropriate refractive index into the near-field is the fundamental effect exploited in the a-SNOM, where specially prepared scanning probes are used to achieve the conversion. However, the transmitted energy strongly decreases with increasing gab distance and vanishes almost completely after a few wavelengths [44]. Therefore, in SNOM measurements, the scanning probes are kept at subwavelength distances to the sample surface with special distance regulation techniques (cf. Section 3.2).

2.2 Beyond diffraction limit: fundamentals of near-field optics

2.2.1 Diffraction limit

In 1665, Grimaldi described diffraction as the “deviation of light from rectlinear propagation” for the first time [46]. It occurs when the light encounters an obstacle or an aperture in an opaque plane. This behavior of light is attributed to its wave nature and can be explained by the Huygens-Fresnel principle [42,43]: every point of a wavefront can be considered as the origin of a secondary elementary wave, which interfere with each other. Upon hitting on an obstacle, parts of the wavefront change their phase or amplitude, which then results in diffraction of the light.

Depending on the relative geometry of the optical system, two regimes of diffraction can be distinguished. The characteristic parameter describing this relative geometry is called the Fresnel number [47]:

$$F = \frac{a^2}{R\lambda} \tag{2.40}$$

where a denotes the size of the diffracting aperture or obstacle, λ the light wavelength and R the distance between the diffracting object and the image plane. For $F \ll 1$, e.g. in case of large R, the regime is referred to as the far-field diffraction or the Fraunhofer diffraction, for $F \geq 1$, e.g. in case of small R, the regime is referred to as the near-field[1] diffraction or Fresnel diffraction.

In conventional optical microscopy, Fraunhofer diffraction plays a much more important role than the Fresnel diffraction. The diffraction pattern, i.e. the intensity distribution can be derived by evaluating the Fresnel-Kirchhoff diffraction integral under the Fraunhofer approximation ($F \ll 1$) [39, 42]. For the special case of a circular aperture, which is of the greatest interest with regard to the operating principle of optical instruments, the intensity distribution of a point source on an

---

[1] Note that the term “near-field” used in this context is not the same as the one described in Section 2.1.5, where the near-field specifically represents the evanescent field.

image plane in the far-field is described by [43]

$$I(\alpha) = I_0 \left[\frac{2\, J_1(k\, r\, \sin\alpha)}{k\, r\, \sin\alpha} \right]^2 \tag{2.41}$$

where J_1 denotes the first order Bessel function, k the wave number, r the radius of the circular aperture and α the opening angle between k and the central optical axis ($\alpha = 0$). The resulting diffraction pattern is referred to as the Airy pattern, which is depicted in Fig. 2.3. The bright disc in the center is called the Airy disk, which is surrounded by alternate, concentric dark and bright rings. Note that the intensity is plotted on a logarithmic scale.

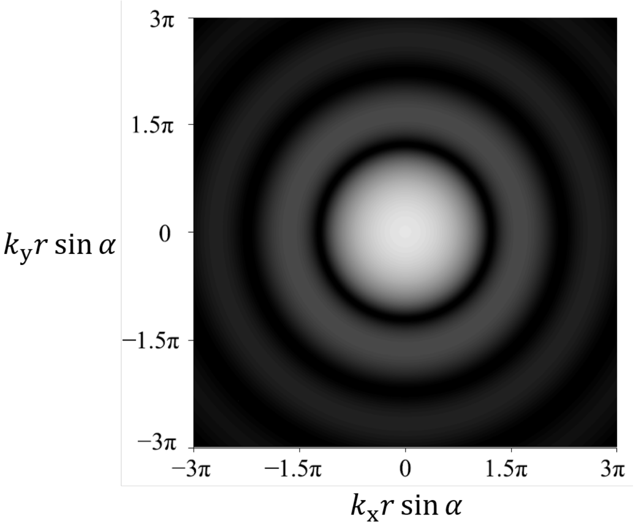

Figure 2.3: Image of the Airy pattern, which illustrates the typical intensity distribution of a point source on the image plane after Fraunhofer diffraction by a circular aperture. The intensity is plotted on a logarithmic scale. Reproduced from [48]

According to Rayleigh [49, 50], two point sources are still unambiguously resolved if their minimum distance is such that the center of the Airy disc of first point source just coincides with the first minimum of the Airy pattern of the second point source. As a consequence, the resolution d_{min} can be calculated as [42]

$$d_{\text{min}} = 0.61\, \frac{\lambda}{NA} \tag{2.42}$$

where $NA = n\sin\alpha$ denotes the numerical aperture of the optical system, e.g. of the objective in case of a conventional far-field microscope. A similar expression for the resolution was obtained by Abbe, where the object is not treated as luminous point sources, but as a diffraction grating illuminated by plane waves [51]

$$d_{\min} = \frac{\lambda}{2NA} \tag{2.43}$$

Aside from a constant factor, both Abbe and Rayleigh derived an optical resolution which is limited by diffraction. One can increase the optical resolution by increasing the numerical aperture or using light with shorter wavelengths. However, the resolution is always limited at the order of half of a wavelength. For visible light, the optical resolution lies approximately in the range of $200\,\mathrm{nm} - 500\,\mathrm{nm}$.

2.2.2 Angular spectrum representation

In the angular spectrum representation, optical fields can be described as the superposition of plane waves and evanescent waves with variable amplitudes and propagation directions [44]. For an arbitrary electric field $\boldsymbol{E}(x,y,z)$ with an arbitrarily chosen z-axis, the two-dimensional Fourier transform $\hat{\boldsymbol{E}}(k_x,k_y,z)$ in the plane $z =$ constant and the corresponding inverse Fourier transform are [44]

$$\hat{\boldsymbol{E}}(k_x,k_y;z) = \frac{1}{4\pi^2}\iint\limits_{-\infty}^{\infty} \boldsymbol{E}(x,y,z)\, e^{-i(k_x x + k_y y)}\,\mathrm{d}x\,\mathrm{d}y \tag{2.44}$$

and

$$\boldsymbol{E}(x,y,z) = \iint\limits_{-\infty}^{\infty} \hat{\boldsymbol{E}}(k_x,k_y z)\, e^{i(k_x x + k_y y)}\,\mathrm{d}k_x\,\mathrm{d}k_y \tag{2.45}$$

where (k_x,k_y) are the corresponding spatial frequencies to the Cartesian coordinates (x,y).

Furthermore, for a time-harmonic electric field in free space, the Helmholtz equation applies:

$$(\nabla^2 + k^2)\boldsymbol{E}(x,y,z) = 0 \tag{2.46}$$

By using the Helmholtz equation on Eq. 2.45 and defining

$$k^2 \equiv k_x^2 + k_y^2 + k_z^2 \tag{2.47}$$

one obtains the following relation:

$$\hat{\boldsymbol{E}}(k_x,k_y;z) = \hat{\boldsymbol{E}}(k_x,k_y;0)\, e^{\pm ik_z z} \tag{2.48}$$

Equation 2.48 shows that, by multiplying the two-dimensional Fourier spectrum of the electric field in an object plane $z = 0$ by the term $e^{\pm ik_z z}$, one obtains the two-dimensional Fourier spectrum in the image plane $z = \text{constant}$. Hence, the term $e^{\pm ik_z z}$ is referred to as the “propagator” in reciprocal space [44]. Finally, inserting Eq. 2.48 into Eq. 2.45 yields

$$\boldsymbol{E}(x,y,z) = \iint\limits_{-\infty}^{\infty} \hat{\boldsymbol{E}}(k_x,k_y;0)\, e^{i(k_x x + k_y y \pm k_z z)}\, \mathrm{d}k_x\, \mathrm{d}k_y \tag{2.49}$$

which is angular spectrum representation of the electrical field $\boldsymbol{E}(x,y,z)$.

From the definition of k in Eq. 2.47, it is obvious that, depending on the sign of k_z^2, i.e. the values of k_x and k_y, k_z can be either real or imaginary. As a consequence, two characteristic solutions with the respective Fourier components are obtained [44]:

$$e^{i(k_x x + k_y y)}\, e^{\pm i|k_z|z}, \qquad k_x^2 + k_y^2 \leq k^2 \tag{2.50a}$$

$$e^{i(k_x x + k_y y)}\, e^{-|k_z||z|}, \qquad k_x^2 + k_y^2 > k^2 \tag{2.50b}$$

Equation 2.50a depicts oscillating functions, which correspond to plane waves that propagate to the far-field, while Eq. 2.50b describes exponentially decaying functions, which correspond to evanescent waves that are localized in the near-field. Together with Eq. 2.47, we can conclude that the higher the spatial frequencies k_x and k_y are, the larger the value of $|k_z|$ becomes, which results in a faster decay of the evanescent waves. Since the subwavelength details of objects are stored in the high spatial frequencies, i.e., in the evanescent fields [52, 53], the subwavelength optical information cannot reach the far-field. This is the fundamental origin of the diffraction limit of the optical resolution in classical far-field microscopy.

2.2.3 Near-field optics and SNOM

The diffraction limit does not constitute the fundamental limit of the optical resolution, but rather arises from the applied optics. According to the Heisenberg uncertainty principle, the relation between the bandwidth of the spatial frequency $\Delta k_{\|}$ and the spatial confinement $\Delta r_{\|}$ obeys [44, 54]

$$\Delta k_{\|}\,\Delta r_{\|} \geq 1 \tag{2.51}$$

where $\|$ denotes the transverse components of $\boldsymbol{k}$ and $\boldsymbol{r}$, which comprise of (k_x, k_y) or (x, y), respectively. Following Eq. 2.51, the broader the bandwidth of spatial frequencies is, the better the spatial confinement will be. Theoretically, unlimited spatial resolution is achievable with infinite bandwidths. However, as elucidated in Section 2.2.2, the access to high spatial frequencies requires access to the evanescent fields, which is the subject of near-field optics.

Near-field optics studies non-propagating inhomogeneous fields, i.e. evanescent electromagnetic waves and their interaction with matter [54, 55]. An essential tool for the study of near-field optics is the <u>s</u>canning <u>n</u>ear-field <u>o</u>ptical <u>m</u>icroscope (SNOM). The basic concept of a SNOM is to use a subwavelength aperture or tip, which is approached to the sample surface within the range of the evanescent fields, to increase the bandwidth of spatial frequencies, consequently surmounting the diffraction limit. The optical resolution is then no longer limited by the wavelength, but only depends on a characteristic length parameter [44]. In case of the a-SNOM, the optical resolution is primarily determined by the aperture diameter.

Synge proposed as the first one an experimental scheme, which forms the basis for an a-SNOM, in 1928 [1]. In his illustration, optical resolution beyond the diffraction limit is achieved by illuminating a tiny hole with 100 nm diameter in a thin, opaque metal film, thereby turning the tiny hole into a nanometric light source. In 1944, Bethe first developed a rigorous theory for the diffraction of light through a subwavelength circular hole in a metal screen [56]. In order to derive an analytical solution for the field distributions near the tiny aperture, Bethe made the idealized assumption of an infinitely thin and perfectly conducting metal screen. Errors in Bethe's theory were later corrected by Bouwkamp in 1950 [57]. According to the Bethe-Bouwkamp model, for normal incidence of plane waves, the calculated transmission efficiency η after normalization to the aperture area reads [41, 58]

$$\eta = \frac{64}{27\pi^2}\,(kr)^4 \propto (\frac{r}{\lambda_0})^4 \tag{2.52}$$

where r denotes the aperture radius and λ_0 the vacuum wavelength of the light.

The scaling with $(r/\lambda_0)^4$ indicates that for a subwavelength aperture with $r \ll \lambda_0$, the total transmission is expected to be very weak and drops further rapidly with increasing wavelengths.

Due to the idealizations made in the Bethe-Bouwkamp model, it does not accurately describe the reality, where the metal has a finite thickness and finite conductivity. Therefore, further improvements of the model have been made during the years by various researchers to describe more realistic systems [59–62]. However, even for a real metal with finite thickness, the Bethe-Bouwkamp model still delivers a good qualitative description of the characteristic features of the near- and far-field distribution [55, 63].

2.3 Fundamentals of the solar cell

A solar cell generates photocurrent when it is illuminated with light. However, between “light in” and “current out”, a series of complex physical processes takes place in the solar cell. The diagram in Fig. 2.4 depicts the relevant physical processes contributing to the generation of the photocurrent in a solar cell: upon illumination of the solar cell, light couples into the absorber material. While the light propagates within the solar cell, the photons with an energy $\hbar\omega$ above the band gap E_g of the absorber material are absorbed, upon which charge carriers (electrons and holes) are generated. The charge carriers are then separated by the built-in electric field and travel to the contacts with the corresponding polarity, respectively. Charge carriers which do not recombine during the transport can reach the contacts and be extracted there as charge current.

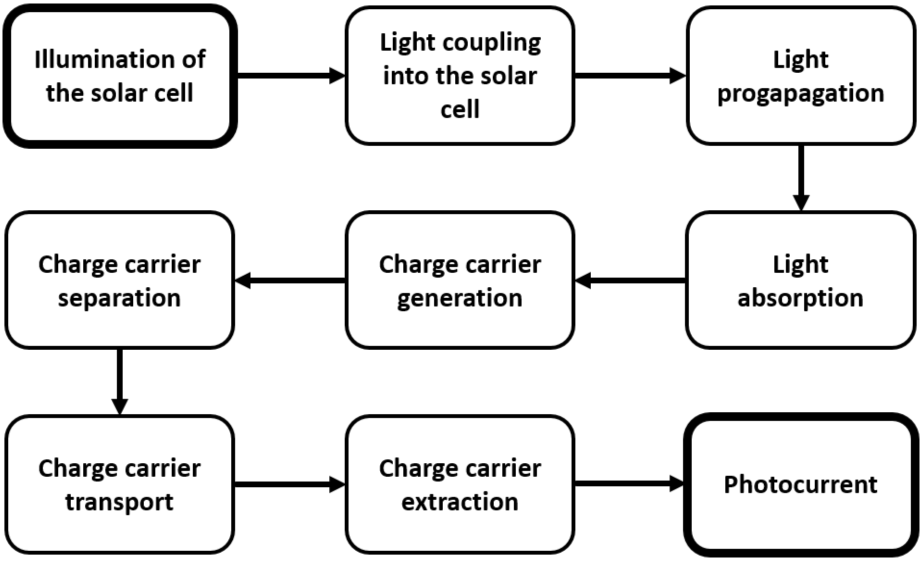

Figure 2.4: Schematic diagram showing the essential physical processes contributing to the generation of photocurrent in a solar cell upon light illumination.

The basic device physics of a solar cell can be described by the continuity equation [64]

$$\frac{\partial n(\boldsymbol{r})}{\partial t} = \frac{1}{q}\boldsymbol{\nabla}\cdot J(\boldsymbol{r}) + G - R \tag{2.53}$$

where $n(\boldsymbol{r})$ denotes the minority charge carrier density, q the elementary charge, $J(\boldsymbol{r})$ the charge current density, G the volume generation rate and R the volume recombination rate of the charge carriers. The charge current is the sum of the drift current and the diffusion current:

$$J(\boldsymbol{r}) = q\mu n F + q D \nabla n \tag{2.54}$$

where μ denotes the charge carrier mobility, F the electric field and D the diffusion coefficient.

2.3.1 Basics of silicon solar cell

A solar cell converts electromagnetic radiation (light) into electrical energy. The most suitable, hence predominantly used material in a solar cell are semiconductors. Semiconductors are primarily characterized by their band gap E_g, which denotes the energy difference between the maximum of the valence band and the minimum of the conduction band[2]. Especially semiconductors with band gaps lying between $1.1 - 1.4\,\mathrm{eV}$, matching the maximum range of the solar spectrum, constitute the optimum candidates for photovoltaic materials [68]. Among all appropriate semiconductors, silicon is the most widely applied photovoltaic material owing to its many advantages, such as abundance, non-toxicity, stability and a nearly ideal band gab of $1.12\,\mathrm{eV}$ [69]. Furthermore, silicon has been thoroughly studied for decades due to its relevance for the microelectronics industry, hence it is both scientifically and technically very advanced. With the first reported silicon solar cell reaching an efficiency of 6% in 1954 [70, 71], today, it dominates the photovoltaic market with a record efficiency of 26.7% [72, 73] and a market share of over 95% [74].

Among the different types of silicon solar cells, the crystalline silicon (c-Si) solar cell provides the highest efficiencies. In thin-film silicon solar cells, hydrogenated microcrystalline silicon (μc-Si:H) and hydrogenated amorphous silicon (a-Si:H) are used as the absorber materials. Thin-film silicon solar cells are mostly fabricated applying plasma-enhanced chemical vapor deposition (PECVD) techniques [75]. Despite the lower record efficiencies of 10.2% for single-junction a-Si:H and 11.9% for single-junction μc-Si:H [73], thin-film silicon solar cells have the advantages of less material consumption, lower processing temperature and simplified large-area production processes, *etc.*

Typically, c-Si solar cells utilize the p-n junction to realize the built-in electric field, where the n-type emitter is created *via* dopant diffusion on the p-type base, while p-i-n or n-i-p geometry is implemented in μc-Si:H or a-Si:H thin-film solar cells [64]. Both geometries are easily achieved by depositing the correspondingly doped or intrinsic layers in the desired order. A description of the specific layer structure of the solar cells studied in this work is provided in the respective chapters.

---

[2] For more details about semiconductor band theory please refer to [65–67]

2.3.2 Absorption coefficients of silicon materials

Figure 2.5 depicts the absorption coefficient of c-Si, μc-Si:H and a-Si:H as a function of the photon energy. Due to its indirect band gap[3], c-Si has a relatively low absorption coefficient, especially near the band gap $E_\mathrm{g} = 1.12\,\mathrm{eV}$ [68, 69]. In order to fully absorb the photons from the solar spectrum with energies $\hbar\omega > E_\mathrm{g}$, a c-Si absorber needs to be more than 100 µm thick without absorption-enhancement measures [76].

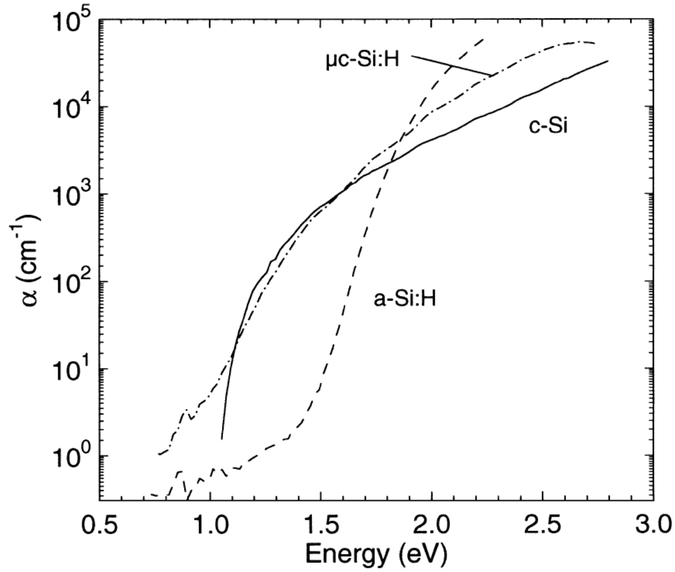

Figure 2.5: The absorption coefficient of crystalline silicon (c-Si), microcrystalline silicon (μc-Si:H) and amorphous silicon (a-Si:H) as a function of the photon energy. Reprinted from [77], Copyright (2000), with permission from Elsevier.

Contrary to the single crystalline Si where the Si atoms are well-arranged in a tetrahedral crystal structure, the amorphous Si does not possess a long-range order. Although most of the Si atoms retain the covalent bonds to four other Si atoms,

---

[3] the maximum of the valence band and the minimum of the conduction band are not located at the same position in the crystal momentum space

the bond lengths and bond angles vary from atom to atom. Si atoms coordinated to only three neighboring atoms leave a valence orbital unsatisfied, which forms the so-called dangling bond [78, 79]. The lack of long-range order in a-Si:H leads to an absorption behavior similar to that of a direct semiconductor [64, 76], which is reflected in the steep rise of the absorption coefficient of a-Si:H at its band gap of $\sim 1.7\,\text{eV}$ in Fig. 2.5. In the visible range of the solar spectrum, the absorption coefficient of the a-Si:H exceeds that of the c-Si by an order of magnitude.

The microcrystalline silicon is a heterogeneous system consisting of crystalline and amorphous phases. The volume fraction and distribution of both phases, as well as the sizes of the crystallites strongly depend on the deposition conditions [77,80,81]. The size of the crystallites can vary between a few tens to a few hundred nanometers. The absorption coefficient of μc-Si:H is rather similar to that of c-Si. Particularly in the infrared range ($\hbar\omega < 1.7\,\text{eV}$, i.e. $\lambda > 700\,\text{nm}$), μc-Si:H has a significantly higher absorption coefficient compared to that of a-Si:H.

2.3.3 Recombination mechanisms

Charge carriers are generated upon light absorption in the solar cell absorber, those which recombine with their counterparts during the transport are lost and do not contribute to the photocurrent. Upon recombination, a pair of electron and hole is annihilated and the energy set free is transferred to another particle (photon, electron, hole, phonons). Essentially, three types of recombination can be distinguished: radiative recombination, Auger recombination and Shockley-Read-Hall (SRH) recombination [64].

Radiative recombination, where an electron reacts with a hole and produces a photon, is the reverse process of light absorption. Therefore, the recombination rate is proportional to the product of the electron density n and the hole density p [76]:

$$R_{\text{rad}} = Bnp \tag{2.55}$$

where B denotes the radiative recombination coefficient. Radiative recombination is a fundamental physical process that is present in all photovoltaic absorbers, therefore it constitutes an upper limit to the minority carrier lifetime, consequently to the solar cell efficiency [82].

Auger recombination is a non-radiative recombination process involving three carries. Upon annihilation of an electron and a hole, the energy set free is transferred to a third carrier as kinetic energy which subsequently dissipates to the lattice by excitation of phonons. Therefore, the Auger recombination rate is proportional to the product of three carrier densities [76]:

$$R_{\text{Auger}} = C_n p n^2 + C_p p^2 n \tag{2.56}$$

where C_n and C_p denote the Auger recombination coefficients. Auger recombination typically occurs in doped materials with relatively low band gaps. It is the dominant loss mechanism in high-quality c-Si.

Shockley-Read-Hall recombination describes a non-radiative recombination process caused by trap states in the band gap [83, 84]. Deep trap states form recombination centers for both electrons and holes. The origins of these trap states are usually defects in the crystal structure or extrinsic impurities. The dangling bonds in amorphous silicon are a typical example of recombination centers, the saturation of dangling bonds can be achieved by incorporation of hydrogen (a-Si:H) [85]. Further examples of SRH-recombination centers are dislocations, misplaced atoms or vacancies, which are commonly found at grain boundaries in polycrystalline silicon materials (cf. Chapter 5). Due to the more complex nature of the SHR-recombination, the recombination rate is not merely a function of the carrier densities, but also depends on the properties of the trap states.

Among the three recombination mechanisms, while radiative recombination and Auger recombination occur due to fundamental physical processes in the intrinsic material and belong to the category of unavoidable recombination processes, SRH-recombination is a consequence of imperfect material, therefore it belongs to the category of avoidable recombination processes, which are the predominant ones in real semiconductors [64]. Accordingly, the reduction or elimination of losses caused by SRH-recombination, i.e. defect-assisted recombination, is of crucial importance for the design and fabrication of high-efficiency solar cells and remains a key research topic in the development of photovoltaic materials.

2.3.4 Light trapping

Aside from the already mentioned advantages of thin-film solar cells in Section 2.3.1, the small absorber thickness also posts a necessity in case of rather defect-rich absorber materials such as μc-Si:H or a-Si:H. Due to the enhanced recombination of charge carriers at the defects, a short travel distance is required for the charge carriers to reach the contacts. However, due to the weak absorption of silicon, the incident light cannot be fully absorbed within the usual thicknesses of a single junction μc-Si:H (a few µm) or a-Si:H (a few hundred nm) thin-film solar cell.

In order to achieve the maximum possible light absorptance while maintaining the benefits of a thin absorber, light management concepts such as light trapping are developed and implemented on thin-film solar cells. Light trapping refers to the strategy of prolongation of light path inside the absorber layer by applying back reflector, and particularly, light scattering textures. A variety of such textures has been extensively studied and applied on solar cells, such as pyramids [86–88], periodic nanotextures [89–94], random textures [95, 96], *etc.*

The main goal of introducing light trapping textures is to scatter the incident light into the absorber layer at large angles, which entails two beneficial effects: (i) the scattered light travels a longer distance than the sheer layer thickness for each passage. (ii) The back-reflected light can undergo total internal reflections at the front-surface texture, hence remains “trapped” inside the absorber layer.

Yablonovitch derived an upper limit for the increase of the average light path length in the absorber material under the conditions of weak absorption coefficient and isotropic light distribution in the absorber layer (as can be realized with randomized textures) [97, 98]:

$$\langle l \rangle_{\max} = 4n^2 d \tag{2.57}$$

where $\langle l \rangle$ denotes the average light path length, n the refractive index of the absorber material and d the thickness of the absorber. In other words, the maximum achievable enhancement of light absorption by implementing randomized textures accounts for $4n^2$ compared to the case of a planer absorber without back reflector. In case of intrinsic silicon, this translates to an enhancement factor of ~ 50 for photon energies near the band edge of 1.12 eV.

3 Methods

This chapter introduces both, the experimental and the simulation methods used in this work. Section 3.1 gives a general description of the experimental setup for the SNOM photocurrent measurement. The main components of the aperture-type SNOM, which provides the illumination of the solar cell sample with a nanoscale resolution, are explained in Section 3.2. Section 3.3 describes technical details for the collection and processing of the local photocurrent generated with the a-SNOM. At last, Section 3.4 depicts the principles of the finite-difference time-domain (FDTD) method, which is applied for the simulation of optical processes in the SNOM photocurrent measurements in this work. Furthermore, it provides an overview of the main configuration parameters of the home-developed FDTD simulation tool.

3.1 General setup for the SNOM photocurrent measurement

Figure 3.1 shows the principle setup deployed in this work for the SNOM photocurrent measurement with the essential components. Periodically modulated, monochromatic light is coupled into an optical fiber *via* a fiber coupler. The other end of the optical fiber, which is tapered and aluminum-coated, serves as the scanning probe. While the probe scans the sample area of interest line by line with a tip-to-sample distance of $\sim 20\,\mathrm{nm}$ by applying shear-force distance feedback regulation, the light coupled out of the small aperture at the apex of the scanning probe features the point light source and illuminates the sample surface. The locally generated photocurrent in the measured solar cell is extracted from the silver contacts on the front and the rear side. Due to the small photocurrent signal in the range of some nA, the photocurrent is enhanced firstly by a current preamplifier and subsequently by a lock-in amplifier. Together with the topography information, which is reproduced from the shear-force regulation signal, the photocurrent is converted into digital signal by an analog-to-digital converter and can be further processed by the computer.

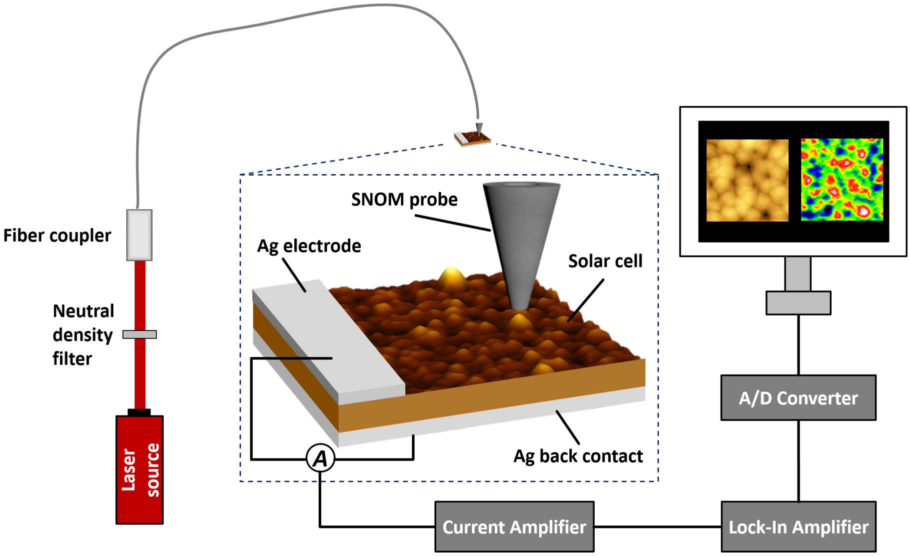

Figure 3.1: (a) Schematic diagram showing the principle setup for the measurement of the local photocurrent using an a-SNOM.

The SNOM photocurrent measurement setup is mounted on an optical table with pneumatic vibration damping legs to minimize the external mechanical vibrations, which could destroy SNOM probe during measurements. Furthermore, as shown in Fig. 3.2, the most vibration-sensitive components, such as the scanning probe, the distance control, the sample mounted on the sample holder and the various positioning systems, are set up in a vacuum chamber. More detailed descriptions of the individual components are provided in Section 3.2. Although the measurement results presented in this work are not obtained under vacuum conditions, the vacuum chamber greatly benefits the stability of the operation by providing additional protection against the mechanical vibration, blocking the air circulation and reducing the disturbing influence of the ambient light.

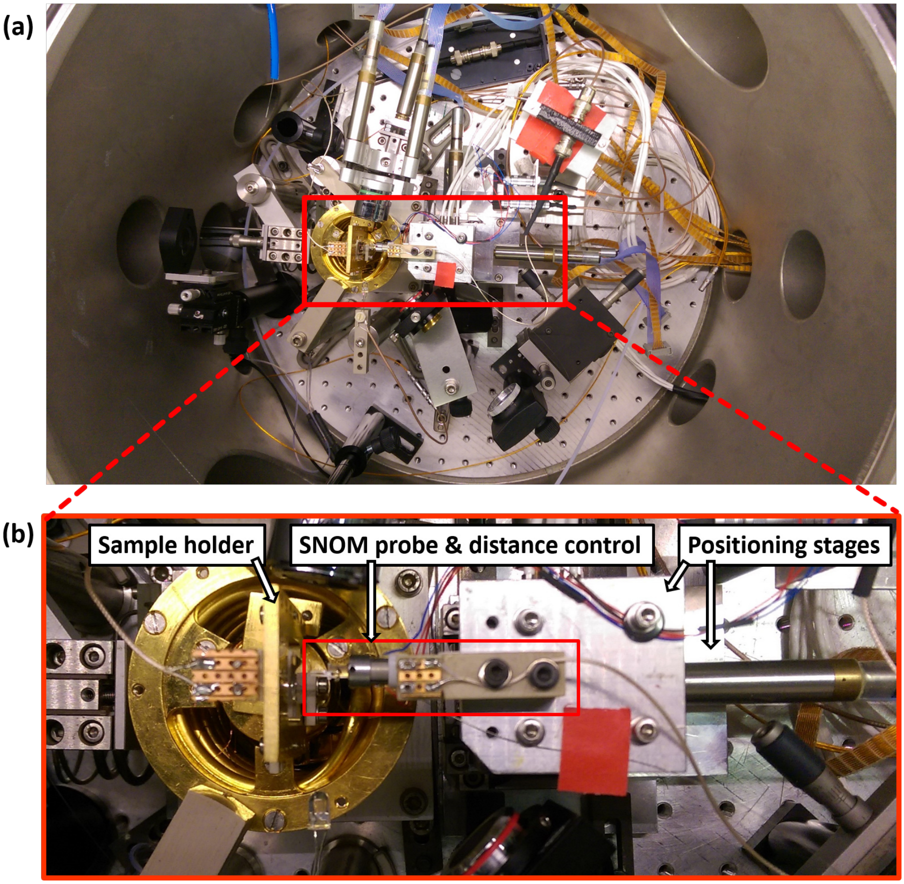

Figure 3.2: (a) Photo of the vacuum chamber which contains parts of the SNOM setup. (b) Zoom-in photo of the vibration-sensitive components in the vacuum chamber.

3.2 Main components of the a-SNOM

The core of the SNOM photocurrent measurement setup is the home-built a-SNOM, which enables the illumination with sub-100 nm optical resolution. In this section, by following the travel of light from the laser light source to the generation of charge carriers in the sampled solar cell, the main components of the a-SNOM setup are described.

Laser

In the scope of this work, five continuous-waved solid state lasers with the wavelengths 473 nm, 532 nm, 658 nm, 735 nm and 780 nm were applied as the primary light sources. The maximum laser power of the individual laser lies in the range $\sim 20-300\,\mathrm{mW}$, which partly exceed the maximum power the scanning probe is specified for ($\sim 10\,\mathrm{mW}$) [48]. Neutral density filters with different attenuation factors allow for the adjustment of the laser power to the desired value. All lasers are periodically modulated either with mechanical choppers or with electrical frequency generators, the modulation frequency also serves as an input to the lock-in amplifier (*FEMTO*), so that the resulting photocurrent signal with the corresponding frequency can be specifically enhanced.

Optical fiber and scanning probe

The laser beam is directed to a fiber coupler and couples into a single-mode optical fiber. The laser light is guided along the glass fiber toward the tip. In order to monitor potential fluctuations of the laser light power in the fiber, a silicon photodiode is installed at a certain position close to the fiber, where the glass fiber is slightly bent. This bending allows a small fraction of the laser light to be scattered out of the fiber. The scattered light is detected by the silicon photodiode and serves as a reference measurement of the light power in the glass fiber. In case of any unwanted fluctuations of laser light power in the fiber, this reference measurement allows for a correction of the photocurrent signal.

The other end of the glass fiber is processed and constitutes the near-field scanning probe. The probe processing mainly involves two treatments. The first step is the tapering of the glass fiber end to form a tip with sub-100 nm diameter. Mainly two methods are commercially applied for the reproducible fabrication of large amount of such tips: the fiber pulling [99, 100] and the fiber etching [101, 102]. While the etched fibers generally exhibit larger cone angles (up to 41°) [103], hence provide considerably higher optical throughput [104], the cone angles of the pulled probes typically do not exceed 20° [103, 105], therefore enable a good access to textured topography with its small lateral dimensions [106]. Additional treatment with Focused Ion Beam (FIB) milling facilitates an apex diameter down to 20 nm [106], however, due to the large expense of time and effort needed for the FIB milling, it is not suitable for the commercial, large-scale fabrication of fiber probes. Subsequent to the tapering, the fiber tip is coated with a metal film to form an aperture at the apex and confine the optical field to approximately the size of the aperture in the vicinity of the apex. Therefore, the diameter of the probe aperture roughly determines the optical resolution of the scanning probe of an a-SNOM in the optical near-field.

In general, there are two basic modes when operating an a-SNOM: the illumination mode and the collection mode [107, 108]. In illumination mode, the light is coupled into the glass fiber and then couples out of the aperture of the scanning probe to irradiate the sample surface in the near-field during the scanning process. In collection mode, the sample is irradiated with a light source from the far-field or near-field [109, 110], while the scanning probe collects the optical information from the sample in the near-field. In this work, the a-SNOM is only applied in the illumination mode, as it mainly functions as a point light source for the generation of the local photocurrent.

The SNOM probe applied in this work is commercially available (optical fiber with pulled, aluminum-coated scanning probe) and acquired from *Lovalite*. The typical aperture diameter lies in the range $50 - 80\,\mathrm{nm}$ [111–113].

Shear-force distance regulation

As previously introduced in Chapter 2, the subwavelength optical resolution can only be achieved if the distance between the probe aperture and the sample surface is kept at a fraction of the wavelength [114, 115]. The fact that the a-SNOM is often applied on samples with surface structures [35, 111, 116–118] requires a probe-to-sample distance regulation mechanism, which is sensitive to the variation of the relative probe-to-sample distance and fast in the response to the distance variation.

The most commonly exploited mechanism for the distance control while operating a SNOM is the shear-force mechanism [119–123].

Figure 3.3 shows components which are essential for the shear-force distance control. Before the scanning probe can be installed in the SNOM for measurements, some preparation steps have to be performed. A commercially available quartz tuning fork, whose functionality is tested in advance (especially with regard to the resonance curve), is glued on a specially designed glass holder. Subsequently, the scanning probe is attached on the quartz tuning fork by adhesive bonding. For more detailed descriptions of the probe preparation steps refer to [48].

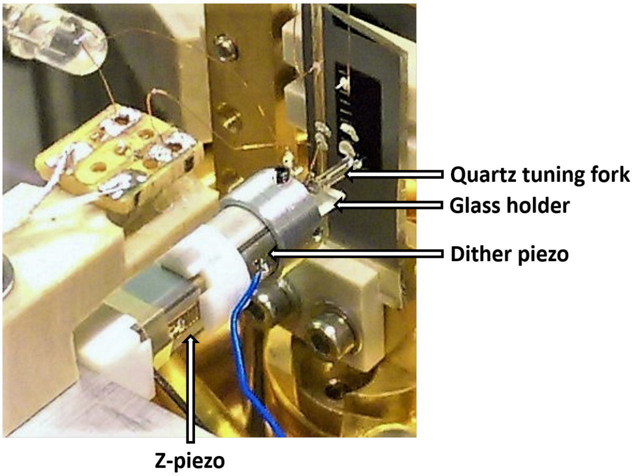

Figure 3.3: Essential components for the shear-force distance control.

Upon installation in the SNOM, the glass holder mechanically attaches to a dither piezo, which excites a lateral oscillation with a certain resonance frequency and oscillation amplitude. This lateral oscillation is transferred to the quartz tuning fork or the scanning probe *via* the glass holder. The oscillation amplitude, which usually accounts for a few nm [63, 124, 125], is detected and serves as an input of a Proportional-Integral-Derivative (PID) controller operating at a given set point.

After the approach to the sample surface, the shear-force between the scanning probe and the sample surface causes a distortion of the resonance frequency and the oscillation amplitude. The PID controller detects this distortion and reacts according to the set point with a distance adjustment of the scanning probe by applying a voltage at a z-piezo. The applied voltage is proportional to the distance regulation and therefore, can be used to reproduce the topography. During the scanning process, the probe-to-sample distance typically accounts for $\sim 20\,\mathrm{nm}$ [120, 121, 126].

The whole shear-force regulation system, consisting of the scanning probe glued on the quartz tuning fork, the dither piezo, as well as the z-piezo, is bonded to an aluminum plate (visible in Fig. 3.2). The aluminum plate is again mounted on positioning systems, which navigate the scanning probe throughout the measurements.

Positioning systems

Two different kinds of positioning stages are deployed in the SNOM setup to meet different precision requirements during the operation. For the coarse positioning of the scanning probe in all three spatial dimensions, motorized positioning stages are used (visible in Fig. 3.2, the lower one of the two positioning stages). The motorized stage has an operation range of several cm in all three directions, it is mainly used to navigate the scanning probe across a large area of the sample surface to search for the desired measurement field. For the fine positioning of the scanning probe, a multi-axis, piezo-based nanopositioning system, the so-called NanoCube (P-611.3S) from *Physik Instrumente* (PI) is applied (Fig. 3.2, below the aluminum plate). The NanoCube has a travel range of $100\,\mu\mathrm{m} \times 100\,\mu\mathrm{m} \times 100\,\mu\mathrm{m}$ and a spatial resolution of $1\,\mathrm{nm}$, which provide sufficient safety and accuracy for the coarse approach of the scanning probe to the sample surface, before the z-piezo drives the probe into the range where the shear-force becomes effective. Last but no least, the NanoCube performs the scanning of the sample surface during measurements. The standard scan area accounts for $10\,\mu\mathrm{m} \times 10\,\mu\mathrm{m}$ in this thesis, which takes roughly two hours.

3.3 Extraction and processing of the photocurrent signal

During the course of this thesis, the existing a-SNOM has been modified and extended for the local photocurrent measurement of a solar cell by utilizing the scanning probe as point illumination source. This section introduces the components of the setup, which enable the measurement and the collection of the local photocurrent signal.

The solar cell to be measured is mounted on a sample holder, which is specially designed for variable sample sizes and flexible positioning of the sample. Figure 3.4 shows the sample holder with a test sample on it. The grid of screw holes on the main body allows for the versatile positioning of the sample. With the help of clamping elements of different shapes and sizes, which are made of polyether ether ketone (PEEK) and non-conductive, the sample can be fixed to the desired position on the main body. The sample holder is installed in the SNOM photocurrent measurement setup *via* a mounting socket.

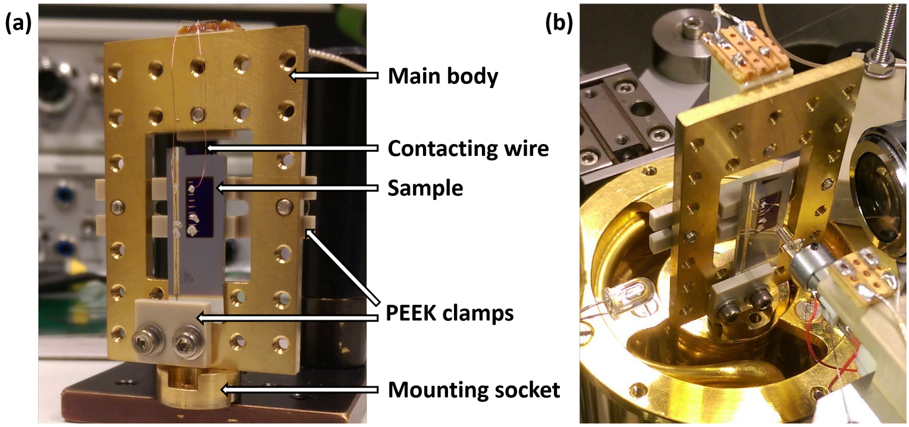

Figure 3.4: (a) Front view of the home-designed sample holder. (b) Top view of the sample holder installed in the SNOM photocurrent measurement setup.

Charge carriers are locally generated in the solar cell absorber upon illumination by the scanning probe. Subsequently, the electrons and holes drift to the corresponding contacts with reversed polarities and are extracted there. Two thin copper wires are attached to the contacts *via* conductive silver lacquer to collect the photocurrent. Due to the strongly reduced light power at the scanning-probe aperture, the local photocurrent signal usually lies in the range of some nA. For this reason, the photocurrent signal is firstly enhanced by a current amplifier (*DL INSTRUMENTS*, Model 1211), then collected by a lock-in amplifier (*Stanford Research Systems*, SR830). The lock-in amplifier receives the modulation frequency of the lasers as input and provides background suppression and noise reduction. Subsequently, an AD converter converts the photocurrent signal into digital signal and guides it to the computer. The measurement program, which is home-developed by Stephan Lehnen, records and processes photocurrent signal. Many measurement operations, including the approach of the scanning probe to the sample surface, the scanning process *etc.*, are also controlled using this program.

3.4 FDTD simulation

This section outlines the basic principles of the finite-difference time-domain (FDTD) method, which was applied for the optical simulations performed in the scope of this work. The detailed descriptions of the specific domain configurations used in the FDTD simulations are given in the respective result chapters.

The FDTD method solves Maxwell's equations rigorously and calculates the electromagnetic field at any given point in space and time for a pre-defined geometry. The application of finite differences to the solution of Maxwell's equations was first presented by Kane S. Yee in his work in 1966 [127]. In his paper from 1980, Professor Allen Taflove has coined the term finite-difference time-domain for the method developed by Yee [128]. Ever since, with the continuous development in both the algorithm and the computing power, the FDTD method has experienced a steady rise in popularity. Today, the FDTD method is one of the most widely used simulation tools in the computational electromagnetics. It constitutes an essential tool for problems such as the propagation, the scattering, *etc.*, of the electromagnetic waves. Numerous books have been published on it [129–131].

Basics principles

As the name FDTD indicates, the method replaces the temporal and spatial derivatives in Maxwell's equations in 2.1 with finite differences using second order central-difference approximation. For this purpose, both space and time are discretized, which results in an orthogonal cubic spatial grid. In addition, the electric fields and the magnetic fields are staggered in both space and time. In order to obtain the electric field at a desired point of space and time, one needs to solve the finite difference equations from the known neighboring magnetic fields and the known electric field at this spatial point one time step back in the past. Similarly, in order to obtain the magnetic field at a desired point of space and time, one needs to solve the finite difference equations from the known neighboring electric fields and the known magnetic field at this spatial point one time step back in the past. These steps are repeated until the desired fields are attained.

For the FDTD simulation of domains other than free space, i.e. domains consisting of different materials, specific permittivity and permeability values are assigned to every point of the spatial grid.

Perfectly matched layer

Aside from some special configurations of the simulated structures, such as a resonator, very often the problems investigated with FDTD simulations require open boundary conditions, i.e. infinite space. Clearly, it is not feasible to really simulate an infinite domain, nor it is necessary. The key lies in the reflection-free termination of the FDTD grids. If the electromagnetic waves reaching the boundaries are not reflected, they cannot interact with, hence have no influence on the interior of the domain. This configuration allows the finite simulation domain to behave equivalently to infinite space.

There are mainly two possible approaches to construct such an open boundary condition. One of them is the application of periodic boundary conditions [132,133], which however requires that both the simulated structures and the electromagnetic fields are periodic. The other approach is the application of absorbing boundary conditions [134,135], where the open boundary condition is realized by implementing non-reflective, absorbing layers at the boundaries. Among the absorbing boundary conditions, one of the most prominent, state-of-the-art approach is the perfectly matched layers (PML), which is also applied in all FDTD simulations presented in this work.

The PML-concept was firstly described by Bérenger in 1994 [136]. By introducing a perfectly absorbing layer consisting of specially designed (non-physical) anisotropic medium, the electromagnetic waves reaching the boundary are transmitted into the PML's without reflection and subsequently absorbed within a few cells. Furthermore, this perfectly absorbing behavior is realized independent of wavelength, polarization and incidence angle of the electromagnetic waves. More theoretical details and technical implementation for the FDTD simulation can be found in [136]. Aside from the technique introduced by Bérenger, further approaches were developed to obtain perfectly absorbing boundaries, such as complex coordinates stretching [137, 138], uniaxial PML [139], *etc.*, which are commonly summarized as PML techniques as well, although they do not necessarily base on Bérenger's equations.

In the FDTD simulations presented in this work, the thickness of the PML layers accounts for a few ten-fold of the resolution, which is sufficiently large for the transmitted electromagnetic waves to be completely absorbed.

3.4.1 FDTD simulation tool

In this work, FDTD simulations are performed to support the understanding and interpretation of the experimental results from the SNOM photocurrent measurements. Therefore, a good agreement between the simulated system and the measurement system needs to be ensured. The FDTD simulation tool used in this work is a custom-built software based on the MEEP FDTD solver [140]. An interface based on a text file is used for the input of configuration parameters, which define the simulation domains. These configuration parameters include

- the corresponding topography files for the individual layers of the simulated structures.

- the physical dimension of the respective layers: lateral sizes, thicknesses, *etc.*
- the optical data of the layer materials: mainly the real and the imaginary part of the permittivity.
- the properties of the scanning probe: the geometry of the probe, the probe position, *etc.*
- the properties of the illuminating light: the wavelength, the polarization direction.

In this work, both idealized topography (Chapter 4) and real topography recorded by atomic force microscope (Chapter 6) are used. The thicknesses of the layers are chosen such that they match those of the measured sample. The wavelength-dependent permittivity values are obtained from spectroscopic ellipsometry measurements of the samples. Aside from the proper representation of the sample structure, the incorporation of a SNOM scanning probe is indispensable. The simulation of the scanning probe bases on the same principle presented by M. Ermes in [113, 141]. The scanning probe has the idealized geometry of a truncated cone and is mainly characterized by the following parameters: the sidewall angle of the cone, the thickness of the metal coating and the aperture radius. For illustration purpose, Fig. 3.5 shows the image of an exemplary SNOM probe with a cone angle of 15°, coating thickness of 60 nm and an aperture radius of 200 nm.

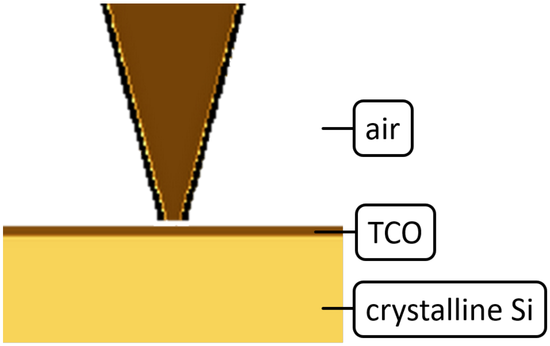

Figure 3.5: Exemplary image of a SNOM probe in the FDTD simulation. The probe has a cone angle of 15°, coating thickness of 60 nm and an aperture radius of 200 nm.

The image of the scanning probe is directly extracted from the FDTD simulation domain and shows only an area of 3 µm × 3 µm with a resolution of 20 nm, therefore revealing visible pixels. The illumination is realized by implementing a point light source inside the scanning probe. Depending on the required configuration, a specific position and height can be assigned to the scanning probe.

4 Investigation of the flat μc-Si:H and the a-Si:H thin-film solar cells

This chapter focuses on the investigation of optical processes in the generation of local photocurrent in a solar cell. The first section provides a short description of the investigated flat μc-Si:H thin-film solar cell and subsequently presents SNOM local photocurrent measurement results with five different wavelengths ranging from 473 nm to 780 nm. In Section 4.2 and Section 4.3, FDTD simulation results with an idealized topography are presented and compared to the experimental measurement results of a periodically textured a-Si:H thin-film solar cell. Section 4.4 provides an extensive discussion of the effect of the light polarization on the local light coupling through an a-SNOM aperture. In Section 4.5, a discussion regarding the correlation between the local photocurrent response and the topographic structure is given. Parts of the results in this chapter were published in [142] and [143].

4.1 SNOM photocurrent measurement results

As already mentioned, the specimen chosen for the local photocurrent measurement with the SNOM is a flat μc-Si:H thin-film solar cell fabricated in substrate configuration. Figure 4.1 illustrates the layer structure of the sample. Firstly, a 250 nm thick Ag layer and a 80 nm thick aluminum-doped zinc oxide (ZnO:Al) layer are sputtered on a flat substrate (usually glass substrate with a ZnO:Al film deposited on it *via* radio frequency magnetron sputtering), which serve as the reflector and the rear contact of the solar cell. Subsequently, a 20 nm thick n-doped μc-SiO$_x$:H layer, a 1.3 µm thick intrinsic μc-Si:H layer and a 18 nm thick p-doped

μc-SiO$_x$:H layer are deposited sequentially by plasma enhanced chemical vapor deposition (PECVD) [144]. Afterward, a ZnO:Al layer of 80 nm thickness is sputtered on top of that as the transparent front contact layer. At last, Ag finger electrodes with a thickness of 1 µm are deposited *via* thermal evaporation.

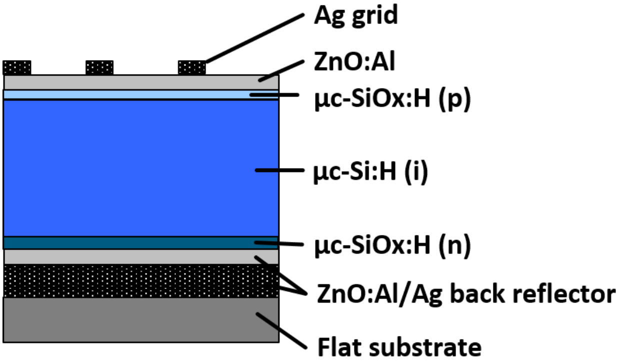

Figure 4.1: Schematic showing the layer structure of the measured hydrogenated microcrystalline silicon (μc-Si:H) thin-film solar cell.

SNOM local photocurrent measurements were performed on a scan field of 8 µm × 8 µm with five different wavelengths: 473 nm, 532 nm, 658 nm, 735 nm and 780 nm. Figure 4.2 (a) shows the topography image of the measured area. The protrusions on the surface are the tops of the micro-crystallites, which are formed by the columnar growth of the crystallites [77]. The lateral sizes of the protrusions vary in the range from hundred to several hundred nanometers, while the heights of the protrusions lie in the range of a few ten nanometers. Figure 4.2 (b) – (f) show photocurrent images from the same area for different wavelengths. In all photocurrent images, the photocurrent signal is normalized by the corresponding average value and the images have the same relative scale. This representation allows for a better comparison of the photocurrent images recorded at different wavelengths, as the relative contrast shows how strong the local photocurrent variation is in every image. As can be seen in Fig. 4.2, this contrast is very similar for the wavelengths 473 nm, 735 nm and 780 nm, while the contrast seems to be weaker for the two wavelengths in between. This reduced contrast can be mainly ascribed to the parasitic light caused by the scattered laser light, which was stronger in case of 532 nm and 658 nm. The photocurrent image recorded at 473 nm in Fig. 4.2 (b) exhibits a rectangular area with overall higher photocurrent signal at the top. This is probably caused by the fluctuation of the laser power during the measurement, which could not be completely corrected in this case, or a slight "wear-off" of the probe tip during the scanning process, which led to a minimally wider-opened aperture.

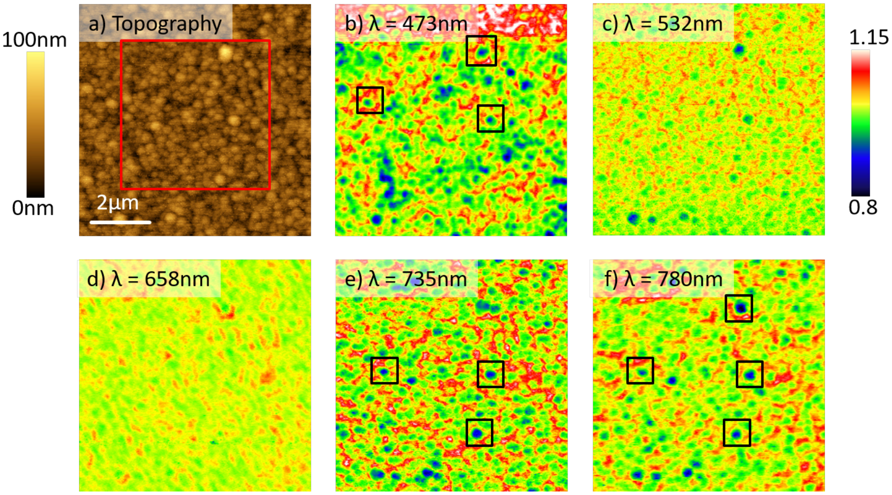

Figure 4.2: (a) SNOM topography image of the flat μc-Si:H thin-film solar cell from a scan field with size of 8 µm × 8 µm. (b)-(f) SNOM photocurrent images from the area in (a) recorded at $\lambda = 473$ nm, $\lambda = 532$ nm, $\lambda = 658$ nm, $\lambda = 735$ nm and $\lambda = 780$ nm, respectively. In all SNOM photocurrent images, the photocurrent is normalized by the average value and the images are displayed in the same relative range $(0.8 - 1.15)$. A strong correlation between the local photocurrent signal and the surface topography is clearly visible for all wavelengths, especially at the surface protrusions highlighted with black squares.

In all photocurrent images, the local photocurrent signal exhibits a strong correlation to the surface topography, which appears to be the same for all wavelengths: the local photocurrent response is lower at topographic maximums, e.g. on top of the protrusions, while the local photocurrent response is higher at topographic minimums, e.g. in the surrounding grooves between the protrusions. In Fig. 4.2, some protrusions where this correlation can be very well observed are highlighted with black squares. In order to visualize this correlation more clearly, the measurement results from an area of 5 µm × 5 µm are shown as 3D-representations in Fig. 4.3. Since the correlation between the local photocurrent signal and the surface topography is the same for all five wavelengths, only the measurement results of the shortest wavelength ($\lambda = 473\,\text{nm}$) and the longest wavelength ($\lambda = 780\,\text{nm}$) are displayed in 3D as two extreme cases.

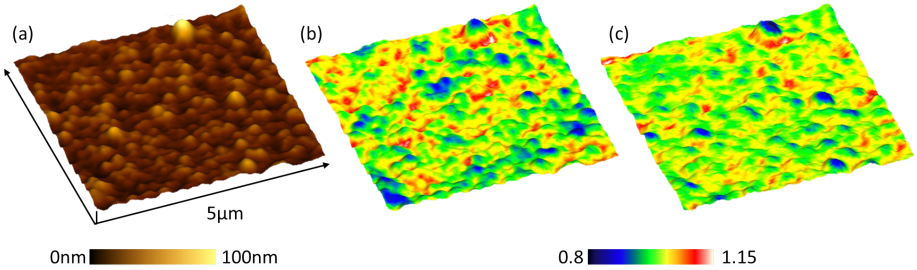

Figure 4.3: (a) 3D topography image from an area of 5 µm × 5 µm, indicated with a red square in the SNOM topography image in Figure 4.2 (a). (b)-(c) 3D SNOM topography image from (a) color-coded with the photocurrent signal at $\lambda = 473\,\text{nm}$ and $\lambda = 780\,\text{nm}$, respectively. In all 3D images, the topography is smoothed and the z-axis is scaled by a factor of 5 with reference to the x- and y-axis for better clarity. Adapted from [143] with permission from the PCCP Owner Societies.

Figure 4.3 (a) shows the 3D image of the measured topography. Due to the small heights of the surface protrusions, the z-axis is scaled by a factor of 5 with reference to the x- and y-axis to make the topographic structures better visible. Figure 4.3 (b) and (c) present the 3D-topography image from (a), which is color-coded with the photocurrent images recorded at $\lambda = 473\,\text{nm}$ and $\lambda = 780\,\text{nm}$, respectively. For both wavelengths, the global variation of the photocurrent signal accounts for $\sim \pm 20\,\%$ around the average value. On a local scale (one individual protrusion with the surrounding grooves), the min-max contrast of the photocurrent signal varies in a range of $5\,\% - 20\,\%$ on the measured field.

As described in Chapter 2, the measured local photocurrent response is determined by both optical and electrical processes. If electrical processes would be the dominate mechanism, then the local variation of the photocurrent would be mainly caused by local material inhomogeneity, which originates from the distribution of the micro-crystallites and the voids or amorphous silicon filling the space between the micro-crystallites. This interpretation might apply for the photocurrent measurement result in the case of 473 nm due to the short absorption length (~ 100 nm) of light in μc-Si:H at this wavelength. However, with increasing wavelength, the absorption length of the light in μc-Si:H increases as well. In the case of the longest wavelength 780 nm, the absorption length of light already reaches $\sim 10\,\mu$m, which is much larger than the μc-Si:H layer thickness. Therefore, for longer wavelengths, the excitation volume is likely defined by scattering and the photocurrent response at a single position would be the averaged result from a large volume containing many micro-crystallites. As a consequence, the obtained photocurrent image would appear to be much more homogeneous, as the effect of a single micro-crystallite could not be resolved. The fact that, all photocurrent images in Fig. 4.2 manifest comparably fine feature sizes of $\sim 100 - 150$ nm, where individual protrusions are clearly visible, indicates an insignificant influence of local electronic properties, hence the local photocurrent response is likely dominated by optical processes. In order to provide theoretical verification of this interpretation, optical simulations using FDTD-methods are carried out. The results are presented in the following sections.

4.2 Domain configuration and parameters for the FDTD simulations

The FDTD simulations are performed within a three-dimensional spatial domain with the size of $10\,\mu\text{m} \times 10\,\mu\text{m} \times 5\,\mu\text{m}$. In order to sufficiently resolve the SNOM probe aperture and small topographic structures, the spatial resolution is chosen to be 10 nm. Two different configurations of the layer structure are created. Figure 4.4 (a) and (b) show the cut-outs with a size of $2\,\mu\text{m} \times 2.5\,\mu\text{m}$ from the simulation-domain profiles for each configuration, respectively. In Fig. 4.4 (a), the layer structure corresponds to that of a real μc-Si:H thin-film solar cell, which was measured in the experiment. From the bottom to the top, the layer stack consists of a flat metal substrate approximated by a perfect electric conductor (PEC) layer, a TCO layer with a thickness of 80 nm, an intrinsic μc-Si:H layer with a thickness of 1.34 µm and a top TCO layer with a thickness of 80 nm. The n- and p-doped μc-SiO$_x$:H layers are omitted due to their negligible thickness (~ 20 nm) compared to that of the entire layer stack, in addition, they have similar optical properties as the intrinsic μc-Si:H layer. The space above the sample comprises of air. The SNOM probe providing local illumination has the idealized geometry of a truncated cone. The sidewall angle of the cone is 15° with respect to the surface normal. The metal coating of the probe has a thickness of 30 nm, which is approximated by a PEC layer. The probe aperture has a diameter of 80 nm. This configuration is referred to as the "*layer-stack configuration*" in the following. In the layer-stack configuration, various optical processes, such as reflection, light guidance in the layers and light coupling efficiency, are taken into consideration. However, the individual contributions of these processes can hardly be determined. In the second configuration, which is depicted in Fig. 4.4 (b), the bottom PEC layer and the bottom TCO layer are removed and replaced by μc-Si:H. This way, a μc-Si:H half space is created below the top TCO layer. In addition, the imaginary part of the permittivity of the μc-Si:H is set to zero to assume a non-absorbing material. As a consequence, light coupled into the μc-Si:H half space will be transmitted through it without being attenuated or reflected back. In this configuration, by calculating the light intensity in the μc-Si:H half space, the local light coupling efficiency can be determined. This configuration is referred to as the "*half-space configuration*" in the following. In order to realize open boundary conditions and prevent any reflection of the light at the boundaries of the 3D simulation domains, all sides of the simulation domains are covered with perfectly matched layers (PML), which have a thickness of 0.5 µm.

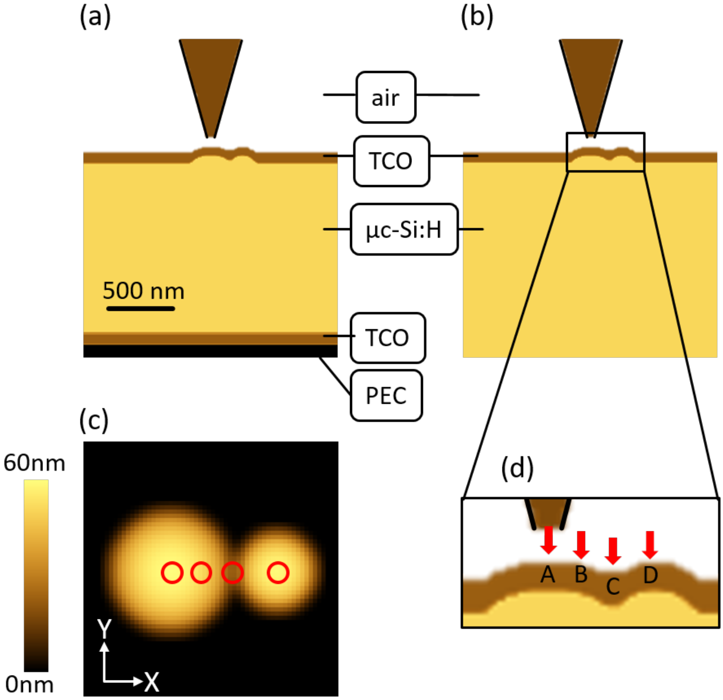

Figure 4.4: Cut-outs from the profiles of the simulation domains created with (a) layer-stack configuration and (b) half-space configuration. Both cut-outs have a size of 2 µm × 2.5 µm. PEC stands for perfect electric conductor. (c) Top-view 2D image of the idealized topographic features for the simulation. For better visualization, only an area of 0.6 µm × 0.6 µm from the total area of 10 µm × 10 µm is shown. The topographic features are formed by two partly overlapping partial spheres with radii of 150 nm and 100 nm, respectively. Both partial spheres are 60 nm high. The four SNOM probe positions selected for the simulations are indicated with red circles in (c) and with red arrows in the profile zoom-in image in (d).

Figure 4.4 (c) shows the top-view of the artificially generated, idealized topographic structures. The topography consists of two partial spheres, which are smoothed at their boundaries and slightly overlap with each other. The choice of the partial sphere bases on the fact that it is a simple geometric structure, which resembles the shape of the surface protrusions in topography image from the measurements the most. The larger partial sphere has a radius of 150 nm, while the smaller partial sphere has a radius of 100 nm. The height of both partial spheres accounts for 60 nm. The chosen geometry represents the most prevalent protrusion sizes in the measurements.

The FDTD simulation demands a large amount of computation time and memory. Furthermore, for every single location of the probe, every wavelength and each layer-structure configuration, an own FDTD simulation is required. Therefore, four probe positions are selected, where the most characteristic topographic features are identified. These four characteristic positions are indicated with red circles in Fig. 4.4 (c) and with red arrows in Fig. 4.4 (d), respectively. Figure 4.4 shows the zoom-in image of the probe aperture and topographic structures. From the left to the right, the probe positions include:

- A and D: above the tops of the two partial spheres mimicking local topographic maximums with different curvatures.
- B: above a flank of the larger partial sphere.
- C: between the partial spheres mimicking a local topographic minimum.

In real measurements, the probe-sample distance might vary during the scanning process and lead to artifacts [145]. In order to exclude the possibility that the correlation observed in the measurements could originate from such artifacts, it is essential to keep the probe-sample distance constant for all probe positions in the FDTD simulations. This distance is defined as the distance between the topography surface and the aperture center and is set to 70 nm in the simulations, which is the lower limit for the existing geometry. This way, the difference between the simulation results of individual probe positions only originate from the local topography, and is not affected by the probe-sample distance variations. Furthermore, similar to the experiments, the optical simulations are performed with both wavelengths 473 nm and 780 nm.

One of the simulation parameter is the light polarization. In our FDTD simulations, there are two fundamental polarization directions, which are indicated in Fig. 4.4 (c) with the white arrows. For simplicity, in the following the two polarization directions are referred to as the "*x-polarization*" and "*y-polarization*", respectively.

If the topographic structure exhibits a preferential orientation in one of the polarization directions, the light polarization could have a significant impact on the resulting intensities. As can be seen in Fig. 4.4 (c), the generated topographic structure shows a preferential orientation in the x-axis. In order to investigate the effect of the light polarization, FDTD simulations with both x-polarization and y-polarization have been performed. A detailed discussion of the effect of the light polarization is given in Section 4.4.

However, due to the random distribution of the surface protrusions as seen in the topography image in Fig. 4.2 (a), there is no preferential orientation of the topography. Therefore, the light polarization will less likely have an effect on the resulting photocurrent in the measurements. To take this into account, in the following section the averaged value of the simulation results from both polarization directions is used to assume the unpolarized case.

4.3 FDTD simulation results and comparison with the measurements

In order to make the simulation results comparable within the individual configuration, firstly a measure has to be defined, which relates to the measured quantity in the experiments. For the layer-stack configuration, this measure is defined as the integrated light intensity I_A over the complete μc-Si:H layer. I_A is proportional to the absorbed light intensity in the μc-Si:H layer, which corresponds to the photocurrent of the solar cell. For the half-space configuration, this measure is defined as the integrated light intensity I_T over an arbitrary horizontal plane in the μc-Si:H half space. Due to the non-absorbing character of the μc-Si:H half space, I_T is identical for every horizontal plane and corresponds to the totally transmitted light intensity into the μc-Si:H half space. Consequently, I_T can be considered as a measure for the light coupling efficiency. Furthermore, for a better comparability between the simulation results from different wavelengths, FDTD simulations have been performed for a flat topography for each combination of the wavelengths and the simulation-domain configurations. The corresponding calculated absorbed intensities I_A and the calculated transmitted intensities I_T serve as the normalization factor in all diagram plots of the simulation results in this chapter.

Figure 4.5 (a) shows the normalized absorbed intensities I_A as a function of the four probe positions in the layer-stack configuration for both wavelengths $\lambda = 473\,\mathrm{nm}$ (blue circles) and $\lambda = 780\,\mathrm{nm}$ (red squares). For a better attribution of the absorbed intensities to the probe positions, i.e. topographic features, a horizontal line scan through the center of the generated topographic structure is depicted in the diagram by a black dashed line. For both wavelengths, the maximum I_A is obtained when the probe is placed between the two partial spheres, i.e. on a topographic minimum, while weaker I_A is obtained when the probe is placed on the tops of the partial spheres or on the flank. This correlation corresponds very well to that observed in the SNOM photocurrent measurements shown in Fig. 4.3 (b) and (c). It should be emphasized that, despite the form and size variation of the numerous surface protrusions, the theoretically calculated correlation applies to every single protrusion in the measurements. In addition, as highlighted with black squares in Fig. 4.2 (b), (e) and (f), surface protrusions with local min-max contrasts similar to those observed in Fig. 4.5 ($\sim 20\% - 30\%$) are found in the scan field of $8\,\mu\mathrm{m} \times 8\,\mu\mathrm{m}$. Accordingly, the results from the optical simulations do not only reproduce the experiments qualitatively, but also deliver a reasonable quantitative description of the experimental results. Therefore, the correlation between the local photocurrent response and the local topographic features observed in the measurements mainly originates from optical processes.

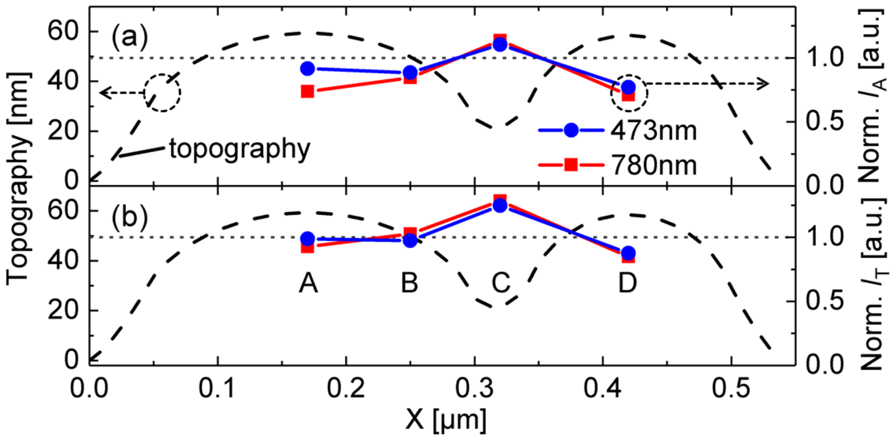

Figure 4.5: (a) Absorbed intensity I_A in the layer-stack configuration and (b) transmitted intensity I_T in the half-space configuration plotted as a function of the SNOM probe position for both wavelengths $\lambda = 473\,\mathrm{nm}$ (blue circles) and $\lambda = 780\,\mathrm{nm}$ (red squares), respectively. The corresponding simulation domains are depicted in Fig. 4.4. In both configurations and for both wavelengths, the results of different probe positions are normalized by the I_A and I_T calculated for a flat topography. The maximum of the respective graph is always found at the topographic minimum between the partial spheres. The black dashed lines in both diagrams represent the line scan through the center of the idealized topographic structure.

In order to further specify the dominating optical mechanism, FDTD simulations were carried out for the half-space configuration. Also here, the subsequently calculated transmitted intensities I_T are normalized by the results from the flat-topography case. Figure 4.5 (b) shows the transmitted intensities I_T as a function of the four probe positions for both wavelengths. Both graphs exhibit a similar general trend as observed in the layer-stack configuration, namely, maximum I_T is obtained when the probe is positioned on the topographic minimum, while lower I_T is obtained when the probe is placed on topographic maximums or on the flank. In the half-space configuration, the only relevant optical mechanism is how efficiently the light is coupled into the μc-Si:H half space. The fact that the graphs of both short and long wavelengths become very close regarding both, the general trend and the overall contrast, indicates that, if the light coupling is the dominating mechanism, similar coupling efficiency is expected for the same topographic features irrespective of the wavelength (at least in the range 473 nm − 780 nm).

It is noted that for both wavelengths, an offset between the graphs from different configurations is observable. This could be attributed to the variation of the permittivity in both configurations. As described in Section 4.2, while in layer-stack configuration the μc-Si:H absorber has a complex permittivity, it has a real permittivity in half-space configuration to simulate the non-absorbing condition. While this difference does not have an influence on the trend or the overall relative contrast of the graph, it could lead to different reflection coefficients in the two simulation-domain configurations, hence to the offset between the graphs.

Finally, the simulation results of both configurations are compared for each wavelength, respectively. In case of $\lambda = 473\,\mathrm{nm}$, the graphs of both configurations are very similar in both the general trend and the overall contrast. This can be explained by the very short absorption length ($\sim 100\,\mathrm{nm}$) compared to the layer thickness ($1.34\,\mu\mathrm{m}$) in the layer-stack configuration. Figure 4.6 (a) shows the intensity profile of the xz-plane centrally crossing the topographic structure for $\lambda = 473\,\mathrm{nm}$ in the layer-stack configuration. For clarity, only the intensity distribution in the μc-Si:H layer is displayed. The intensity is normalized by the maximum value. The red dotted lines indicate the shape and the position of the probe, as well as the interfaces of the μc-Si:H layer. Due to the short absorption length, the light is absorbed within a few hundred nanometers. Therefore, it cannot reach the bottom PEC layer and cannot be reflected or guided. As a consequence, the absorbed intensity I_T mainly depends on how efficiently light is locally coupled to the μc-Si:H layer, which corresponds to the half-space case, hence yielding similar results for both configurations.

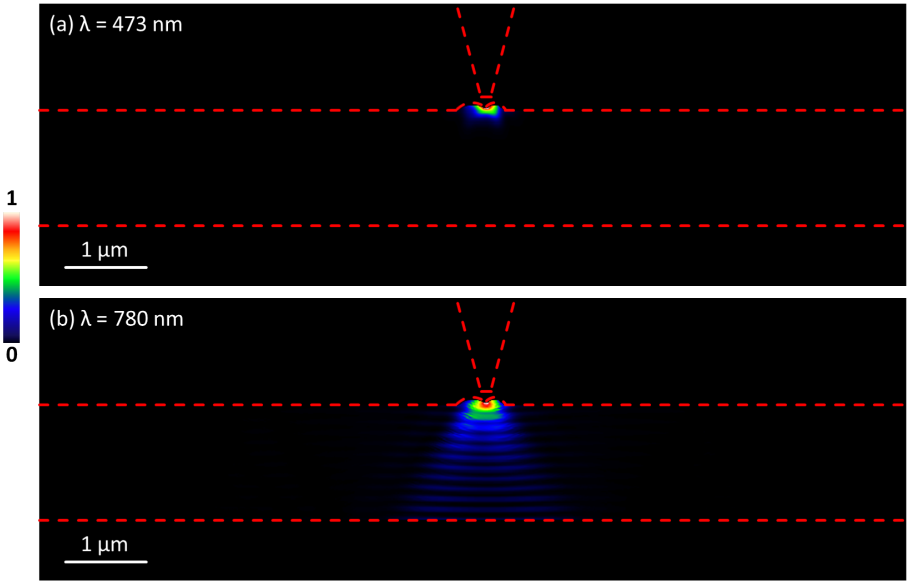

Figure 4.6: (a) Intensity profile of the central xz-plane crossing the idealized topographic structure for $\lambda = 473\,\mathrm{nm}$ in the layer-stack configuration. For clarity, only the intensity distribution in the μc-Si:H layer is displayed. Due to the short absorption length of $\sim 100\,\mathrm{nm}$, the light only propagates for a few hundred nanometers in the μc-Si:H layer before it is fully absorbed. (b) Intensity profile of the central xz-plane for $\lambda = 780\,\mathrm{nm}$. Due to the long absorption length of $\sim 10\,\mathrm{\mu m}$, the light can reach the bottom of the μc-Si:H layer where it is reflected and propagates further throughout the layer. In both intensity profiles, the intensity is normalized by the individual maximum value for each wavelength. The red dotted lines outline the contours of the probe and the μc-Si:H layer.

In case of $\lambda = 780\,\mathrm{nm}$, compared to the layer-stack configuration, the graph of the half-space configuration in Fig. 4.5 (b) has preserved the general trend but lost the overall contrast. For example at $x \approx 0.17\,\mathrm{\mu m}$, the relative contrast to the maximum has decreased from $\sim 35\%$ in the layer-stack configuration to $\sim 28\%$ in the half-space configuration. Figure 4.6 (b) shows the intensity profile of the central xz-plane for $\lambda = 780\,\mathrm{nm}$. Due to the longer absorption length of $\sim 10\,\mathrm{\mu m}$, the light can propagate a large distance in all directions in the layer-stack configuration. Consequently, it can reach the bottom PEC layer and will be reflected and guided through the μc-Si:H layer. All these factors will have an impact on the overall contrast and can lead to deviations of the graphs between the layer-stack configuration and the half-space configuration, where only the local light coupling determines the resulting intensities. Nevertheless, as can be seen in Fig. 4.5, this deviation is only minimal and does not change the overall trend. Hence, also in the case of long wavelength, i.e. long absorption length, the local light coupling remains the dominating optical mechanism. As a conclusion, the results of the FDTD simulations confirm the interpretations in Section 4.1 that in the presented SNOM photocurrent measurements, the local light coupling efficiency has the dominating influence on the local photocurrent response for all applied wavelengths, which is determined by the local surface topography of the sample.

4.4 Effect of the light polarization on the local light coupling

In the previous sections, local light coupling through topographic structures has been identified as the main factor determining the local photocurrent signal in the presented measurements of a flat μc-Si:H thin-film solar cell. Due to the lack of a preferential orientation of the surface protrusions, no effect of the light polarization is observed in the measurements. This section focuses on the effect of the light polarization on the local light coupling through a topographic structure with a preferential orientation. This effect is firstly analyzed with the FDTD simulation results of the half-space configuration, then demonstrated in the SNOM local photocurrent measurements of a periodically textured a-Si:H thin-film solar cell. The comparison between the simulation results of the flat μc-Si:H thin-film solar cell and the measurement results of the a-Si:H thin-film solar cell is justified, as the local light coupling is shown to be determined by the local surface topography in homogeneous material and the amorphous silicon features even higher material homogeneity than the microcrystalline silicon. Detailed descriptions of the periodically textured a-Si:H thin-film solar cell regarding both the fabrication process and the sample structure are provided in [146] and [147].

As mentioned in Section 4.2, in our custom-developed FDTD simulation tool, two light polarization directions are available: the x-polarization and the y-polarization. Furthermore, the idealized topographic structure for the simulation has a preferential direction in the x-axis. Figure 4.7 shows the normalized transmitted intensity I_{T} as a function of the four probe positions in the half-space configuration for both wavelengths (a) $\lambda = 473\,\mathrm{nm}$ (blue circles) and (b) $\lambda = 780\,\mathrm{nm}$ (red circles). In each diagram, the results for the x-polarization are depicted by empty circles containing a horizontal line and the results for the y-polarization are depicted by empty circles containing a vertical line, respectively. For a better attribution of I_{T} to the probe positions, i.e. topographic features, a horizontal line scan through the center of the idealized topographic structure is depicted in the diagrams by a black dashed line.

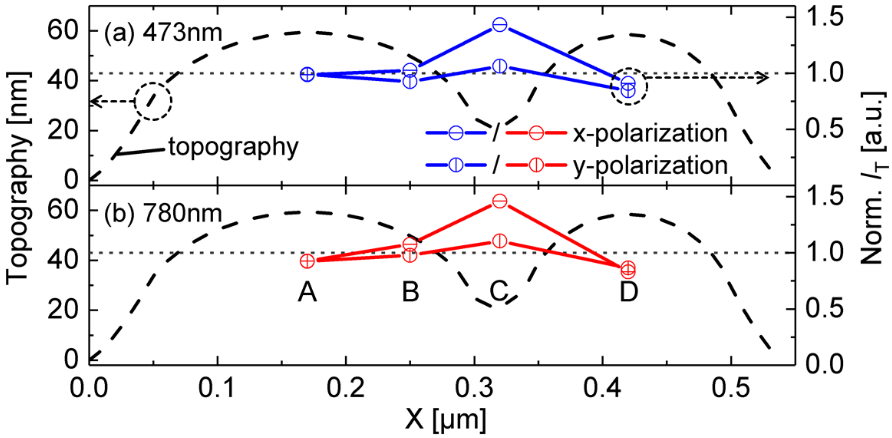

Figure 4.7: Normalized transmitted intensity I_{T} in case of x-polarization (empty circle with horizontal line) and in case of y-polarization (empty circle with vertical line) in the half-space configuration for (a) $\lambda = 473\,\mathrm{nm}$ and (b) $\lambda = 780\,\mathrm{nm}$. The black dashed lines in both diagrams represent the line scan through the center of the idealized topographic structure. The behavior of the graphs in (a) are very similar to that in (b) despite the different wavelengths. I_{T} exhibits the strongest polarization dependency at the topographic minimum (position C), which accounts for $\sim 36\%$.

As can be seen in Figure 4.7 (a) for $\lambda = 473\,\mathrm{nm}$, the transmitted intensity

I_{T} shows no significant difference between the x-polarization and the y-polarization at positions A, B and D, while at position C the contrast amounts for $\sim 36\%$. At position A and D, i.e. on tops of the partial spheres, the I_{T} values of different polarizations almost coincide with each other. Due to the rotational symmetry of the partial spheres around the z-axis, the light-polarization direction does not influence the coupling efficiency [148]. With the increase in the asymmetry of the topography shape, the deviation between the I_{T} values for different polarizations also begins to increase. At position B, i.e. on the flank of the larger partial sphere, the contrast reaches $\sim 10\%$. At position C, i.e. at the topographic minimum between the partial spheres, the asymmetry of the topograhic structure with regard to the x-axis and the y-axis becomes the strongest. Accordingly, the deviation between the I_{T} values of different light polarizations also reaches the maximum with a contrast of $\sim 36\%$, with the transmitted intensity I_{T} for the x-polarization being the larger one. As a conclusion, for the presented idealized structures, if the probe is placed above the position where the topographic structure has the strongest rotational asymmetry, the local light coupling efficiency is enhanced for that light-polarization direction which accords with the preferential direction of topographic structure. The same behavior is observed for the graphs in Fig. 4.7 (b) for $\lambda = 780\,\mathrm{nm}$, indicating that the investigated effect of the light polarization on the local light coupling efficiency applies at least to all wavelengths in this thesis ($473\,\mathrm{nm} - 780\,\mathrm{nm}$).

As a visual demonstration of the simulation results, Fig. 4.8 shows the intensity profiles of the xz-plane centrally crossing the topographic structure in half-space configuration for different wavelengths and light polarizations. The intensity profiles all have a size of $10\,\mu\mathrm{m} \times 3.25\,\mu\mathrm{m}$. For clarity, only the intensity distribution in the μc-Si:H half space is displayed. The probe position and the μc-Si:H/TCO-interface are outlined with red dotted lines. For better comparison, the intensity profiles of the same wavelength, but different polarizations are displayed with the same scale. For both wavelengths, the intensity profile exhibits a broader distribution in the polarization direction - in this case the x-direction. Similarly, the intensity profiles in the yz-plane exhibit broader distribution in the y-direction for y-polarized light, which are not shown here. Moreover, in accordance with the results shown in Fig. 4.7, the transmitted intensity is significantly higher for x-polarization.

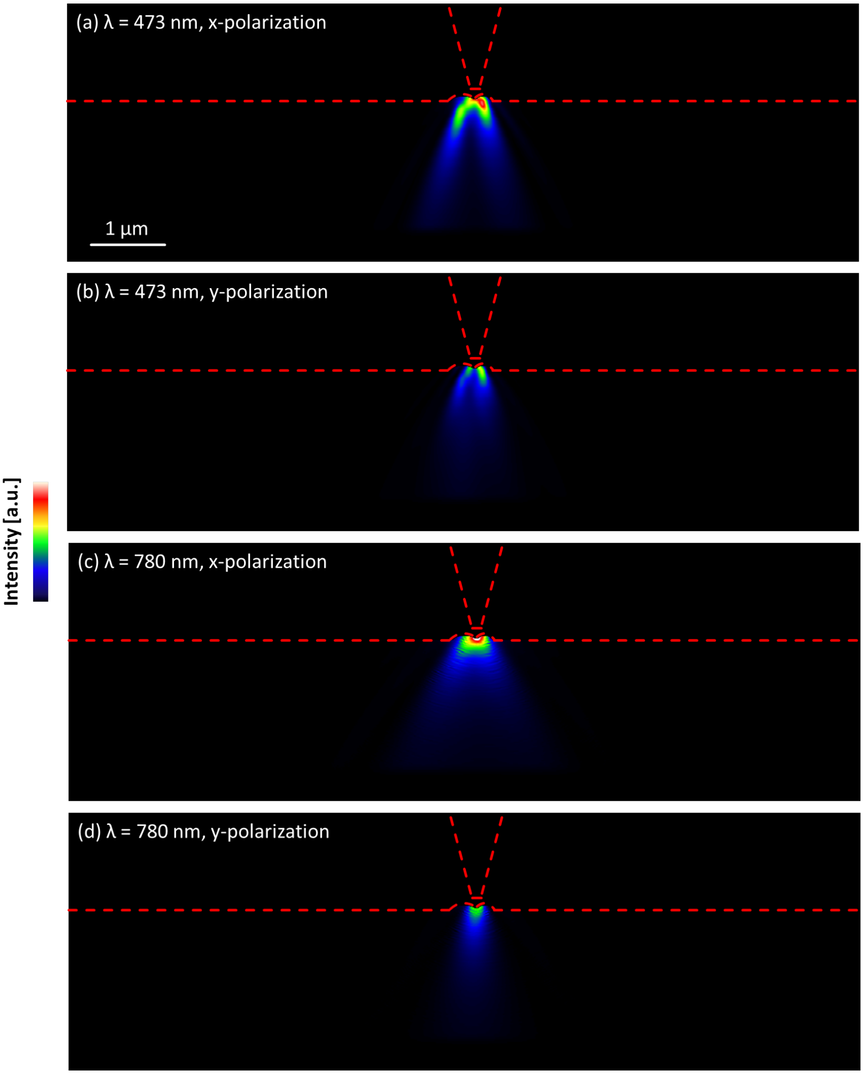

Figure 4.8: Intensity profiles of the central xz-plane crossing the idealized topographic structure in the half-space configuration. All profiles have a size of $10\,\mu\text{m} \times 3.25\,\mu\text{m}$. For clarity, only the intensity distribution in the μc-Si:H layer is displayed. (a) Intensity profile for x-polarized light at $\lambda = 473\,\text{nm}$. (b) Intensity profile for y-polarized light at $\lambda = 473\,\text{nm}$. (c) Intensity profile for x-polarized light at $\lambda = 780\,\text{nm}$. (d) Intensity profile for y-polarized light at $\lambda = 780\,\text{nm}$. The same scale is applied for each wavelength. For both wavelengths, the transmitted intensity is notably higher in the case of x-polarization.

Due to the random distribution of the surface protrusions, the flat μc-Si:H thin-film solar cell is not very suitable for the experimental investigation of the light polarization effect, whereas an a-Si:H thin-film solar cell with periodic structures provides to be a much better candidate. Owing to the ordered arrangement of the surface structures, a periodically textured a-Si:H thin-film solar cell allows for the demonstration of the light-polarization effect on numerous surface structures with a minimum amount of measurements. Note that the SNOM local photocurrent measurements presented in this section are recorded with the wavelength 658 nm, nonetheless the comparison between the simulation results and the measurement results in this section is still valid, as it was shown in Section 4.3 that similar local light coupling effect is expected for all wavelengths in the spectral range $\lambda = 473\,\mathrm{nm}$ – $\lambda = 780\,\mathrm{nm}$.

Figure 4.9 (a) shows the topography image of the measured area with a size of $9\,\mu\mathrm{m} \times 9\,\mu\mathrm{m}$. The array of surface structures has a period of 500 nm. Figure 4.9 (b) and (c) show the corresponding SNOM photocurrent images of the area recorded with x-polarized light and y-polarized light, respectively. The polarization directions are indicated with the white arrows in the images. In all photocurrent images, the photocurrent signal is normalized by the corresponding average value and the images are displayed in the same relative scale. Both photocurrent images exhibit clear periodic patterns, which seem to correlate to the periodic surface textures. In order to visualize this correlation more clearly, zoom-in images of the same field with an area of $1\,\mu\mathrm{m} \times 1\,\mu\mathrm{m}$ are extracted from the respective photocurrent images and displayed below them. The gray dotted squares illustrate the contours and the positions of the four surface structures contained in this area. In accordance with the investigation results obtained from the SNOM photocurrent measurements of the flat μc-Si:H thin-film solar cell, for both light polarizations, the local photocurrent response is lower at topographic maximums, i.e. on top of the periodic structures, while the local photocurrent response is higher at topographic minimums, i.e. in the surrounding grooves between the periodic structures. This is the evidence that also for the periodically textured a-Si:H thin-film solar cell, the local light coupling efficiency has the dominating influence on the local photocurrent signal. For both polarization directions, the global variation of the photocurrent signal accounts for $\sim \pm 20\%$ around the average value. On a local scale (one groove protrusion with the surrounding grooves), the min-max contrast of the photocurrent signal varies in a range of 20% – 25% on the measured field.

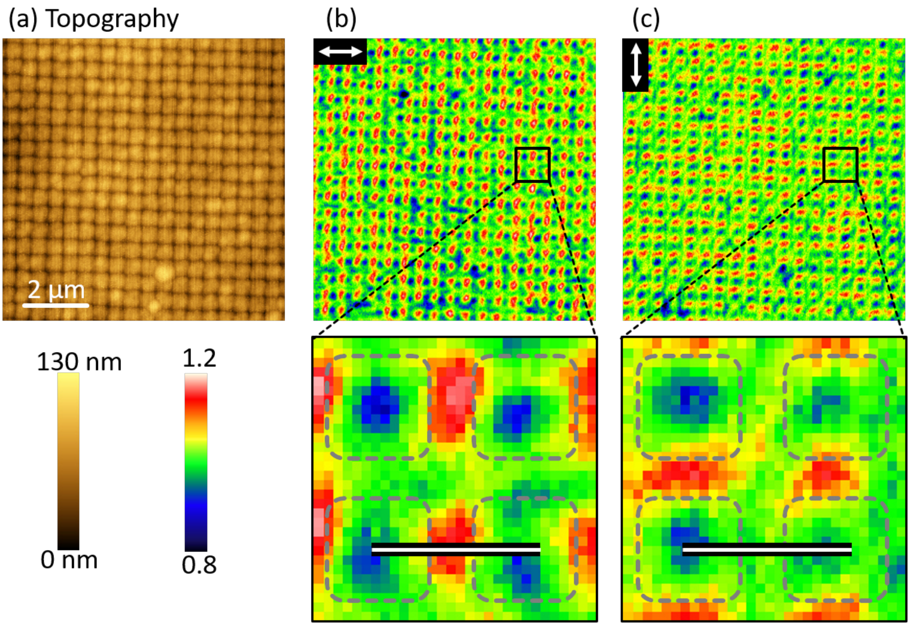

Figure 4.9: SNOM photocurrent measurement results from the a-Si:H thin-film solar cell with a scan field of 9 µm × 9 µm. (a) Topography image of the measured area. The periodic structures have a pitch of 500 nm. (b) - (c) SNOM photocurrent images from the area in (a) recorded at $\lambda = 658\,\text{nm}$. The incident light is (b) x-polarized and (c) y-polarized, respectively. In all SNOM photocurrent images, the photocurrent is normalized by the average value and the images are displayed in the same relative range (0.8 – 1.2). For better visualization of the correlation between the photocurrent signal and the periodic structures as well as the light polarization directions, below each SNOM photocurrent image of the individual light polarization, a zoom-in image with an area of 1 µm × 1 µm is shown. The zoom-in images originate from the same field of the solar cell, whereas the gray dotted squares indicate the positions of the periodic surface structures. The black/white-lines in the zoom-in phocurrent images denote the position the selected line scans, which are shown in Fig. 4.10.

Although the photocurrent images for both polarization directions exhibit periodic patterns, in the zoom-in images, the difference between the patterns in the two photocurrent images becomes obvious. In the photocurrent images in Fig. 4.9 (b), where x-polarized light is applied, the photocurrent response in the grooves between two horizontally aligned periodic structures is remarkably higher than the photocurrent response in the grooves between two vertically aligned periodic structures. The contrary behavior of the photocurrent response is observed in Fig. 4.9 (c), where y-polarized light is applied: the photocurrent response in the grooves between two vertically aligned periodic structures is remarkably higher than the photocurrent response in the grooves between two horizontally aligned periodic structures. According to the conclusion made based on the FDTD simulation results presented in this section, the local light coupling efficiency is enhanced for that light-polarization direction which accords with the preferential orientation of the topographic structure. The correlation between the local photocurrent signal and the topography observed in Fig. 4.9 (b) and (c) is in perfect agreement with the conclusions drawn from the simulation results. On the whole measured field shown in Fig. 4.9 (a), the contrast between the photocurrent signal in the groove and that on the surrounding structures increases from $\sim < 10\%$ for y-polarized light to $\sim > 20\%$ for x-polarized light.

Figure 4.10 presents a quantitative comparison of the simulation results (Fig. 4.10 (a)) of the flat μc-Si:H thin-film solar cell and the measurement results (Fig. 4.10 (b)) of the a-Si:H thin-film solar cell. While the results for x-polarized light are depicted by empty circles containing a horizontal line, the results for y-polarized light are depicted by empty circles containing a vertical line. Figure 4.10 (a) shows the normalized transmitted intensity I_T as a function of the four probe positions in the half-space configuration for the wavelength $\lambda = 780\,\mathrm{nm}$. For a better attribution of I_T to the probe positions, i.e.topographic features, a horizontal line scan through the center of the idealized topographic structure is plotted in the diagram by a black dashed line. Figure 4.10 (b) shows horizontal line scans through the middle of an representative groove between two periodic structures from the topography and the SNOM photocurrent measurements. The position of the line scans through the selected groove and the neighboring structures is indicated with a black/while-line in the zoom-in photocurrent images in Figure 4.9 (b) and (c).

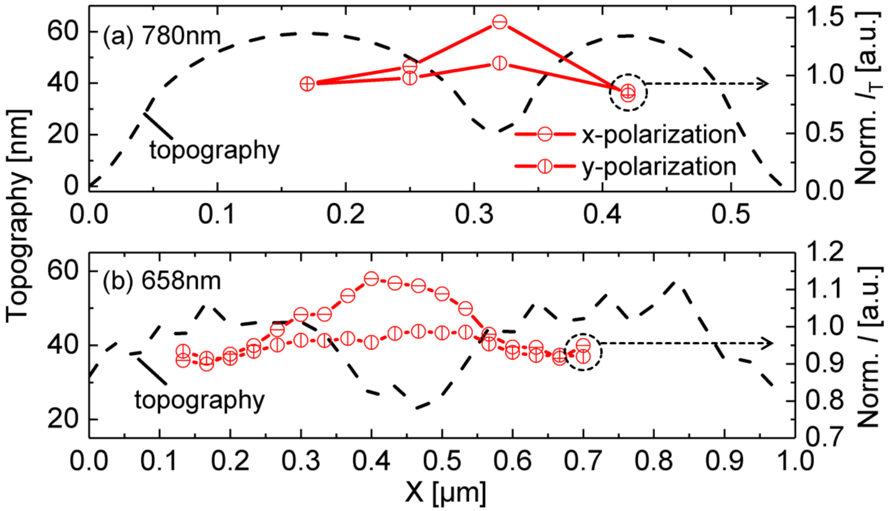

Figure 4.10: (a) Normalized transmitted intensity I_T, taken from the simulation results of the flat μc-Si:H thin-film solar cell, in case of x-polarization (empty circle with horizontal line) and in case of y-polarization (empty circle with vertical line) in the half-space configuration for the wavelength $\lambda = 780\,\mathrm{nm}$. The black dashed lines in the diagram represents the line scan through the center of the idealized topographic structure. (b) Horizontal line scans through an exemplary groove of the a-Si:H thin-film solar cell, whose position is marked in Fig. 4.9. The line scans are extracted from the topograhpy image (black dashed line), the photocurrent image recorded with x-polarized light (empty circle with horizontal line) and the photocurrent image recorded with y-polarized light (empty circle with vertical line), respectively.

In both diagrams in Fig. 4.10, the transmitted intensity or the local photocurrent signal at the topographic minimum between surface structures is significantly enhanced for x-polarized light compared to y-polarized light, hence the simulation results are very well reproduced and confirmed by the SNOM photocurrent measurements. While at the topographic minimum the intensity contrast between different light polarizations accounts for $\sim 36\%$ in the simulation, the photocurrent contrasts account for $\sim 15\%$ in the measurements. This decrease in the contrast can be explained by two reasons: on the one hand, the topographic structures in the measurements differ from the idealized structure in the FDTD simulations both in shape and size. On the other hand, as already mentioned in Section 4.1, for the wavelength 658 nm, the parasitic light caused by scattered laser light is stronger, which leads to a reduction of contrast in all photocurrent measurements conducted with this wavelength.

In summary, for topographic structures with a preferential orientation, the polarization direction of the incident light has a significant influence on the local light coupling efficiency at positions exhibiting rotational asymmetry (e.g. at topographic minimums between surface structures). Moreover, enhanced light coupling efficiency can be achieved if the light-polarization direction matches the preferential orientation of the topographic structures.

4.5 Possible origin of the topography-dependent local light coupling efficiency

So far, the local light coupling efficiency has been identified as the main optical mechanism determining the local photocurrent response in the presented SNOM photocurrent measurements, also the correlation between the local light coupling efficiency and the topographic structure, as well as the effect of the light polarization on the local light coupling efficiency has been extensively analyzed. This section provides a discussion about the possible origin of the influence of different topographic structures on the local light coupling efficiency.

Both, the SNOM photocurrent measurements and the simulation results have shown the same correlation: the local light coupling efficiency is higher at topographic minimums and is lower at topographic maximums. However, the topograhic height does not likely have a direct influence on the local light coupling efficiency, but rather the curvature of the local topography.

Figure 4.11 (a) shows the same topography image of the flat μc-Si:H thin-film solar cell with an area of 8 µm × 8 µm from Fig. 4.2. From this topography image, the local curvature at every pixel is calculated and subsequently the corresponding curvature image is created and depicted in Fig. 4.11 (b). The local curvature is defined as the second derivative of the local topography, which is composed of the pixel at the target position and the 8 surrounding pixels. In order to eliminate possible artifacts in the curvature image due to the noise or spikes in the topography image, the topography image is smoothed with a 5 × 5 Gaussian filter prior to the calculation of the curvature image. Figure 4.11 (c) and (d) show the corresponding SNOM photocurrent images from the area in (a) recorded with the wavelengths 473 nm and 780 nm, respectively. A clear correlation between the photocurrent images and the local-curvature image can be observed: The local photocurrent is higher when the local topography exhibits negative curvature, while the photocurrent is lower when the local topography exhibits positive curvature. This correlation is further visualized in Fig. 4.12, where the normalized photocurrent is plotted as a function of the local curvature for both $\lambda = 473\,\mathrm{nm}$ and $\lambda = 780\,\mathrm{nm}$, respectively. In order to avoid the disturbing influence of the upper rectangular area from the photocurrent image recorded with $\lambda = 473\,\mathrm{nm}$ on the analysis, this area ($\sim 8\,\mu\mathrm{m} \times 1\,\mu\mathrm{m}$) is excluded from all the images prior to creating the correlation plot. The fact that the correlation plot of $\lambda = 473\,\mathrm{nm}$ resembles that of $\lambda = 780\,\mathrm{nm}$ in both, the manner and the strength, provides further indication for the independence of the local light coupling of the wavelength.

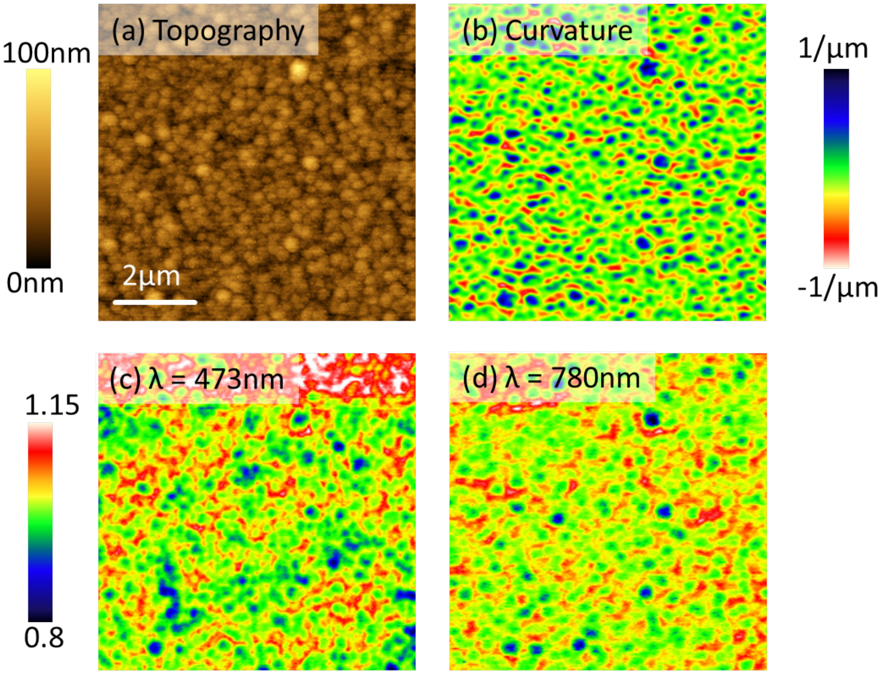

Figure 4.11: (a) SNOM topography image of the flat μc-Si:H thin-film solar cell from a scan field of 8 µm × 8 µm. (b) Image of the local curvature created from the topography image in (a). (c) and (d) SNOM photocurrent images from the area in (a) recorded with $\lambda = 473\,\mathrm{nm}$ and $\lambda = 780\,\mathrm{nm}$, respectively. In all SNOM photocurrent images, the photocurrent is normalized by the average value and the images are displayed in the same relative range $(0.8 - 1.15)$. A correlation between the local curvature image and the SNOM photocurrent images is clearly seen.

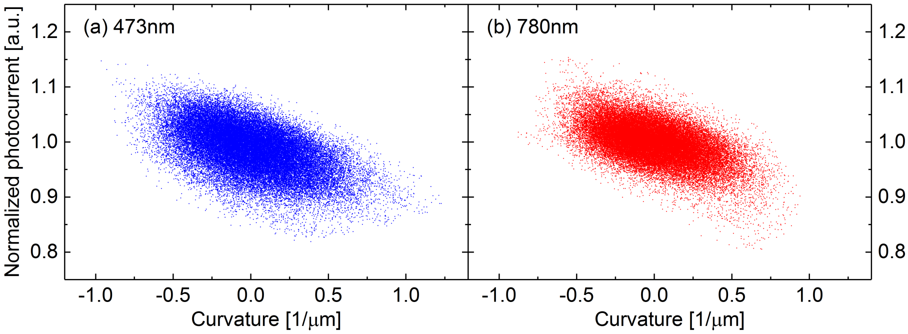

Figure 4.12: Correlation plots of the normalized photocurrent and the local curvature for the wavelengths (a) $\lambda = 473\,\mathrm{nm}$ and (b) $\lambda = 780\,\mathrm{nm}$. The similarity between the two plots suggests that, as expected, both the kind and the strength of the correlation are independent of the wavelength.

Now that the local curvature of the surface topography is identified as the main factor determining the local light coupling efficiency, the remaining question is where this correlation originates from. A conceivable explanation is illustratively shown in Fig. 4.13. Both schematics in (a) and (b) are zoom-in captures of the same region from the FDTD simulation domain, displaying the SNOM probe tip and the two surface structures. In Fig. 4.13 (a), the probe is situated above the larger partial sphere, while in Fig. 4.13 (b), the probe is situated between the partial spheres. The red spheres with a diameter of $\sim 100\,\mathrm{nm}$ in both schematics represent the optical near-field in the vicinity of the probe apex. As indicated by the black dotted lines, at positions with negative curvature (local minimum), the surface area interacting with the optical near-field seems significantly larger than in the case of positive curvature (local maximum), thus leading to higher light transmittance into the absorber. This explanation would also apply for the effect of the light polarization on the local light coupling efficiency: at the topographical minimum between two neighboring surface structures, if the light polarization direction aligns to the preferential orientation of the surface structures, i.e. along the connecting axis of the two structures, the optical near-field can interact with a larger surface area due to its elongated form in the polarization direction.

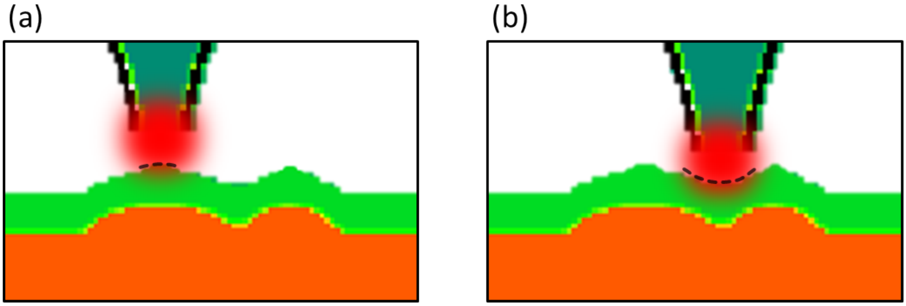

Figure 4.13: Schematics showing how the local surface curvature could influence the local light coupling efficiency when the probe is placed (a) above the local maximum and (b) above the local minimum, irradiating different areas of the surface with the optical near-field. For an accurate illustration, the schematics (without the red light spheres) are directly created from zoom-in captures of the FDTD simulation domain.

4.6 Conclusion

In this chapter, an extensive investigation of the optical process in the photocurrent generation with an a-SNOM was presented. Both, the SNOM local photocurrent measurements and the FDTD simulations, were performed with a flat μc-Si:H thin-film solar cell. Subsequently, the experimental results and the theoretical results were compared to each other. As a result, the local light coupling was identified as the dominating optical mechanism determining the local photocurrent response. In addition, the local light coupling efficiency strongly correlates to the local topography: at local topographical minimums, the light coupling efficiency can be up to $\sim 30\%$ higher than that at local topographical maximums. This behavior can be attributed to the difference of surface areas interacting with the optical near-field, which is larger in the case of a local topographical minimum. Furthermore, the effect of the light polarization on the local light coupling efficiency was examined both, theoretically and experimentally, as well. By applying light with parallel and perpendicular polarization directions with regard to the orientation of the surface structures of the solar cell, it was found that at positions with a high rotational asymmetry (e.g. at the local minimum between two neighboring surface structures), the local light coupling efficiency significantly increases if the light polarization aligns along the preferential orientation of the surface structures. In the presented simulations, the contrast between the light coupling efficiencies of perpendicular light polarizations can become larger than 30%.

5 Investigation of the poly-Si LPC thin-film solar cell

In the previous chapter, it was demonstrated that in case of a homogeneous absorber, the generation of local photocurrent with an a-SNOM as the illumination source is dominated by optical processes, i.e. local light coupling, which again strongly depends on the variation of the local topography. This chapter focuses on the investigation of electrical processes in the generation of local photocurrent. This requires the application of a solar cell appropriate for this purpose: a flat polycrystalline silicon thin-film solar cell fabricated by liquid phase crystallization (LPC). Section 5.1 shortly introduces the flat poly-Si LPC thin-film solar cell and elaborates on the choice of such a sample for the characterization of electrical processes. Section 5.2 presents the SNOM photocurrent measurement results of the flat LPC solar cell with three different wavelengths (473 nm, 658 nm and 780 nm). In Section 5.3, FDTD simulations with an identical layer configuration as that of the real LPC solar cell are performed for the same wavelengths. The results of the FDTD simulations provide optical parameters, which serve as the input parameters for the subsequent electrical simulations described in Section 5.4. Finally, Section 5.5 delivers a discussion of the results from the electrical simulations. Based on the fitting to the measurement results, characteristic electrical parameters are deduced.

5.1 Flat poly-Si LPC thin-film solar cell

As shown in Chapter 4, topographical features on the surface of the sample would greatly influence the local light coupling, i.e. the local photocurrent response.

Hence, the investigation of the electrical processes with SNOM local photocurrent measurement requires a solar cell with a flat surface while containing local electrical inhomogeneities inside the absorber. The poly-Si LPC thin-film solar cell, with its nominally flat surface (shown in Section 5.2) and grain boundaries, serves as an appropriate candidate. Most grain boundaries have been shown to have a negative impact on the electrical properties of the solar cell due to the recombination of minority carriers at the grain boundaries [149–154].

The flat LPC thin-film solar cell investigated in this thesis was friendly provided by the group of Professor Christiane Becker from the Helmholtz-Zentrum Berlin. Figure 5.1 illustrates the layer structure of the sample. On a flat glass substrate, an interlayer consisting of 250 nm SiO_x, 80 nm SiN_x and 20 nm SiO_x is coated by reactive RF-magnetron sputtering. This interlayer serves multiple purposes, such as diffusion barrier, surface passivation, anti-reflective layer, etc. [155]. In the next step, 6.5 µm intrinsic silicon absorber in amorphous or nanocrystalline form is deposited on the interlayer via high rate electron beam evaporation. The doping of the intrinsic absorber layer is achieved by sputtering a thin layer ($\sim$ 15 nm) of n-doped hydrogenated amorphous silicon (a-Si:H(n)) on top using PECVD. After the liquid phase crystallization, the n-doped poly-Si absorber is covered with 5 nm a-Si:H(i) buffer and 10 nm a-Si:H(p) emitter layer using PECVD. Afterward, an indium tin oxide (ITO) layer of 80 nm thickness is sputtered on top of the layer stack as the transparent emitter contact. In order to define the active area of the cell and more importantly, contact the absorber, a square area of 8 mm × 8 mm is shadow-masked. Subsequently, the surrounding unmasked ITO, as well as the a-Si:H(i/p) emitter layer are removed by wet etching. The absorber contact consisting of 50 nm Ti, 50 nm Pd and 1 µm Ag is then deposited on the poly-Si absorber using electron beam evaporation. At last, Ag finger electrodes are deposited on the ITO *via* thermal evaporation. More detailed descriptions of the fabrication process can be found in [156–158]. The grain sizes of poly-Si thin-film solar cell fabricated by liquid phase crystallization can reach several mm [159, 160].

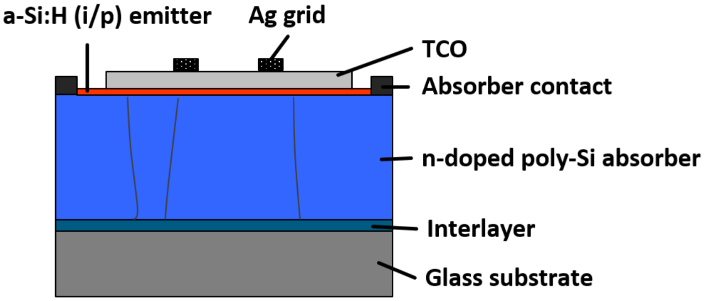

Figure 5.1: Schematic showing the layer structure of the measured flat polycrystalline silicon thin-film solar cell, which was fabricated by liquid phase crystallization.

5.2 SNOM photocurrent measurement results

SNOM photocurrent measurements were performed on a scan field of 5 µm × 10 µm with three different wavelengths: 473 nm, 658 nm and 780 nm. Figure 5.2 (a) shows the topography image of the measured area. Aside from the two line features, the surface does not exhibit any distinct topographic structures. While the top line feature appears to be a narrow trench, which very likely points to a grain boundary, the bottom one appears to be a single step with a step height of $\sim$ 20 nm. Figure 5.2 (b) – (d) show photocurrent images from the same area for different wavelengths. In all photocurrent images, the photocurrent signal is normalized by the corresponding maximum value and the images are displayed in the same relative scale $(0.35 - 1)$. The black rectangle in Fig. 5.2 (a) denotes the area, from which the averaged photocurrent signal profiles are extracted and discussed in Section 5.5.

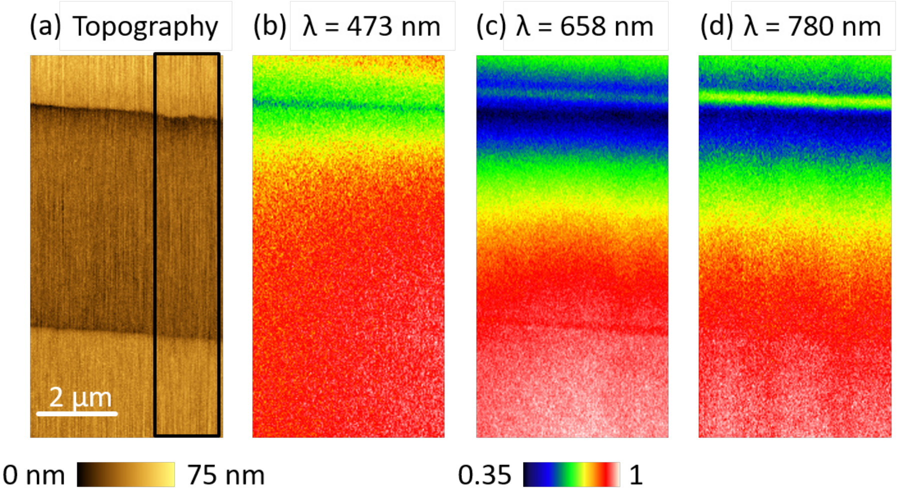

Figure 5.2: SNOM photocurrent measurement results of the flat LPC solar cell from a scan field of 5 µm × 10 µm. (a) Topography image of the measured area. Two line features are visible in the image. The upper one seems to be a grain boundary, while the lower one seems to be a simple step. The step height is ∼ 20nm. (b)-(d) SNOM photocurrent images from the area in (a) recorded with $\lambda = 473\,\text{nm}$, $\lambda = 658\,\text{nm}$ and $\lambda = 780\,\text{nm}$, respectively. In all SNOM photocurrent images, the photocurrent is normalized by the maximum value and the images are displayed in the same relative range $(0.35 - 1)$.

In all three photocurrent images, the step in the topography has hardly any impact on the photocurrent response, while the narrow trench shows a significant influence on the measured photocurrent. At the narrow trench, the obtained photocurrent signal is the lowest. With increasing distance from the narrow trench, the photocurrent signal gradually increases, until it reaches a “plateau level” (= 1 in the relative scale) at the bottom part of the images. This spatial variation of the photocurrent signal corresponds very well to the typical behavior of the electron/light beam induced current (E/LBIC) response at a grain boundary in polycrystalline silicon solar cell [161–165], providing the essential evidence that the narrow trench corresponds to a grain boundary.

Contrary to the SNOM photocurrent measurement results shown in Chapter 4, where optical effects prevail, the photocurrent signal measured at the grain boundary shows a strong wavelength dependence. On one hand, the overall contrast of the photocurrent signal increases with increasing wavelength, on the other hand, the spatial variation of the photocurrent signal across the grain boundary broadens with increasing wavelength. Especially from 473 nm to 658 nm, this contrast increase, as well as the broadening effect is clearly visible. This wavelength dependence can be explained by the wavelength-dependent absorption length of the light in the crystalline silicon. Based on the absorption coefficient data provided in [166], the absorption lengths L_{abs} of the three wavelengths are calculated as follows: $L_{\mathrm{abs,473\,nm}} \sim 0.6\,\mu\mathrm{m}$, $L_{\mathrm{abs,658\,nm}} \sim 3.9\,\mu\mathrm{m}$ and $L_{\mathrm{abs,780\,nm}} \sim 9.7\,\mu\mathrm{m}$. Due to the much larger light absorption length in case of $\lambda = 658\,\mathrm{nm}$ compared to $\lambda = 473\,\mathrm{nm}$ (by a factor of 6.5), the generated photocurrent would still be affected by the grain boundary for larger distances between the SNOM probe position and the grain boundary, leading to a broader spatial variation of the photocurrent signal.

However, for 658 nm and 780 nm, the photocurrent images appear to be similar with respect to the broadening and the global contrast. In case of 780 nm, the global contrast of the photocurrent even seems slightly reduced . A conceivable reason for this rather unexpected observation could be the bright line feature on the upper edge of the grain boundary in Fig. 5.2 (d), which would considerably offset the minimum photocurrent signal at the grain boundary to a higher value, thus reducing both, the overall contrast and the lateral extent of the spatial distribution. The same line feature is also weakly recognizable in Fig. 5.2 (c) for $\lambda = 658\,\mathrm{nm}$, nonetheless invisible in Fig. 5.2 (b) for $\lambda = 473\,\mathrm{nm}$. Although the exact origin of this line feature in the photocurrent images in Fig. 5.2 (c) und (d) was not identified in the scope of this work, some reasonable restrictions regarding its origin can be made: based on similar considerations presented in Section 4.1, the sharp edge of this bright line feature visible in Fig. 5.2 (d) despite the large absorption length suggests that the origin of it is likely of optical nature. Furthermore, unlike the topography-dependent light coupling effect discussed in Chapter 4, the bright line feature appears at the flat edge of the grain boundary and exhibits a strong wavelength dependence in addition. One conceivable scenario could be the existence of a structure with the characteristics of an optical resonator obscured below the flat surface.

So far, various publications have presented E/LBIC measurements of polycrystalline silicon solar cells. It has been shown that by fitting theoretical models to the current contrast profile across a grain boundary, two important electrical parameters of the grains can be extracted [161–165, 167–169]: the minority carrier intra-grain diffusion length L_D and the grain boundary recombination velocity S_gb. Now, having demonstrated the ability of the SNOM photocurrent measurement to detect electrical processes in the photocurrent generation, in the following sections, similar attempt is undertaken to evaluate the SNOM photocurrent images in Fig. 5.2 to derive the L_D and S_gb. Compared to EBIC and LBIC methods, the SNOM photocurrent measurement provides some unique advantages: while it does not require a vacuum chamber for the operation as the EBIC method does, it has a spatial resolution which is more than one order of magnitude smaller than the LBIC method. The typical spatial resolution of the LBIC measurement accounts for several micrometers [154, 165, 167].

5.3 Domain configuration and results of the FDTD simulations

In order to fit theoretical models to the photocurrent profiles from the measurements, various input parameters need to be either given or determined (more details will follow in Section 5.4). One important input parameter is the carrier generation volume of the beam source. Usually, the generation volume is theoretically derived and can feature various shapes, such as point source [164], spherically-symmetrical Gaussian shape [170], pear shape [171] or cubic shape [172]. In this work, the carrier generation volume is obtained *via* FDTD simulations. As demonstrated in Chapter 4, FDTD simulations provide a very accurate description of the light coupling through a SNOM aperture, as well as the light intensity propagation within the absorber. Hence, the resulting light intensity distribution inside the absorber layer corresponds to the carrier generation volume.

The FDTD simulations are performed within a three-dimensional spatial domain with the size of 15 µm × 15 µm × 10 µm. Unlike the FDTD simulations performed for the μc-Si:H thin-film solar cell, which have a domain size of 10 µm ×

10 µm × 5 µm, a larger domain size is necessary due to the larger absorber thickness of 6.5 µm. However, the larger domain size would lead to a significant increase of the computation time by a factor of ~ 5, if the spatial resolution was kept at 10 nm. Therefore, a spatial resolution of 20 nm is chosen as a trade-off. Nonetheless, as no nanoscale topographic structure is involved, the resolution of 20 nm is still sufficient. Figure 5.3 shows the cut-out with a size of 6 µm × 8 µm from the simulation-domain profile in the xz-plane. The layer structure corresponds to that of the real poly-Si LPC thin-film solar cell measured in the experiment. From the bottom to the top, the layer stack consists of 260 nm glass layer, 6.5 µm crystalline silicon absorber and 80 nm TCO. The approximation of the interlayer by a glass layer is justified by their similar optical properties. The use of crystalline silicon as the absorber bases on the assumption, that the light propagation, thus the light intensity distribution is not or barely affected by the grain boundaries in a real poly-Si LPC thin-film solar cell. The space above the sample comprises of air. The SNOM probe providing local illumination has the idealized geometry of a truncated cone. The sidewall angle of the cone is 15° with respect to the surface normal. The metal coating of the SNOM probe is approximated by the PEC layer. Instead of 30 nm as in the simulations for the μc-Si:H thin-film solar cell, the coating thickness accounts for 60 nm, which corresponds to 3 pixels in the simulation domain. The choice of 3 pixels as the minimum thickness for the coating is to ensure a seamless sidewall and prevent any light leakage due to the sloped sidewall. Also here, PMLs with a thickness of 0.6 µm are defined at the boundaries of the 3D simulation domains to prevent light reflection.

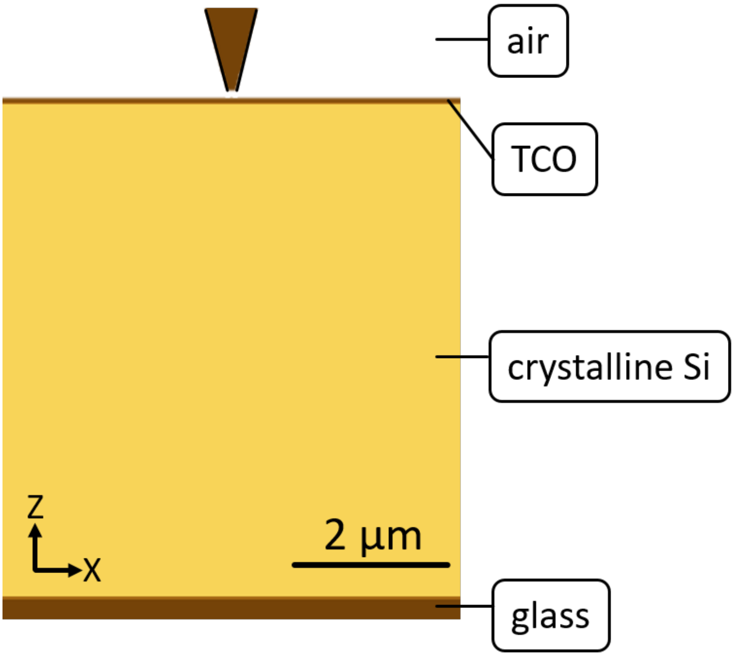

Figure 5.3: Cut-out from the profile (in xz-plane) of the simulation domain with a similar layer stack as the flat poly-Si LPC thin-film solar cell. The cut-out has a size of 6 µm × 8 µm, whereas the full dimension of the simulation domain is 15 µm × 15 µm × 10 µm. The glass layer has a thickness of 260 nm, the crystalline silicon absorber has a thickness of 6.5 nm and the top TCO has a thickness of 80 nm.

Since the results of the FDTD simulations are further used as input parameters in the subsequent electrical modeling, it is crucial to avoid any possible propagating error, e.g. from inaccurate assumptions in the FDTD simulations. Therefore, the aperture diameter of the SNOM probe was varied between 80 nm and 200 nm in the FDTD simulations to examine the sensitivity of the results to the aperture diameter, as it is the parameter with the largest uncertainty in regard to the experiment. At this position it is noted in advance that, in the given aperture diameter range, no significant deviations regarding the intensity distribution were observed between the respective simulation results. Accordingly, all simulation results presented in this chapter are exemplarily chosen from the aperture diameter 120 nm.

In accordance with the experiments, FDTD simulations have been performed for the wavelengths 473 nm, 658 nm and 780 nm, respectively. As a visual demonstration of the simulation results, Figure 5.4 shows cut-outs of the intensity profiles of the xz-plane centrally crossing the simulation domain for $\lambda = 473\,\mathrm{nm}$, $\lambda = 658\,\mathrm{nm}$ and $\lambda = 780\,\mathrm{nm}$, respectively. The cut-outs have a size of $15\,\mu\mathrm{m} \times 8\,\mu\mathrm{m}$. For clarity, only the intensity distribution in the crystalline silicon layer is displayed in logarithmic scale. For all wavelengths, the intensity is normalized by the corresponding maximum value. The red dotted lines indicate the shape and the position of the probe, as well as the interfaces of the crystalline silicon layer. As expected, at the two long wavelengths, the light propagates further in the crystalline silicon layer and has a broader distribution as well due to the longer absorption lengths. However, the observed light propagation range does not seem to match the calculated absorption lengths. This is explained by the fact that the presented intensity profiles are extracted from only one slice along the y-axis of the simulation domains, therefore do not contain the total intensity. As can be seen later in Fig. 5.5, once the total intensity is taken into account, the obtained intensity profiles will correspond to the individual wavelength much better.

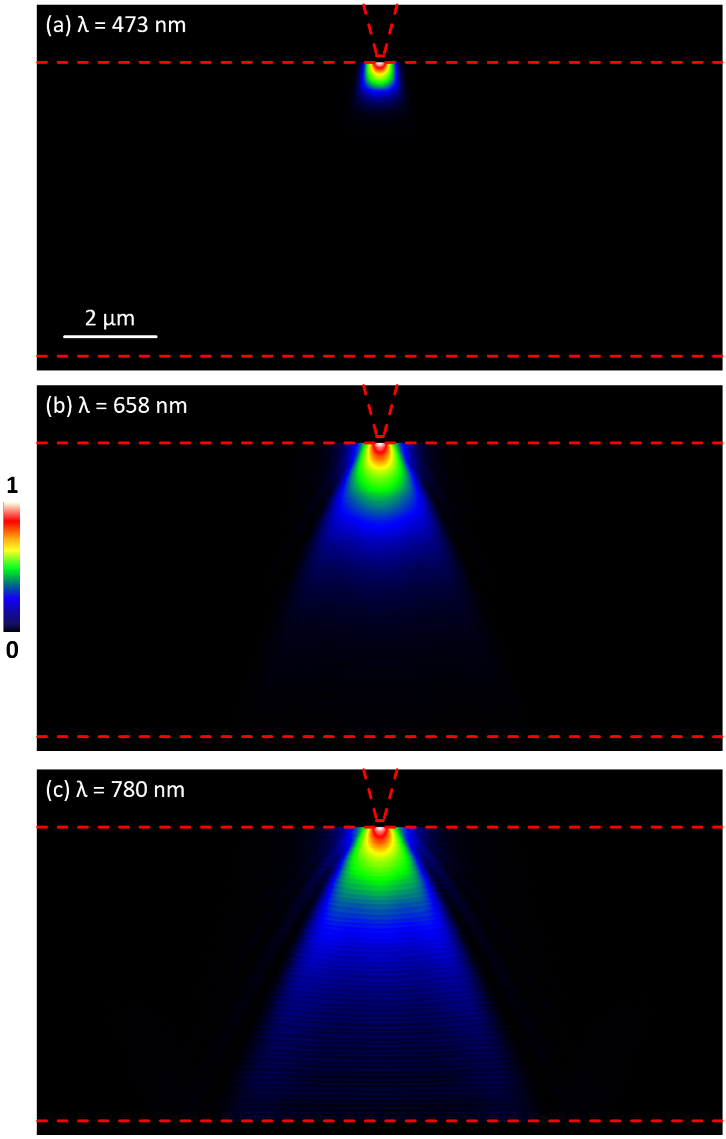

Figure 5.4: Logarithmic intensity profiles of the central xz-plane from the simulation domain for (a) $\lambda = 473\,\mathrm{nm}$, (b) $\lambda = 658\,\mathrm{nm}$ and (c) $\lambda = 780\,\mathrm{nm}$, respectively. All profiles have a size of $15\,\mu\mathrm{m} \times 8\,\mu\mathrm{m}$. For clarity, only the intensity distribution in the crystalline silicon layer is displayed. The intensity is normalized by the individual maximum value for each wavelength. The red dotted lines outline the contours of the probe and the interfaces of the crystalline silicon layer.

Given the relative straightness of the measured grain boundary, a translational invariance of the measured sample along the y-axis can be assumed, which reduces the three-dimensional problem to a two-dimensional one. For this purpose, the 3D intensity distribution is integrated over the y-axis and projected on the xz-plane. The thus created generation volumes, or rather generation profiles, will serve as input parameters for the subsequent electrical simulations. Note that, also in this chapter, unpolarized light is assumed by averaging the simulation results from both polarization directions.

Figure 5.5 shows the integrated light intensity distributions inside the crystalline silicon layer, i.e. the generation profiles for $\lambda = 473\,\mathrm{nm}$, $\lambda = 658\,\mathrm{nm}$ and $\lambda = 780\,\mathrm{nm}$, respectively. Also here, logarithmic scale is applied. The cut-outs have a size of $13\,\mu\mathrm{m} \times 6.5\,\mu\mathrm{m}$.

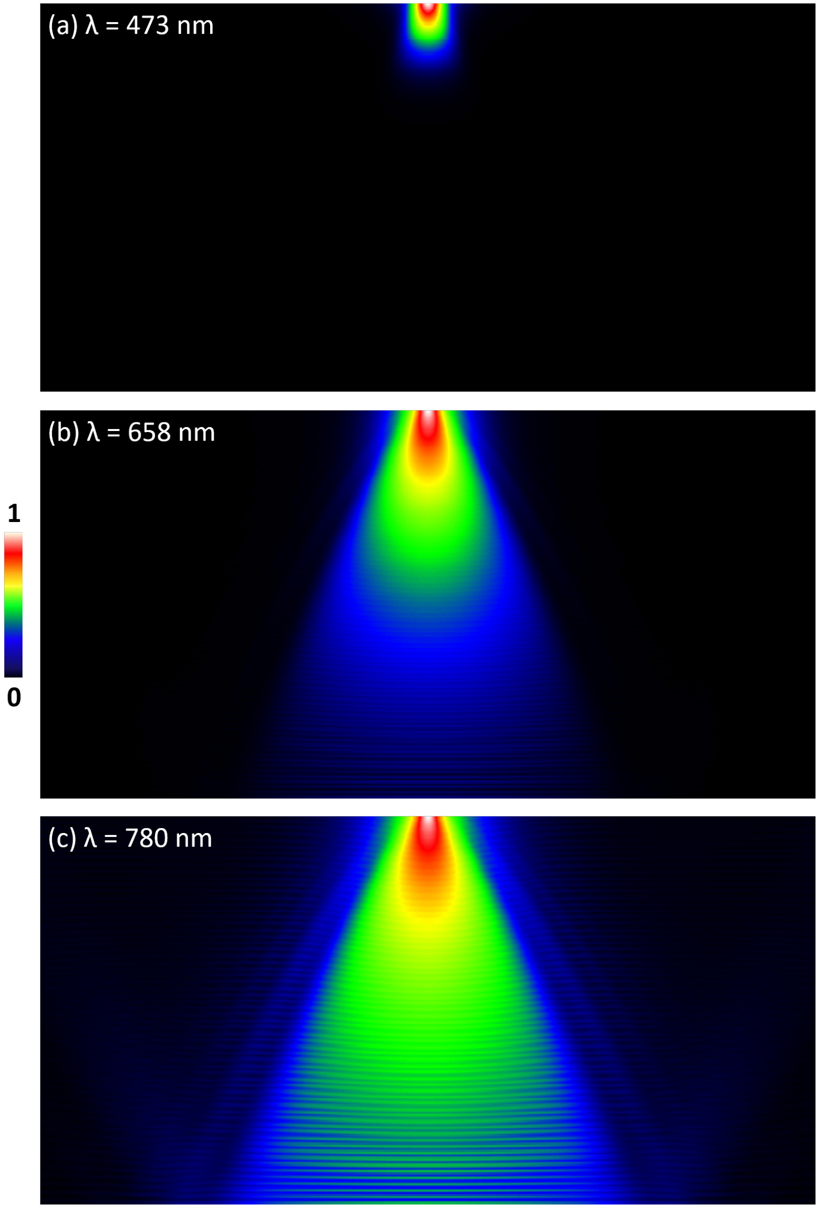

Figure 5.5: Logarithm of integrated generation profiles for (a) $\lambda = 473\,\mathrm{nm}$, (b) $\lambda = 658\,\mathrm{nm}$ and (c) $\lambda = 780\,\mathrm{nm}$, respectively. The profiles have a size of $13\,\mu\mathrm{m} \times 6.5\,\mu\mathrm{m}$. In addition, The intensity is normalized by the individual maximum value for each wavelength and the same scale is applied for all three images.

For each wavelength, the intensity is normalized by the corresponding maximum value. Moreover, the same scale is applied in all images. Therefore, compared to Fig. 5.4, the integrated intensity distributions in Fig. 5.5 deliver a much more accurate depiction of the absorption length of the respective wavelengths. For $\lambda = 473\,\mathrm{nm}$ ($L_{\mathrm{abs},473\,\mathrm{nm}} \sim 0.6\,\mu\mathrm{m}$), the intensity distribution reaches a depth of $\sim \frac{1}{5}$ of the entire layer thickness. For $\lambda = 658\,\mathrm{nm}$ ($L_{\mathrm{abs},658\,\mathrm{nm}} \sim 3.9\,\mu\mathrm{m}$), the intensity distribution reaches the bottom of the crystalline silicon layer. For $\lambda = 780\,\mathrm{nm}$ ($L_{\mathrm{abs},780\,\mathrm{nm}} \sim 9.7\,\mu\mathrm{m}$), not only does the intensity distribution propagate to the back side of the crystalline silicon layer, also the reflected intensity and interference patterns are visible.

For further calculations with the generation profiles, the intensity is normalized such, that the total integrated intensity over the entire crystalline silicon layer yields 1. This way, the resulting generation profiles can be directly applied in the following electrical simulations and simplify the calculations.

5.4 Basic principles of the electrical simulations

The electrical modeling and the fitting to the experimental photocurrent signal profiles are contributed by Professor Uwe Rau. This section briefly outlines the basic principles and the configuration of the electrical simulations.

The photogenerated short circuit current can be written as [173]

$$J = q \int_0^{V_0} f(\boldsymbol{r})\, g(\boldsymbol{r})\, \mathrm{d}V \tag{5.1}$$

where q denotes the elementary charge, $f(\boldsymbol{r})$ denotes the collection probability of a photogenerated carrier at position $\boldsymbol{r}$, $g(\boldsymbol{r})$ describes the photogeneration profile and V_0 denotes the entire volume of the absorber. Furthermore, according to [173–175], the collection probability $f(\boldsymbol{r})$ is equal to the dark excess carrier concentration at $\boldsymbol{r}$ normalized by the dark excess carrier concentration at the cell junction. Hence, the photogenerated current can be written as

$$J = q \int_0^{V_0} n_{\mathrm{D}}(\boldsymbol{r})\, g(\boldsymbol{r})\, \mathrm{d}V \tag{5.2}$$

where $n_{\mathrm{D}}(\boldsymbol{r})$ denotes the normalized dark minority-carrier density.

The electrical modeling is performed on the basis of the equation 5.2. While the normalized generation profiles $g(\boldsymbol{r})$ for different wavelengths are obtained from the FDTD simulations as described in Section 5.3, the dark minority-carrier concentration can be calculated by solving the minority carrier diffusion equation (cf. Eq. 2.53) in Fourier space [176,177]. According to [176], the excess minority carrier density can be expanded into a Fourier series with respect to the coordinates x and y for the three-dimensional case

$$n(\boldsymbol{r}) = n(x,y,z) = \sum_{k,l=-N}^{N} \hat{n}(k,l,z)\, e^{ikx}\, e^{ily} \tag{5.3}$$

where N represents the number of the highest Fourier component. The general solution for each Fourier component then can be written as

$$\hat{n}(k,l,z) = A(k,l)\cosh\Big(\frac{z}{L_{\mathrm{D}}}\Big) + B(k,l)\sinh\Big(\frac{z}{L_{\mathrm{D}}}\Big) + g(k,l,z)\,\tau \tag{5.4}$$

where L_{D} denotes the minority carrier bulk diffusion length and τ denotes the minority carrier bulk lifetime. A and B are appropriate coefficients in the Fourier decomposition. For the present work, equation 5.4 can be further simplified to

$$\hat{n}(k,l,z) = A(k)\cosh\Big(\frac{z}{L_{\mathrm{D}}}\Big) + B(k)\sinh\Big(\frac{z}{L_{\mathrm{D}}}\Big) \tag{5.5}$$

due to the reduction to the xz-plane and the fact that the solution sought for is for the special case of dark minority carriers ($g(k,l,z) = 0$).

For the numerical calculations, further input parameters, such as the electron diffusion coefficient D_{n}, the grain boundary recombination velocity S_{gb} and the minority carrier diffusion length L_{D} are required aside from the generation profile. Furthermore, as the light with $\lambda = 780\,\mathrm{nm}$ would reach the c-Si/glass interface on the back side, a back surface recombination velocity S_{back} is introduced as well. In this work, $D_{\mathrm{n}} = 7\,\mathrm{cm}^2/\mathrm{s}$ and $S_{\mathrm{back}} = 10^4\,\mathrm{cm/s}$ [178] are chosen as suitable values for n-doped polycrystalline silicon. The electrical parameters characterizing the solar cell and the grain boundary, the minority carrier bulk diffusion length L_{D} and the grain boundary recombination velocity S_{gb}, are the ones to be determined by the fitting process described in this and the next section. For this purpose, both parameters are varied within a proper range: while L_{D} is altered from $1\,\mu\mathrm{m}$ to $10\,\mu\mathrm{m}$ in 11 steps, S_{gb} is altered from $3 \times 10^{5}\,\mathrm{cm/s}$ to $8 \times 10^{5}\,\mathrm{cm/s}$ in 10 steps. The comparison between the simulation results and the measurement results afterward yields the appropriate values for L_{D} and S_{gb}.

The electrical simulations are performed for an absorber with a width of $\Delta x = 50\,\mu\mathrm{m}$ and a thickness of $\Delta z = 6.5\,\mu\mathrm{m}$. The grain boundary is approximated by a vertical line along the z-axis throughout the whole thickness and characterized by the grain boundary recombination velocity S_{gb}. For each point of the simulation domain, equation 5.5 is solved numerically and the normalized dark minority-carrier concentration $n_{\mathrm{D}}(x, z)$ is determined. The thus obtained $n_{\mathrm{D}}(x, z)$-matrix of the simulation domain is then, in accordance with equation 5.2, element-wise multiplied by the normalized generation profile $g(x, z)$ obtained from the FDTD simulations. Subsequent summation over all elements yields the photogenerated short-circuit current. The thus obtained short-circuit current however only constitutes one single point of the simulated current profile. In order to simulate the scanning process in the measurements and calculate the complete short-circuit current profile, the position of the grain boundary is shifted along the x-axis point by point, which is analog to the process as if the light source, i.e. the generation profile was “scanned” over the absorber surface. For each new x-position, the photogenerated short-circuit current is calculated as described.

The calculations described above are performed for each wavelength. Afterward, the simulated short-circuit current profile is subtracted from the corresponding SNOM photocurrent profile point by point for each wavelength, respectively. The square sum σ^{2} of the differences for all wavelengths serves as the error measure and a figure of merit for the fitting.

This procedure is repeated for each combination of L_{D} and S_{gb} and the corresponding σ^{2} is calculated. Consequently, the combination with the smallest σ^{2} will provide the most accurate solutions for L_{D} and S_{gb}. The next section presents the results of the electrical simulations and a comparison with the experimental results.

5.5 Results and discussion of the electrical simulations

Figure 5.6 shows the normalized SNOM photocurrent signal profiles of all three wavelengths starting form the grain boundary, which are extracted from the photocurrent images in Fig. 5.2 (b) – (d), respectively. For the purpose of noise minimization, the photocurrent profiles are averaged over a width of $\sim 1{,}6\,\mu\mathrm{m}$. The area from which the averaged photocurrent profiles are obtained is indicated in Fig. 5.2 (a) with a black rectangle. For better visualization, the photocurrent profiles are shifted such, that the minimum coincides with the coordinate $x = 0\,\mu\mathrm{m}$. As already described in Section 5.2, it is clearly seen that the photocurrent profiles have a higher contrast and broader distribution for the long wavelengths 658 nm and 780 nm. The black dashed line depicts the averaged line scan of the topography from the same area and serves as a guide for the eye. The step with a height of roughly 20 nm is clearly seen at $x \sim 5.5\mu\mathrm{m}$, which only causes a marginal change of the photocurrent response for the long wavelengths.

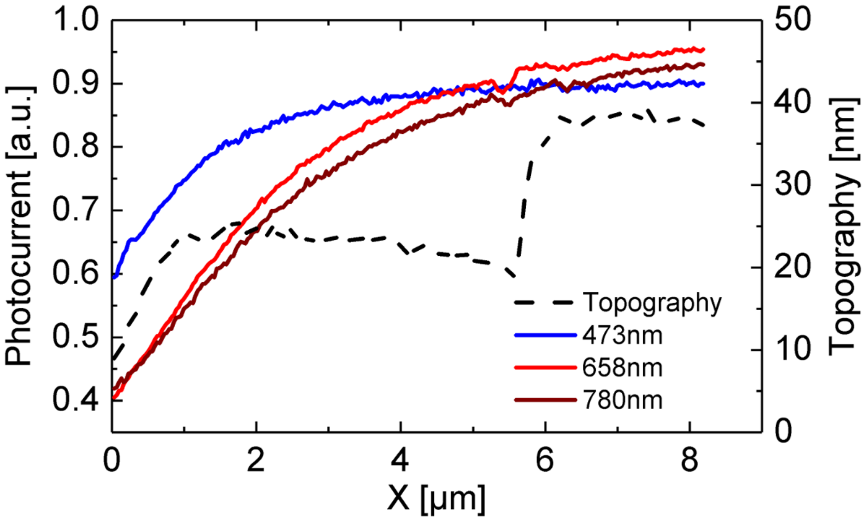

Figure 5.6: Normalized SNOM photocurrent signal profiles extracted from the photocurrent images in Fig. 5.2 (b) – (d) for all three wavelengths at the same position. The black dashed line illustrates the line scan of the topography starting from the grain boundary, where the photocurrent profiles are obtained. Both, the photocurrent profiles and the topography line scan, are the averaged results of an area with a width of ∼ 1.6 µm.

Figure 5.7 shows the two-dimensional contour plot of the error measure σ^2 with the minority carrier bulk diffusion length L_D as the x-axis and the grain boundary recombination velocity S_gb as the y-axis. The color scale bar to the right denotes the magnitude of σ^2. The continuous color map in the 2D-plot is obtained *via* interpolation. For better clarity, the color scale only applies to σ^2-values in the range from 1 to 3. while areas with σ^2-values larger than 3 are filled with white color, the black area in the middle of the contour plot contains σ^2-values smaller than 1.

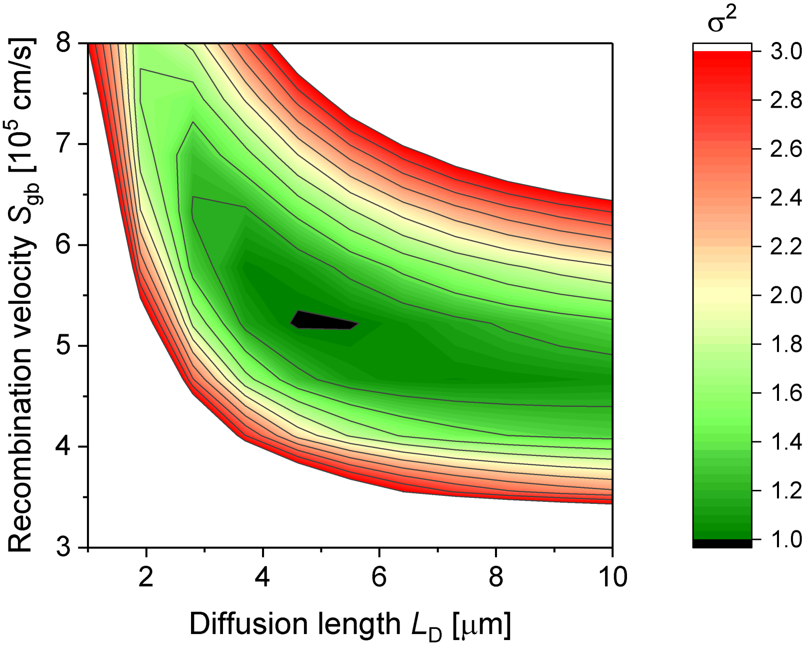

Figure 5.7: Two-dimensional contour plot of the error measure σ^2 as a function of the minority carrier diffusion length L_D and the grain boundary recombination velocity S_{gb}. The color map is only applied to σ^2-values in the range $1-3$. The white space represents all σ^2-values larger than 3 and the black area contains σ^2-values smaller than 1.

The values for the two characteristic electrical parameters for the grain boundary, the grain boundary recombination velocity S_{gb} and minority carrier diffusion length L_D, can now be easily estimated with the help of the 2D contour plot. The elongated shape of the contours along the x-axis suggest that the photocurrent signal is more sensitive to the grain boundary recombination velocity than to the minority carrier diffusion length. Only taking the black area with the smallest σ^2-values into account, the grain boundary recombination velocity S_{gb} can be narrowed down to 5.2×10^5 cm/s $-$ 5.3×10^5 cm/s with a relative high precision, while the minority carrier diffusion length L_D could range from 4.5 μm to 5.5 μm.

From all combinations of S_{gb} and L_D applied in this work, the absolute minimum of σ^2 is obtained for the pair $S_{\mathrm{gb}} = 5.2 \times 10^5\,\mathrm{cm/s}$ and $L_{\mathrm{D}} = 4.6\,\mu\mathrm{m}$, with σ^2 being 0.975. For this S_{gb}-L_{D}-combination, Figure 5.8 plots both, the measured and the calculated normalized short-circuit photocurrent as a function of the distance between the light source and the grain boundary for the wavelengths $\lambda = 473\,\mathrm{nm}$, $\lambda = 658\,\mathrm{nm}$ and $\lambda = 780\,\mathrm{nm}$, respectively. While the empty symbols depict the experimental data, the solid lines with the corresponding colors illustrate the calculated curves. The position $X = 0\,\mu\mathrm{m}$ denotes the location of the grain boundary, where both, the experimental and the theoretical curves have their minimum. Furthermore, for each wavelength, the experimental photocurrent profile is individually normalized by the minimum of the corresponding theoretical photocurrent profile, so that their minimums coincide at $X = 0\,\mu\mathrm{m}$ for better visibility.

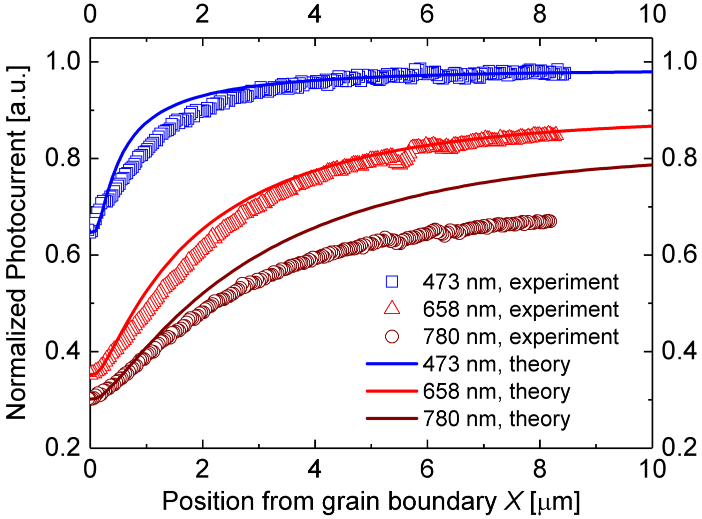

Figure 5.8: Normalized short-circuit photocurrent profiles for the wavelengths $\lambda = 473\,\mathrm{nm}$, $\lambda = 658\,\mathrm{nm}$ and $\lambda = 780\,\mathrm{nm}$ as a function of the light source position, with the grain boundary located at $X = 0\,\mu\mathrm{m}$. While the experimental photocurrent profiles are depicted with empty symbols, the calcuated photocurrent profiles are depicted with solid lines. The theoretical photocurrent profiles are generated with $S_{\mathrm{gb}} = 5.2 \times 10^5\,\mathrm{cm/s}$ and $L_{\mathrm{D}} = 4.6\,\mu\mathrm{m}$.

For the wavelengths $\lambda = 473\,\text{nm}$ and $\lambda = 658\,\text{nm}$, the calculated photocurrent profiles are in good agreement with the measured ones regarding both, the contrast and the shape. However, for $\lambda = 780\,\text{nm}$, the contrast for the experimental photocurrent profile is $\sim 20\,\%$ smaller than for the calculated profile, while the shape appears to be similar. This discrepancy between the experiment and the simulation for $\lambda = 780\,\text{nm}$ could be attributed to the bright line feature on the upper edge of the grain boundary, which is probably an optical effect. As described in Section 5.2, this bright feature could pose a positive offset to the minimum of the measured photocurrent due to its vicinity to the grain boundary, therefore reducing the measured contrast.

As a comparison, in [179], a combination of the techniques photoluminescence (PL) imaging and transient PL was applied to determine the local minority carrier diffusion length of a poly-Si LPC thin-film solar cell. The obtained diffusion lengths vary in a range of $2 - 20\,\mu\text{m}$. It is worth mentioning that, due to the different orientations or the sizes of the grains distributed among the polycrystalline silicon, the minority carrier diffusion length and the grain boundary recombination velocity could also vary locally. The calculated minority carrier diffusion length of $4.6\,\mu\text{m}$ in this work fits very well into this range. Also for the grain boundary recombination velocity, the value of $5.2 \times 10^5\,\text{cm/s}$ is in accordance with the results from [164], where an analytical expression is directly fitted to the EBIC contrast profile across a grain boundary in a solar cell made by cast polycrystalline silicon.

As a conclusion, despite the distortion by the optical feature in the SNOM photocurrent measurements, a good agreement (mainly for the wavelengths $\lambda = 473\,\text{nm}$ and $\lambda = 658\,\text{nm}$) between the measurement results and the simulation results is achieved with the presented methods. Moreover, the extracted grain boundary recombination velocity and the minority carrier diffusion length are both comparable to the values found in other references.

5.6 Conclusion

This chapter demonstrated the detection and the characterization of electrical processes in the photocurrent generation, such as diffusion and recombination, with the SNOM photocurrent measurements. A polycrystalline silicon thin-film solar cell fabricated by liquid phase crystallization, which has a nominally flat surface and contains electrical defects (grain boundaries), served as the sample. From the SNOM photocurrent measurement results of three different wavelengths (473 nm, 658 nm and 780 nm), photocurrent signal profiles were extracted and compared to the results from theoretical simulations. With the help of FDTD simulations, photogeneration profiles for all three wavelengths were created as the input parameters for the subsequent electrical simulations. The combination of FDTD simulations and electrical modeling based on the diffusion equation allows for the determination of two characteristic electrical parameters: the grain boundary recombination velocity S_{gb} and the local minority carrier diffusion length L_{D}. Both obtained values, $S_{\mathrm{gb}} = 5.2 \times 10^5\,\mathrm{cm/s}$ and $L_{\mathrm{D}} = 4.6\,\mu\mathrm{m}$, are in good agreement to the results found in other references.

6 Investigation of the randomly textured μc-Si:H thin-film solar cell

In Chapter 4, optical processes (local light coupling) in the photocurrent generation were analyzed with the SNOM photocurrent measurements. Then in Chapter 5, investigation of electrical processes (minority-carrier recombination) in the photocurrent generation was demonstrated with the SNOM photocurrent measurements. The knowledge gained from the separate studies of the optical and the electrical mechanisms allows us to understand the SNOM photocurrent measurement results of more complex solar cells, where both optical and electrical effects have a significant impact on the photocurrent generation. This chapter presents the experimental and theoretical study of such a complex solar cell: a randomly textured μc-Si:H thin-film solar cell. Section 6.1 briefly introduces the measured solar cell and describes the SNOM photocurrent measurement results with five different wavelengths ranging from 473 nm to 780 nm. Section 6.2 demonstrates the FDTD simulations with the real topography of a textured μc-Si:H thin-film solar cell. Section 6.3 provides a comparison of the FDTD simulation results to the measurement results. Finally, in Section 6.4, a particular discussion regarding the defects in the textured μc-Si:H thin-film solar cell is given.

6.1 SNOM photocurrent measurement results

As described in 2.3.4, introducing light scattering textures in silicon solar cells are an essential concept for the improvement of the light absorption in the absorber, hence the solar cell efficiency. Among the many concepts of texturing a thin-film silicon solar cell, adding random surface texture on a μc-Si:H thin-film solar cell constitutes one of most common methods. Figure 6.1 illustrates the layer structure of the textured μc-Si:H thin-film solar cell adopted for the SNOM photocurrent measurements in this work. The solar cell has the identical layer structure and deposition process as its flat analogon described in 4.1, also the thicknesses of the individual layers are kept the same. However, prior to sputtering the 250 nm thick Ag layer and the 80 nm thick ZnO:Al layer on the substrate as the back reflector, the initially flat substrate is wet-chemically etched in diluted hydrochloric acid (0.5 % HCl) to create a random texture on the substrate surface [180]. The conformal deposition of the subsequent layers on the substrate results in a similar random surface texture of the final solar cell [96].

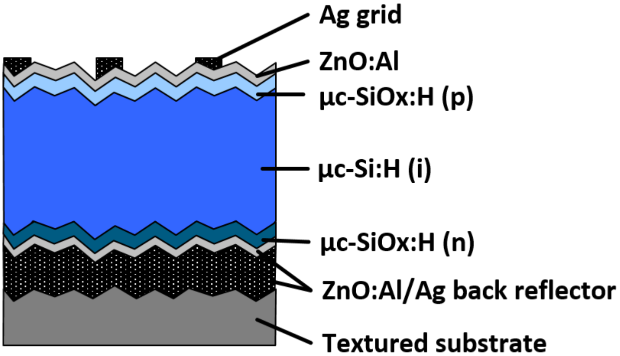

Figure 6.1: Schematic showing the layer structure of the textured μc-Si:H thin-film solar cell.

Figure 6.2 (a) shows the topography image from a scan field of 8 μm × 8 μm recorded with the SNOM. Other than the protrusions with heights of a few 10 nm observed on the flat μc-Si:H thin-film solar cell in 4.1, large, crater-like structures are now visible due to the conformal growth of the μc-Si:H absorber on the randomly textured substrate. The craters have diameters between $1\,\mu\text{m} - 3\,\mu\text{m}$ and are several 100 nm high. Additionally, the crater rims reveals fine, line-shaped trenches at many places. Figure 6.2 (b) – (f) show photocurrent images from the same area in (a) for the wavelengths 473 nm, 532 nm, 658 nm, 735 nm and 780 nm, respectively. In all photocurrent images, the photocurrent signal is normalized by the corresponding average value, then the images are displayed with the same relative scale for a simplified comparison of the local photocurrent variation between the five wavelengths.

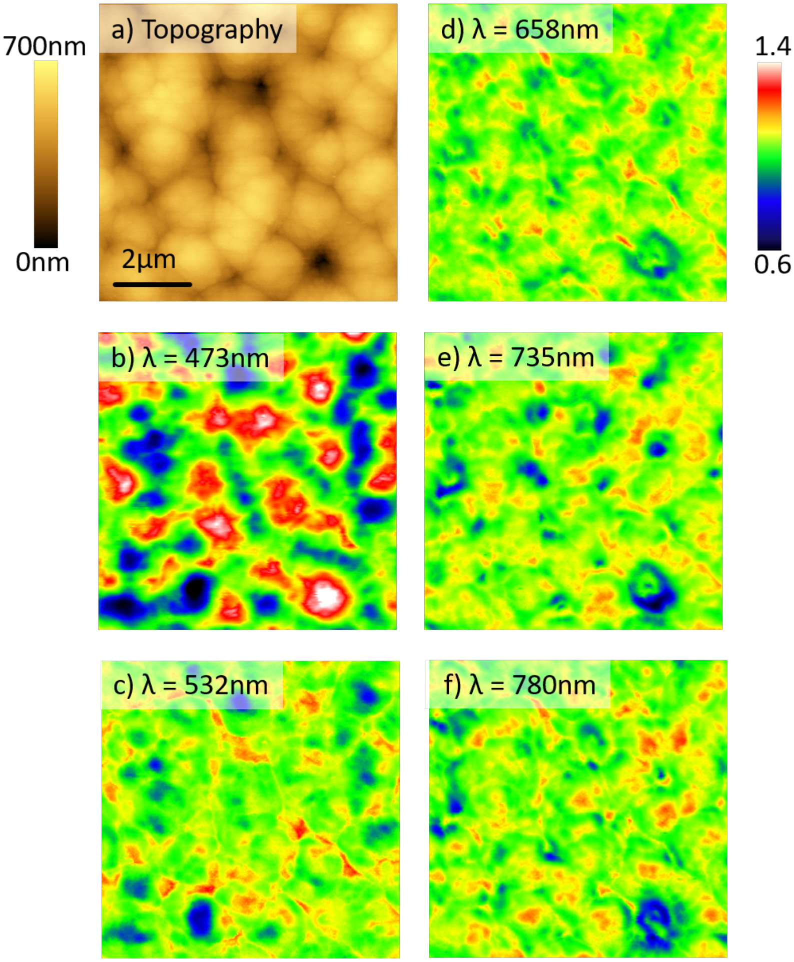

Figure 6.2: (a) SNOM topography image of the textured μc-Si:H thin-film solar cell from a scan field with size of 8 µm × 8 µm. (b)-(f) SNOM photocurrent images from the area in (a) recorded with $\lambda = 473\,\mathrm{nm}$, $\lambda = 532\,\mathrm{nm}$, $\lambda = 658\,\mathrm{nm}$, $\lambda = 735\,\mathrm{nm}$ and $\lambda = 780\,\mathrm{nm}$, respectively. In all SNOM photocurrent images, the photocurrent is normalized by the average value and the images are displayed in the same relative range $(0.6 - 1.4)$.

While the photocurrent images recorded with the four longer wavelengths have a rather similar contrast, the image recorded with 473 nm exhibits the strongest local photocurrent variation. In fact, the photocurrent image at 473 nm reveals areas with both lowest (bottom left) and highest (bottom right) relative photocurrent signals compared to all other wavelengths. The range for the color scale is chosen such, that the values are saturated in the photocurrent image from $\lambda = 473\,\mathrm{nm}$ to avoid obscuring the information in the other four photocurrent images. Nevertheless, the chosen trade-off suffices for the analysis of the main photocurrent features and therefore, for the purpose in this work. The global variation of the photocurrent signal accounts for $\sim \pm 50\,\%$ around the average value for $\lambda = 473\,\mathrm{nm}$. With increasing wavelength, the contrast drops to $\sim \pm 30\,\%$ for $\lambda = 532\,\mathrm{nm}$, then decreases slightly further to $\sim \pm 20\,\%$ for $\lambda = 658\,\mathrm{nm}$, before it rises back to $\sim \pm 30\,\%$ for $\lambda = 735\,\mathrm{nm}$ and $\lambda = 780\,\mathrm{nm}$.

Also in the case of the randomly textured μc-Si:H thin-film solar cell, clear correlations between the local photocurrent response and the topographic features are observed. However, these correlations are more complex than the one observed in the case of the flat μc-Si:H thin-film solar cell investigated in Chapter 4. In order to visualize these correlations more clearly, the topography image, as well as all photocurrent images are depicted in 3D-representations and presented in Fig. 6.3. Figure 6.3 (a) shows the 3D image of the measured topography. For better visibility of the surface texture, the z-axis is scaled by a factor of 1.6 with reference to the x- and y-axis. Figure 6.3 (b) – (c) show the 3D-topography images from (a) color-coded with the photocurrent images recorded with the five wavelengths, respectively.

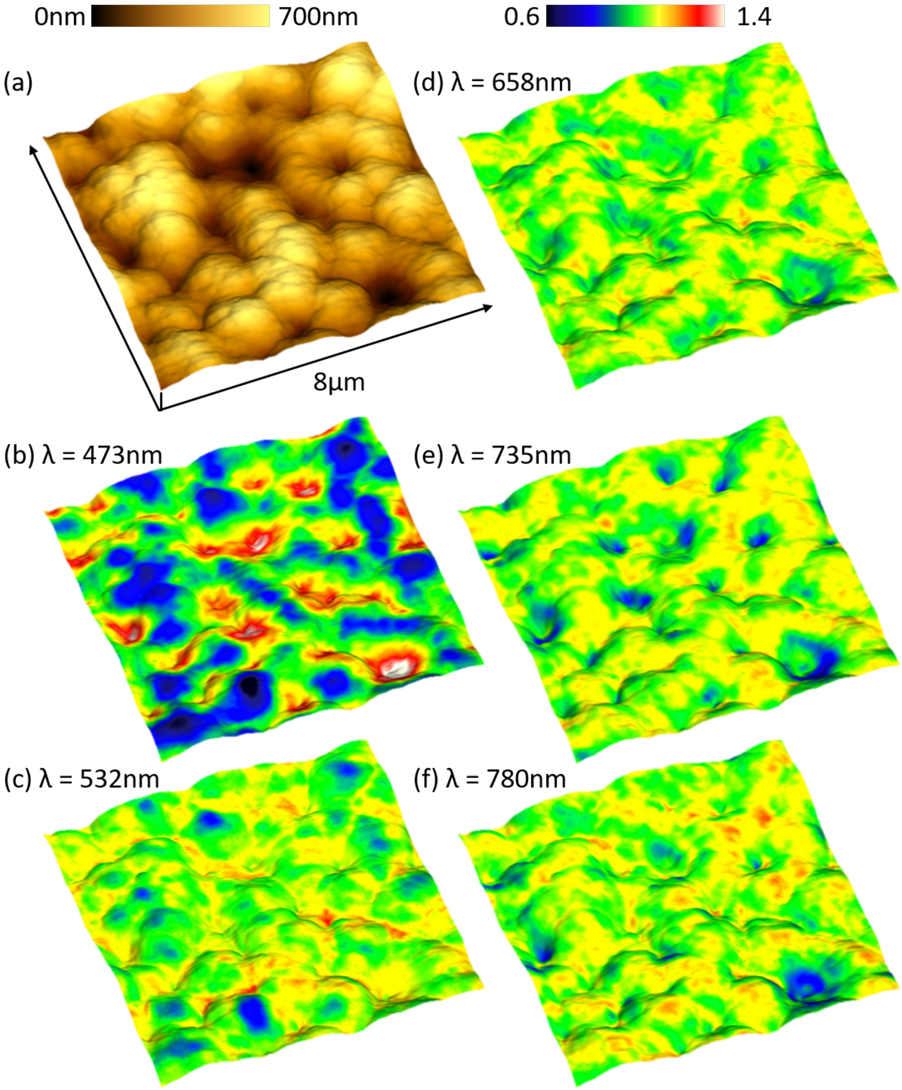

Figure 6.3: (a) 3D SNOM topography image from the area in Figure 6.2 (a). (b)-(f) 3D SNOM topography image from (a) color-coded with the photocurrent signal recorded with $\lambda = 473\,\text{nm}$, $\lambda = 532\,\text{nm}$, $\lambda = 658\,\text{nm}$, $\lambda = 735\,\text{nm}$ and $\lambda = 780\,\text{nm}$, respectively. In all 3D images, the topography is smoothed and the z-axis is scaled by a factor of 1.6 with reference to the x- and y-axis for better clarity. The highest and the lowest values in (b) are saturated due to the chosen color scale to avoid obscuring the information in (c)-(f).

The photocurrent image recorded with $\lambda = 473\,\text{nm}$ shows correlation of the same manner as in the case of the flat μc-Si:H thin-film solar cell: the local photocurrent response is lower at topographic maximums, e.g. on the crater rims or on the ridges. The local photocurrent response is higher at topographic minimums, e.g. in the crater centers or in the grooves between the ridges. However, in the photocurrent image recorded with $\lambda = 532\,\text{nm}$, a strong decrease of this correlation is observed, which is accompanied by the aforementioned reduction of the global contrast from $\sim \pm 50\,\%$ to $\sim \pm 30\,\%$. In the photocurrent image recorded with $\lambda = 658\,\text{nm}$, with a further drop of the global contrast, a reverse of the correlation occurs: the local photocurrent response is now higher at topographic maximums, while being lower at topographic minimums. Finally, at the long wavelengths, i.e. 658 nm, 735 nm and 780 nm, the photocurrent images maintain the same correlation as that of the photocurrent image from $\lambda = 658\,\text{nm}$, while the global contrast increases to $\sim \pm 30\,\%$ again.

The fact that the correlation between the local photocurrent response and the topographic features are converse between short and long wavelengths indicates that there are (at least) two different mechanisms in the photocurrent generation process, which have reversed dependencies on the topographic features. Furthermore, the influence of these mechanisms on the local photocurrent response continuously changes as a function of the incident wavelength. At short wavelengths, one mechanism dominates the photocurrent generation. With increasing wavelength, the other mechanism gradually increases in influence, until it finally prevails in the photocurrent generation process.

In Chapter 4, with the help of FDTD simulations, optical processes, i.e. the local light coupling, was identified as the predominant mechanism in the generation of local photocurrent in case of the flat μc-Si:H thin-film solar cell. Compared to the flat μc-Si:H thin-film solar cell, the randomly textured μc-Si:H thin-film solar cell reveals a much more complex behavior, which involves the interaction of two competing mechanisms. In order to separate the optical from the electrical effects, FDTD simulations are carried out for the randomly textured μc-Si:H thin-film solar cell, as here, only optical effects are taken into account.

6.2 Domain configuration and results of the FDTD simulations

Other than in case of the flat μc-Si:H thin-film solar cell, where an idealized topography was generated for the FDTD simulations, the real topography image has to be used for the randomly textured μc-Si:H thin-film solar cell due to the much more complex surface topography. In order to meet the resolution requirement for the FDTD simulations, the topography image recorded with an atomic force microscope (AFM) is adopted instead of the one recorded with the a-SNOM. Figure 6.4 (a) shows the AFM topography image of the measured area with a size of 10 µm × 10 µm, the area where the SNOM local photocurrent images are recorded is indicated with a white dotted square. Five characteristic probe positions on a well-defined crater are selected for the FDTD simulations. These positions are marked with white circles in the zoom-in image of the crater in Fig. 6.4 (b). In addition, in Fig. 6.4 (c), the crater is depicted in 3D representation, where the five probe positions are more intuitively recognizable. As a guide for the eye, one of the five probe positions is indicated with black arrows in both 2D and 3D images. In Fig. 6.4 (b), from the top to the bottom, the probe positions include:

- A and E: above the tops of two crater rims on the opposite side of the crater.
- B and D: above the flanks of two crater walls on the opposite side of the crater.
- C: in the crater center.

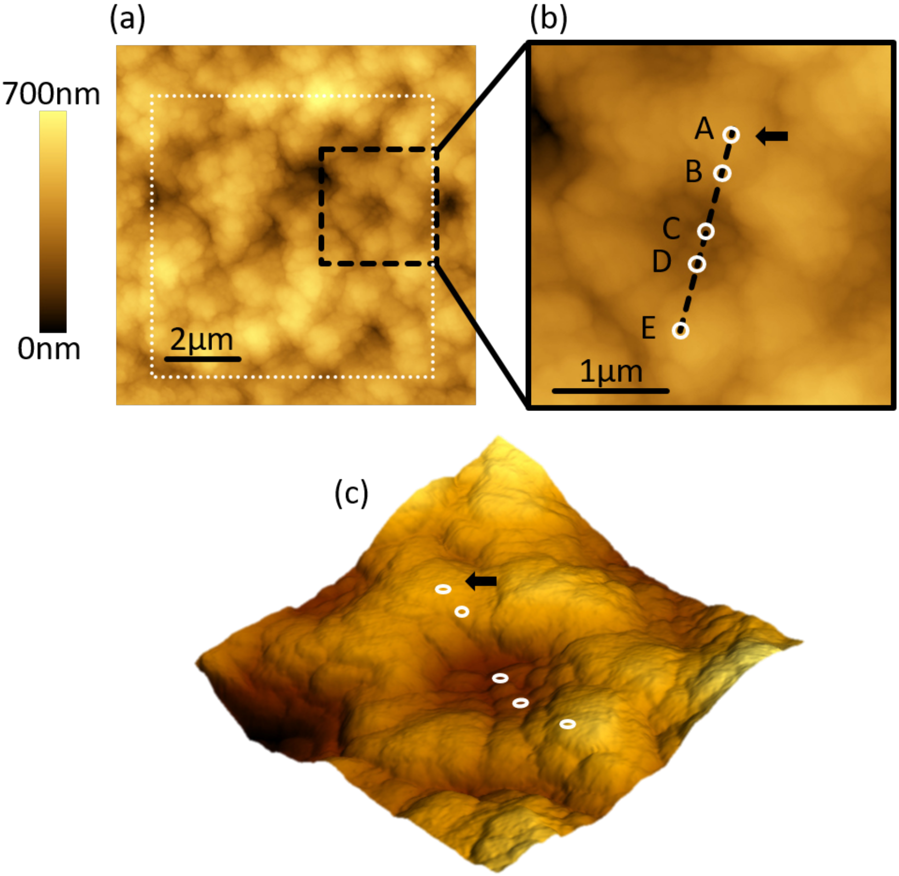

Figure 6.4: (a) AFM topography image with an area of 10 µm × 10 µm, which is used as the topography input for the FDTD simulations. The white dotted square denotes the area, where the SNOM photocurrent images are recorded. (b) Zoom-in image from the black dashed square in (a) with an area of 3.2 µm × 3.2 µm. The probe positions chosen for the FDTD simulations are indicated with white circles. (c) 3D visualization of the topography image in (b), with white circles indicating the chosen probe positions for the FDTD simulations. The z-axis is scaled by a factor of 1.5 with reference to the x- and y-axis for better visual impression. As a guide for the eye, the black arrows in (b) and (c) mark the same position in different illustrations of the topography.

The general configurations of the simulation domains, such as the resolution, the parameters defining the SNOM probe or the layer thicknesses are kept the same as that in the FDTD simulations for the flat μc-Si:H thin-film solar cell. Also, and especially due to the complex surface texture, it is essential that the FDTD simulations are performed with both, the layer-stack configuration and the half-space configuration (More details about the general configurations and descriptions of the two layer-structure configurations are provided in 4.2). However, instead of the flat PEC-substrate or the idealized surface topography in case of the flat μc-Si:H thin-film solar cell, the AFM topography of the randomly textured μc-Si:H thin-film solar cell is applied for each layer in the simulation domains to approximate the conformal layer structure of solar cell. Figure 6.5 shows cut-outs with a size of $6\,\mu\text{m} \times 3\,\mu\text{m}$ from the simulation-domain profiles at $x = 7.23\,\mu\text{m}$ (this is the position where the center of probe is located on the x-axis) for both the layer-stack and the half-space configuration. The individual layers are labeled for the layer-stack configuration. From the bottom to the top, the layer stack consists of a PEC-substrate, a TCO layer with a thickness of 80 nm, an intrinsic μc-Si:H layer with a thickness of $1.34\,\mu\text{m}$ and a top TCO layer with a thickness of 80 nm and the air above the sample.

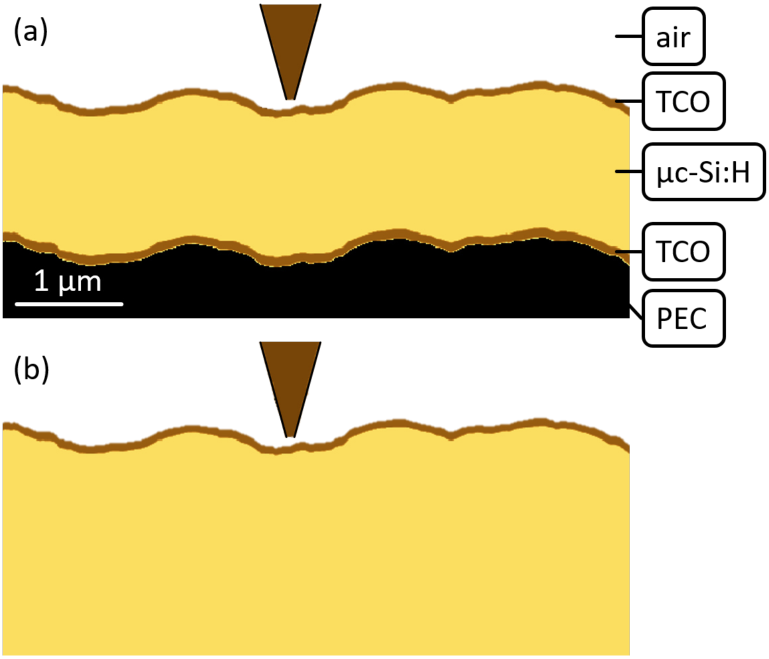

Figure 6.5: Cut-outs from the profiles of the FDTD simulation domains for the randomly textured μc-Si:H thin-film solar cell, created with layer-stack configuration (a) and half-space configuration (b). Both cut-outs have a size of $6\,\mu\text{m} \times 3\,\mu\text{m}$. For each layer in the simulation domains, the AFM-topography is used to account for the conformal growth of the individual layers on the randomly textures substrate. PEC stands for perfect electric conductor.

The point light source inside the SNOM probe is always placed at the same height with reference to the upper boundary of the simulation domain. Consequently, a change of the probe height in the simulation domain would lead to a change of the distance between the light source and the probe aperture. Due to the interference of the light inside the SNOM probe, this change of distance would have an influence on the modes inside the probe and accordingly, the light intensity coupled out of the probe aperture. In case of the flat μc-Si:H thin-film solar cell, this distance variation is insignificant due to the small variations of the surface height. Therefore, in all corresponding FDTD simulations for the flat μc-Si:H thin-film solar cell, the z-size of the simulation domains is kept the same at 5 µm. However, in case of the randomly textured μc-Si:H thin-film solar cell, the height variations of the surface topography are much stronger (up to 240 nm). Therefore, the distance of the light source to the probe aperture varies more significantly than in the case of the flat μc-Si:H thin-film solar cell. In order to compensate this stronger distance variation, the z-size of the simulation domains are individually adapted to the probe height for each probe position.

Figure 6.6 shows the simulation domain profile for the half-space configuration at $x = 7.23$ µm for the probe position C in a gray dotted frame. The complete simulation domain has a dimension of 10 µm × 10 µm × 5 µm. As a comparison, the black dashed lines illustrate the outlines of the simulation domain and of the SNOM probe for the probe position A. Since the SNOM probe is positioned 240 nm higher than at the position C, the z-size of the simulation domain needs to be adjusted to the probe height, so that the complete simulation domain has a size of 10 µm × 10 µm × 5.24 µm.

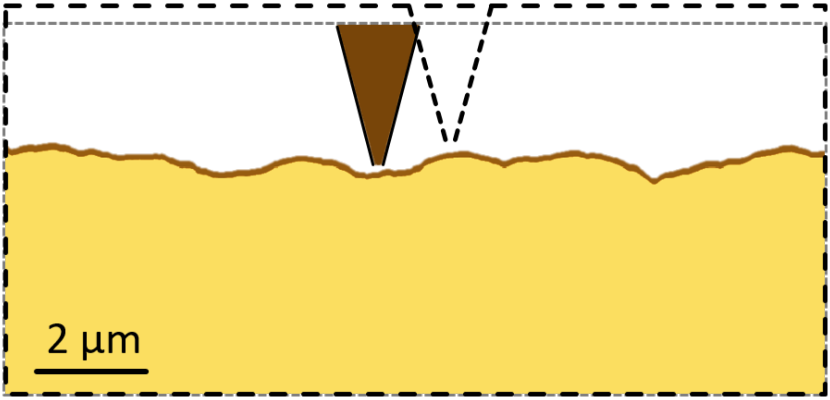

Figure 6.6: FDTD simulation domain profile at $x = 7.23$ µm in half-space configuration for the probe position C. The black dashed lines depict the contour of the simulation domain for the probe position A, where the SNOM probe is placed 240 nm higher.

Due to the large random surface texture, it is assumed that no preferential orientation of the topographic structures exists. Therefore, the polarization effect would be averaged out and does not need to be taken into account. Consequently,

x-polarization is applied throughout all FDTD simulations for the randomly textured μc-Si:H thin-film solar cell. Furthermore, there appears to be a continuous transition of the correlation between the local photocurrent signal and the surface topography within the applied wavelength range, where a reverse of correlation takes place. For this reason, only the shortest wavelength ($\lambda = 473\,\mathrm{nm}$) and the longest wavelength ($\lambda = 780\,\mathrm{nm}$) are considered in the FDTD simulations as two extreme cases. In summary, FDTD simulations are performed for five SNOM probe positions in both, the layer-stack configuration and the half-space configuration, for the wavelengths 473 nm and 780 nm, which amount to a total of 20 simulations. The results will be presented in the next section.

6.3 FDTD Simulation results and comparison with the measurements

Similar to Chapter 4, for the analysis of the FDTD simulation results, the absorbed light intensities I_A and the transmitted light intensities I_T are extracted for the layer-stack configuration and the half-space configuration, respectively. Furthermore, for a better comparability between the simulation results from different wavelengths, FDTD simulations with a flat topography are carried out for each combination of the wavelengths and the simulation-domain configurations. The calculated absorbed intensities I_A and the transmitted intensities I_T corresponding to the individual combination serve as the normalization factor in all diagram plots of the simulation results in this chapter.

Figure 6.7 (a) shows the normalized absorbed intensities I_A as a function of the five probe positions in layer-stack configuration for both wavelengths $\lambda = 473\,\mathrm{nm}$ (blue circles) and $\lambda = 780\,\mathrm{nm}$ (red squares). For a better mapping of the absorbed intensities to the probe positions, i.e. topographic features, the topography profile along the straight line connecting all five probe positions, which is shown in Fig. 6.4 (b), is depicted in the diagram by a black dashed line. For both wavelengths, the maximum I_A is reached when the probe is placed above the crater center at position C, i.e. at the topographic minimum, while weaker I_A is obtained when the probe is placed above the crater rims or above the flanks of the crater walls. Compared to the SNOM photocurrent measurement results of the randomly textured μc-Si:H thin-film solar cell in Fig. 6.2, the correlation between the local photocurrent and the topographic structure is very well reproduced in case of $\lambda = 473\,\mathrm{nm}$. However, in case of $\lambda = 780\,\mathrm{nm}$, the graph does not only show a contrary behavior compared to the measurement results, it also exhibits a significant positive offset of approximately 50 % to that for $\lambda = 473\,\mathrm{nm}$. In the following, firstly the simulation results from the half-space configuration are evaluated in order to identify the optical mechanism behind this offset.

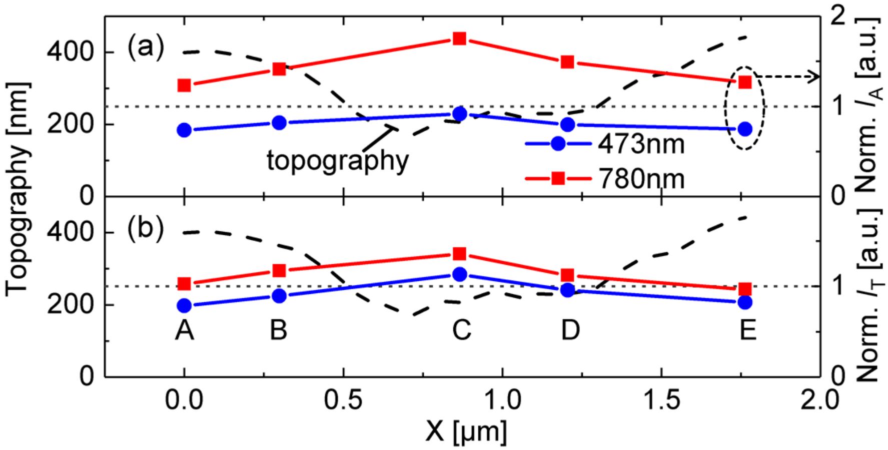

Figure 6.7: (a) Absorbed intensity I_A in the layer-stack configuration and (b) transmitted intensity I_T in the half-space configuration plotted as a function of the SNOM probe position for both wavelengths $\lambda = 473\,\mathrm{nm}$ (blue circles) and $\lambda = 780\,\mathrm{nm}$ (red squares), respectively. The corresponding simulation domains are depicted in Fig. 6.5. In both configurations and for both wavelengths, the results of different probe positions are normalized by the I_A and I_T calculated for a flat topography. The maximum of the respective graph is always found at the topography minimum, i.e. at the crater center. The black dashed lines in both diagrams represent the line scan crossing all five SNOM probe positions through the chosen crater, which is shown in Figure 6.4 (b). The starting position, which corresponds to $X = 0\,\mu\mathrm{m}$ in the diagrams, is indicated with a black arrow in Figure 6.4 (b) and (c), respectively.

Figure 6.7 (b) shows the transmitted intensities I_{T} as a function of the five probe positions in half-space configuration for both wavelengths. As elucidated earlier in Chapter 4, the half-space configuration merely addresses the light coupling efficiency through the local topographic structure into the μc-Si:H half space. The graph for $\lambda = 473\,\mathrm{nm}$ has maintained both, the general trend and the overall contrast from the graph in the layer-stack configuration. Therefore, also for the randomly textured μc-Si:H thin-film solar cell, the local light coupling efficiency can be identified as the dominating mechanism in the photocurrent generation for $\lambda = 473\,\mathrm{nm}$. In case of $\lambda = 780\,\mathrm{nm}$, the offset to the graph of $\lambda = 473\,\mathrm{nm}$ is strongly reduced. As a consequence, the graphs are much more similar to each other regarding both, the general trend and the overall relative contrast. Still, they are not as similar to each other as observed in the FDTD simulations for the flat μc-Si:H thin-film solar cell. The reason could be the much more pronounced surface texture, which would have wavelength-dependent scattering properties. Nonetheless, apparently, the significant offset between the graphs of different configurations in case of $\lambda = 780\,\mathrm{nm}$ cannot be explained by only considering the local light coupling.

As introduced priorly, surface texturing is applied to increase the light path inside the absorber by scattering the light into the absorber at large angles. Accordingly, light trapping only benefits for the long wavelength light, where the light would experience multiple reflections at the interfaces of the absorber due to the long absorption length. In case of $\lambda = 780\,\mathrm{nm}$, the light has an absorption length of $\sim 10\,\mu\mathrm{m}$, which is more than the 7-fold of the μc-Si:H layer thickness. As a consequence, in the layer-stack configuration, the light can be guided and propagate a large distance in all directions, leading to an significant overall increase of the absorbed intensities compared to the half-space configuration, hence to the offset between both configurations.

As has been demonstrated in Chapter 4, with a given topography, optical processes in the photocurrent generation are described very accurately with the FDTD simulations. However, in case of the randomly textured μc-Si:H thin-film solar cell, although for the wavelength 473 nm, the correlation observed in the SNOM photocurrent measurement is reproduced by the FDTD simulations, for the wavelength 780 nm, the measured SNOM photocurrent response shows a complete reversed correlation to the topographic structures compared to the calculated results from the simulations. Hence, it appears obvious that in case of $\lambda = 780\,\text{nm}$, not the optical processes, but the electrical processes become the dominating mechanism in the photocurrent generation, which exhibits a contrary influence on the correlation to the surface topography compared to the optical mechanism. Furthermore, the fact that the electrical mechanism prevails at long wavelengths, i.e. long absorption lengths, indicates that the electrical features are not located near the surface, but buried deeper down in the μc-Si:H absorber. The following section provides a discussion regarding the possible origin of the electrical mechanism and its impact on the photocurrent generation.

6.4 Discussion of the nature of the electrical defects and their impact

From the FDTD simulations for the wavelength 780 nm, it was seen that if the photocurrent generation would mainly be determined by the optical mechanism, then the photocurrent signal would be the strongest at local topographic minimums, i.e. crater center. The fact that the electrical features located further below the surface causes a reverse of the theoretically predicted correlation leads to two conclusions. Firstly, these electrical features show a detrimental effect on the photocurrent generation, therefore, they are most probably electrical defect structures forming local recombination centers, as the grain boundaries in case of the poly-Si LPC thin-film solar cell. Secondly, these electrical defects are primarily located below local topographic minimum, this high dependence on the surface topography indicates that the electrical defects are less likely an inherent property of the μc-Si:H material, but rather formed during the solar-cell fabrication as a consequence of the conformal deposition of the μc-Si:H layers.

A glance at the existing literature provides further evidence, which supports the drawn conclusions. It has been shown in several publications [181–183] that rough surface texture leads to the formation of strip-like defective regions above sharp, V-shaped micro-valleys during the layer deposition. Although the surface texturing of ZnO:Al substrate by wet chemical etching applied in this work is supposed to form more smooth, U-shaped micro-valleys, which are less prone to the formation of the strip-like defects, it can be seen in the SEM-images from several publications that pronounced, V-shaped micro-valleys are still frequently distributed among the surface texture [180, 184, 185].

These strip-like defects were shown to be nano-porous zones with low material density [181, 183, 186], which are formed at the bottom of the micro-valleys, where the silicon growth fronts collide with each other, and develop toward the top surface [182, 183, 187]. These nano-porous regions form local recombination centers to the minority carriers and are in addition prone to in-diffusion of contaminants [181,182], hence deteriorate the local electrical property of the solar cell. Moreover, these strip-like defects tend to decrease in width along the silicon growth direction toward the top surface, some of them even reach full closure near the top surface [182]. Figure 6.8 shows the SEM-image of the cross-section of a textured μc-Si:H thin-film solar cell with V-shaped micro-valleys. The described decrease in width of the strip-like defects are very well visible in this image. This phenomenon also covers with the SNOM photocurrent measurement results of the randomly textured μc-Si:H thin-film solar cell for the wavelength 473 nm, where optical processes still dominate the photocurrent generation, as the generation of the minority carriers only takes place in the first few hundred nm of the μc-Si:H layer and therefore is barely affected by the strip-like defects. This also suggests that the strip-like defects are likely positively charged. As for electron-hole pairs generated near the top surface, the electrons can drift to the p-layer and the holes can drift to the n-layer respectively without combining at the defects, while for electron-hole pairs generated deeper in the absorber, the electrons would have difficulty reaching the p-layer at the top surface due to the recombination at the positively charged defects.

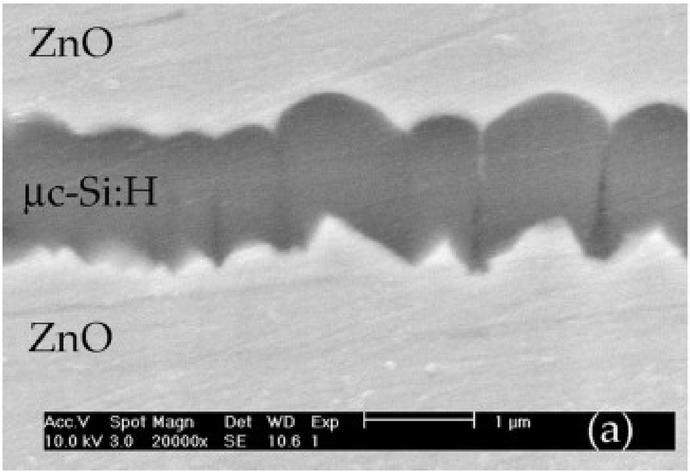

Figure 6.8: SEM-image of the cross-section from a textured μc-Si:H thin-film solar cell. Strip-like defects are observable in each V-shaped micro-valleys, which develop from the bottom of the valleys toward the top surface while decreasing in width. Reprinted from [181], Copyright (2009), with permission from Elsevier.

Although a more detailed study of these electrical defects in the investigated textured μc-Si:H thin-film solar cell would go beyond the scope of this work due to the further required amount of experiments and simulations, a rough estimation of the impact of the electrical defects on the photocurrent generation can be given based on the existing SNOM photocurrent measurements and the FDTD simulation results. On the one hand, from the graph in Fig. 6.7 (a), a global (maximum) relative contrast of $\sim 40\,\%$ with the minimum as the reference can be extracted, if there was no electrical defects and the optical mechanism would dominate the photocurrent generation. On the other hand, from the SNOM photocurrent image for $\lambda = 780\,\mathrm{nm}$ in Fig. 6.2 (f), the local contrast (with respect to the considered crater) with the reversed correlation accounts for $\sim 30\,\%$ with the photocurrent at the crater center as the reference. With the simplified assumption that the photocurrent generation on the crater rims does not suffer from the electrical defects at the crater center, these contrast values imply a loss factor of $(1+40\,\%)/(1-30\,\%) = 2$ for the local photocurrent generated at the crater center. Therefore, these electrical defects exhibit a detrimental effect on the local photocurrent generation, hence the solar cell efficiency. Consequently, their elimination would contribute to the improvement of the solar cell efficiency and is subject of ongoing researches [188–190].

6.5 Conclusion

Equipped with the knowledge acquired from the independent studies of the optical mechanism and the electrical mechanism in the photocurrent generation, this chapter provided a demonstrative example of how the SNOM photocurrent measurement results of a more complex sample can be understood and interpreted. The sample applied for the demonstration is a randomly textured μc-Si:H thin-film solar cell where both, the optical mechanism and the electrical mechanism have a significant impact on the photocurrent generation. SNOM photocurrent measurements were conducted with five different wavelengths: 473 nm, 532 nm, 658 nm, 735 nm and 780 nm. Contrary to the measurement results from the flat μc-Si:H thin-film solar cell, where the optical mechanism dominates for all wavelengths and the same correlation between the local photocurrent response and the local topographic structures were observed, this correlation undergoes a continuous change and becomes reversed from the short wavelengths to the long wavelengths in case of the randomly textured μc-Si:H thin-film solar cell. Supporting FDTD simulations with the real AFM topography predict however the same correlation for all wavelengths, i.e. high photocurrent response at topographic minimums and low photocurrent response at topographic maximums. Therefore, the reversed correlation observed at long wavelengths must originate from electrical defects located below topographic minimums, e.g. crater centers. Research in the existing literature suggests that these electrical defects are most likely strip-like nano-porous zones, which typically grow from the bottom of sharp micro-valleys toward the top surface and form recombination centers for minority carriers. A simple estimation based on the SNOM photocurrent measurement results and the FDTD simulation results shows that these electrical defects can lead to a reduction of the local photocurrent by 50%. Consequently, the suppression of these electrical defects induced by sharp surface texture constitutes an important aspect for the improvement of the solar cell performance.

7 Summary and Outlook

7.1 Summary

The performance of a solar cell is determined, to a large extent, by the local optoelectronic properties on the microscopic or even nanoscopic length scales. Therefore, local photocurrent measurement of solar cells using the probe aperture of an a-SNOM as the illumination source constitutes a highly attractive method for the nanoscale optoelectronic characterization of solar cells. The measured local photocurrent signal contains valuable information about the effects of the local optoelectronic properties on the generation of the photocurrent. The goal of this work was to understand and distinguish the specific effects of the local topography and the local material inhomogeneity on the resulting photocurrent signal by the separate analyses of the optical processes and the electrical processes in the solar cell. In the scope of this work, several solar cell samples were investigated by SNOM photocurrent measurements with various light wavelengths. In combination with theoretical simulations, the individual impact of topographic features and the local material inhomogeneity, specifically the grain boundaries, on the photocurrent signal was successfully identified and demonstrated.

The first investigated solar cell was a μc-Si:H thin-film solar cell which was deposited on a flat substrate in n-i-p structure. In spite of the flat substrate, the solar cell exhibits surface protrusions with sizes ranging from several ten nanometers to several hundered nanometers. SNOM photocurrent measurements with five different wavelengths varying from 473 nm to 780 nm have collectively shown the same and clear correlation between the photocurrent signal and the local topography variation: photocurrent is lower at local topographical maximum, e.g. on top of a protrusion, and higher at local topographic minimum, e.g. in the grooves surrounding the protrusion. By comparison of the measurement results to the FDTD simulation results, which were performed with idealized topography containing both topographic extremes, the local light coupling was identified and confirmed as the dominating mechanism in the photocurrent generation for the μc-Si:H thin-film solar cell. Furthermore, on the applied topographic features, the FDTD simulation results predicted that the light coupling efficiency at local topographical minimum can be up to $\sim 30\%$ higher than that at local topographical maximum, which is in good agreement with the observations from the measurement results. A curvature analysis of the topographic features of the μc-Si:H thin-film solar cell suggests that the correlation between the local light coupling efficiency and the local topography is likely to originate from the variation of the surface area interacting with the optical near-field. In addition, both SNOM photocurrent measurements were conducted and compared to the FDTD simulations to investigate the effect of light polarizations on the local light coupling efficiency. The measurements were carried out with a periodically textured a-Si:H thin-film solar cell where the surface structures are arranged in a square grating. Both, the measurements and the simulations have shown that, at locations with a high rotational asymmetry, e.g. in the groove between two neighboring structures, the local light coupling efficiency can significantly change ($> 30\%$) between two perpendicular polarizations.

After the effect of the surface topography variations on the photocurrent signal was analyzed, the impact of the local material inhomogeneity on the photocurrent response was studied with a polycrystalline silicon thin-film solar cell fabricated by liquid phase crystallization on a flat glass substrate. The applied poly-Si LPC solar cell exhibits a nominally flat surface with barely any topographic structure. Furthermore, large grains are formed during the crystallization process and the associated grain boundaries are typically rich of electrical defects. SNOM photocurrent measurements were conducted on an area with a grain boundary for the wavelengths 473 nm, 658 nm and 780 nm. The measured photocurrent maps show a clear decrease of the photocurrent signal with decreasing distance to the grain boundary for all three wavelengths. Line profiles crossing the grain boundary were extracted from the photocurrent map. The fitting of the photocurrent profiles with electrical simulations based on the minority carrier diffusion equation allows for the derivation of two characteristic material parameters: the minority carrier diffusion length

L_D and the grain boundary recombination velocity S_gb. FDTD simulations, which were performed with an identical layer configuration as that of the real LPC solar cell, delivered the required optical generation profiles for all three wavelengths as the input parameters for the electrical calculations. As a result, $L_\mathrm{D} = 4.6\,\mu\mathrm{m}$ and $S_\mathrm{gb} = 5.2 \times 10^5\,\mathrm{cm/s}$ were obtained for the characterized area and grain boundary of the poly-Si LPC solar cell. These values are in good agreement with those found in other references.

The knowledge of the effects of both, the local topography and the local material homogeneity on the photocurrent generation gained form the previous studies enables the analysis of more complex samples. This was demonstrated for a randomly textured μc-Si:H thin-film solar cell which possesses both, distinct surface textures and electrical defects inside the absorber, hence both optical mechanism and electrical mechanism have significant contribution to the resulting photocurrent response. SNOM photocurrent measurements with five different wavelengths ranging from 473 nm to 780 nm were performed. Unlike the measurement results of the flat μc-Si:H thin-film solar cell, where the local light coupling efficiency dominates and the same correlation between the photocurrent signal and the local topography is observed for all applied wavelengths, the photocurrent response gradually changed with varying wavelengths in case of the randomly textured μc-Si:H thin-film solar cell. While for short wavelengths, the correlation between the photocurrent signal and the local topography was the same as the one for the flat μc-Si:H thin-film solar cell, this correlation becomes less pronounced with increasing wavelengths and finally reversed at long wavelengths: high photocurrent signal is now found at topographic maximums and low photocurrent signal at topographic minimums. However, FDTD simulations performed with the real AFM topography yielded the same correlation for all wavelengths as in the case of the flat μc-Si:H thin-film solar cell. Therefore, the drop of the photocurrent at topographic minimums must be the result of electrical defects at some distance below the surface. According to the existing literature, these electrical defects probably consist of strip-like nano-porous zones, which commonly arise at sharp micro-valleys and grow from the bottom toward the surface. These nano-porous zones are typical recombination centers for minority carriers. By comparing the reversed contrast in the SNOM photocurrent measurements to the predicted contrast in the FDTD simulations, the detrimental effect of the electrical defects is roughly estimated, which can lead to a reduction of the local photocurrent by $\sim 50\%$.

7.2 Outlook

Measurement with external voltage FDTD simulation has been proven to be a powerful tool to support the analysis of the SNOM photocurrent measurements, as it allows for the identification, hence the separation of optical effects from the electrical effects in the measured photocurrent signal. The ability to study these two aspects separately provides valuable insights into the individual influence of the topographic features and the local material inhomogeneity on the photocurrent generation, hence allows them to be addressed specifically when it comes to the improvement of the solar cell performance. On the other side, FDTD simulations are rather time- and resource-consuming. If the investigated optoelectronic sample has a complicated structure, for which neither a simplification with an idealized topography is possible, nor a limited number of characteristic probe positions is sufficient, then the FDTD simulations might not be the most efficient way. The application of a reverse-biased voltage during the SNOM photocurrent measurements provides another possibility for the separate examination of optical and electrical effects. Under reverse bias, the built-in electric field of the solar cell increases and facilitates a better extraction, hence a better collection of the charge carriers, which would have recombined at electrical defects. In other words, the application of reverse-biased voltages could minimize the effects of electrical defects in the SNOM photocurrent measurements, so that the obtained photocurrent signal mainly reflects the influence of optical processes. In the example of the randomly textured μc-Si:H thin-film solar cell, it is expected that the photocurrent signal would show the same correlation to the local topography for all applied wavelengths. The extension of the existing SNOM phocurrent measurement setup by the possibility of applying an electrical voltage enables another important control parameter in the measurement and therefore, holds promise for more informative and easier interpretation of the SNOM photocurrent measurement results.

Measurement of novel photovoltaic materials In the research and continuous development of novel solar cell materials, SNOM photocurrent measurements can provide deep insights into the microscopic and nanoscopic optoelectronic properties of the investigated solar cells. A promising candidate are thin-film solar cells which use hybrid organic-inorganic perovskites such as methylammonium lead halides ($CH_3NH_3Pb(I,Cl,Br)_3$) as the active layer [191–193]. As a solution-processed solar cell, it exhibits both large absorption coefficients and high open-circuit voltages despite the rather simple fabrication technique [194]. The tunability of the bandgap over the entire visible spectral range ($\sim 390\,\mathrm{nm} - 780\,\mathrm{nm}$) by variation of the chemical compositions is another remarkable advantage for the use as active layer in a solar cell [195,196]. The intense research of the perovskite solar cells has boosted the efficiency from 3.8% [197] to more than 21% [73] in a short period of time. The perovskite solar cells generally exhibit material heterogeneity, such as surface morphology, grain formation and local variation of chemical concentrations on length scales from tens of nanometers to a few micrometers [198–202], which are the optimal sizes for the characterization with SNOM photocurrent measurements. Therefore, the investigation of perovskite solar cells with the SNOM photocurrent measurements is highly promising and would certainly add a valuable chapter to the ongoing intense research activities.

References

[1] E. Synge, “A suggested method for extending microscopic resolution into the ultra-microscopic region,” *The London, Edinburgh, and Dublin Philosophical Magazine and Journal of Science*, vol. 6, no. 35, pp. 356–362, 1928.

[2] D. W. Pohl, W. Denk, and M. Lanz, “Optical stethoscopy: Image recording with resolution $\lambda/20$,” *Applied Physics Letters*, vol. 44, no. 7, pp. 651–653, 1984.

[3] A. Lewis, M. Isaacson, A. Harootunian, and A. Muray, “Development of a 500 Å spatial resolution light microscope: I. light is efficiently transmitted through $\lambda/16$ diameter apertures,” *Ultramicroscopy*, vol. 13, no. 3, pp. 227 – 231, 1984.

[4] U. C. Fischer, “Optical characteristics of 0.1 μm circular apertures in a metal film as light sources for scanning ultramicroscopy,” *Journal of Vacuum Science & Technology B: Microelectronics Processing and Phenomena*, vol. 3, no. 1, pp. 386–390, 1985.

[5] P. Dawson, F. de Fornel, and J.-P. Goudonnet, “Imaging of surface plasmon propagation and edge interaction using a photon scanning tunneling microscope,” *Phys. Rev. Lett.*, vol. 72, pp. 2927–2930, May 1994.

[6] K. Imura, T. Nagahara, and H. Okamoto, “Plasmon mode imaging of single gold nanorods,” *J. Am. Chem. Soc.*, vol. 126, pp. 12730–12731, 2004.

[7] H. Ditlbacher, A. Hohenau, D. Wagner, U. Kreibig, M. Rogers, F. Hofer, F. R. Aussenegg, and J. R. Krenn, “Silver nanowires as surface plasmon resonators,” *Phys. Rev. Lett.*, vol. 95, p. 257403, Dec 2005.

[8] J.-S. Bouillard, S. Vilain, W. Dickson, and A. V. Zayats, “Hyperspectral imaging with scanning near-field optical microscopy: applications in plasmonics,” *Opt. Express*, vol. 18, pp. 16513–16519, Aug 2010.

[9] A. G. Choo, H. E. Jackson, U. Thiel, G. N. De Brabander, and J. T. Boyd, "Near field measurements of optical channel waveguides and directional couplers," *Applied Physics Letters*, vol. 65, no. 8, pp. 947–949, 1994.

[10] M. L. M. Balistreri, H. Gersen, J. P. Korterik, L. Kuipers, and N. F. van Hulst, "Tracking femtosecond laser pulses in space and time," *Science*, vol. 294, no. 5544, pp. 1080–1082, 2001.

[11] U. W. Paetzold, S. Lehnen, K. Bittkau, U. Rau, and R. Carius, "Nanoscale observation of waveguide modes enhancing the efficiency of solar cells," *Nano Letters*, vol. 14, no. 11, pp. 6599–6605, 2014.

[12] E. Betzig and R. J. Chichester, "Single molecules observed by near-field scanning optical microscopy.," *Science*, vol. 262, no. 5138, pp. 1422–1425, 1993.

[13] J. K. Trautman, J. J. Macklin, L. E. Brus, and E. Betzig, "Near-field spectroscopy of single molecules at room temperature," *Nature*, vol. 369, no. 6475, pp. 40–42, 1994.

[14] X. S. Xie and J. K. Trautman, "Optical studies of single molecules at room temperature," *Annual Review of Physical Chemistry*, vol. 49, no. 1, pp. 441–480, 1998. PMID: 15012434.

[15] J. Hwang, L. K. Tamm, C. Böhm, T. S. Ramalingam, E. Betzig, and M. Edidin, "Nanoscale complexity of phospholipid monolayers investigated by near-field scanning optical microscopy," *Science*, vol. 270, no. 5236, pp. 610–614, 1995.

[16] J. DeAro, K. Weston, S. Buratto, and U. Lemmer, "Mesoscale optical properties of conjugated polymers probed by near-field scanning optical microscopy," *Chemical Physics Letters*, vol. 277, no. 5, pp. 532 – 538, 1997.

[17] T. Huser, T. Lacoste, H. Heinzelmann, and H.-S. Kitzerow, "Scanning near-field optical microscopy of cholesteric liquid crystals," *The Journal of Chemical Physics*, vol. 108, no. 18, pp. 7876–7880, 1998.

[18] P. F. Barbara, D. M. Adams, and D. B. O'Connor, "Characterization of Organic Thin Film Materials With Near-Field Scanning Optical Microscopy (NSOM)," *Annual Review of Materials Science*, vol. 29, no. 1, pp. 433–469, 1999.

[19] T. Taubner, R. Hillenbrand, and F. Keilmann, "Performance of visible and mid-infrared scattering-type near-field optical microscopes," *Journal of Microscopy*, vol. 210, no. 3, pp. 311–314, 2003.

[20] R. Hillenbrand, "Towards phonon photonics: scattering-type near-field optical microscopy reveals phonon-enhanced near-field interaction," *Ultramicroscopy*, vol. 100, no. 3, pp. 421 – 427, 2004. Proceedings of the Fifth International Conference on Scanning Probe Micrscopy, Sensors and Nanostructures.

[21] Y. Gu, E. S. Kwak, J. L. Lensch, J. E. Allen, T. W. Odom, and L. J. Lauhon, "Near-field scanning photocurrent microscopy of a nanowire photodetector," *Applied Physics Letters*, vol. 87, no. 4, p. 043111, 2005.

[22] Y. Gu, J. P. Romankiewicz, J. K. David, J. L. Lensch, L. J. Lauhon, E.-S. Kwak, and T. W. Odom, "Local photocurrent mapping as a probe of contact effects and charge carrier transport in semiconductor nanowire devices," *Journal of Vacuum Science & Technology B: Microelectronics and Nanometer Structures Processing, Measurement, and Phenomena*, vol. 24, no. 4, pp. 2172–2177, 2006.

[23] Y. T. Chen, K. F. Karlsson, J. Birch, and P. O. Holtz, "Determination of critical diameters for intrinsic carrier diffusion-length of GaN nanorods with cryo-scanning near-field optical microscopy," *Scientific Reports*, vol. 6, no. October 2015, p. 21482, 2016.

[24] S. K. Buratto, J. W. P. Hsu, E. Betzig, J. K. Trautman, R. B. Bylsma, C. C. Bahr, and M. J. Cardillo, "Near-field photoconductivity: Application to carrier transport in ingaasp quantum well lasers," *Applied Physics Letters*, vol. 65, no. 21, pp. 2654–2656, 1994.

[25] M. S. Ünlü, B. B. Goldberg, W. D. Herzog, D. Sun, and E. Towe, "Near-field optical beam induced current measurements on heterostructures," *Applied Physics Letters*, vol. 67, no. 13, p. 1862, 1995.

[26] T. Mueller, F. Xia, M. Freitag, J. Tsang, and P. Avouris, "Role of contacts in graphene transistors: A scanning photocurrent study," *Physical Review B - Condensed Matter and Materials Physics*, vol. 79, no. 24, pp. 1–6, 2009.

[27] S. Grover, S. Dubey, J. P. Mathew, and M. M. Deshmukh, "Limits on the

bolometric response of graphene due to flicker noise," *Applied Physics Letters*, vol. 106, no. 5, p. 051113, 2015.

[28] M. K. Herndon, a. Gupta, V. Kaydanov, and R. T. Collins, "Evidence for grain-boundary-assisted diffusion of sulfur in polycrystalline CdS/CdTe heterojunctions," *Applied Physics Letters*, vol. 75, no. 22, p. 3503, 1999.

[29] M. K. Herndon, W. C. Bradford, and R. T. Collins, "Near-field scanning optical microscopy cross-sectional measurements of crystalline GaAs solar cells," *Applied Physics Letters*, vol. 77, no. 1, pp. 100–102, 2000.

[30] S. Smith, P. Zhang, T. Gessert, and a. Mascarenhas, "Near-field optical beam-induced currents in CdTe/CdS solar cells: Direct measurement of enhanced photoresponse at grain boundaries," *Applied Physics Letters*, vol. 85, no. 17, pp. 3854–3856, 2004.

[31] C. R. McNeill, Frohne, H., Holdsworth, J. L., Furst, J. E., King, B. V., Dastoor, and P. C., "Direct Photocurrent Mapping of Organic Solar Cells Using a Near-Field Scanning Optical Microscope.," *Nano Letters*, vol. 4, no. 2, pp. 219–223, 2004.

[32] C. R. McNeill, H. Frohne, J. L. Holdsworth, and P. C. Dastoor, "Near-Field Scanning Photocurrent Measurements of Polyfluorene Blend Devices: Directly Correlating Morphology with Current Generation," *Nano Letters*, vol. 4, no. 12, pp. 2503–2507, 2004.

[33] R. Riehn, R. Stevenson, D. Richards, D.-J. Kang, M. Blamire, A. Downes, and F. Cacialli, "Local Probing of Photocurrent and Photoluminescence in a Phase-Separated Conjugated-Polymer Blend by Means of Near-Field Excitation," *Advanced Functional Materials*, vol. 16, no. 4, pp. 469–476, 2006.

[34] S. Mukhopadhyay, A. J. Das, and K. S. Narayan, "High-Resolution Photocurrent Imaging of Bulk Heterojunction Solar Cells.," *The Journal of Physical Chemistry Letters*, vol. 4, no. 1, pp. 161–9, 2013.

[35] M. S. Leite, M. Abashin, H. J. Lezec, A. Gianfrancesco, A. A. Talin, and N. B. Zhitenev, "Nanoscale Imaging of Photocurrent and Efficiency in CdTe Solar Cells.," *ACS Nano*, vol. 8, no. 11, pp. 11883–90, 2014.

[36] E. M. Tennyson, J. A. Frantz, J. D. Myers, J. S. Sanghera, R. Y. Bekele, Suok-

Min Na, and M. S. Leite, “Imaging eqe in cigs solar cells with high spatial resolution,” in *2015 IEEE 42nd Photovoltaic Specialist Conference (PVSC)*, pp. 1–4, 2015.

[37] W. Rouis, M. Haggui, S. Rekaya, L. Sfaxi, R. M’ghaieth, H. Maaref, and P. Fumagalli, “Local photocurrent mapping of InAs/InGaAs/GaAs intermediate-band solar cells using scanning near-field optical microscopy,” *Solar Energy Materials and Solar Cells*, vol. 144, pp. 324–330, 2016.

[38] M. Haggui, B. Reinhold, P. Andrae, D. Greiner, M. Schmid, and P. Fumagalli, “Local photocurrent mapping and cell performance behaviour on a nanometre scale for monolithically interconnected Cu(In,Ga)Se2 solar cells,” *Journal of Microscopy*, vol. 268, no. 1, pp. 66–72, 2017.

[39] J. D. Jackson, *Classical electrodynamics.* New York: Wiley, 3rd ed., 1999.

[40] M. Fox, *Optical properties of solids.* Oxford master series in physics, Oxford: Univ. Press, 2nd ed., 2010.

[41] S. A. Maier, *Plasmonics : fundamentals and applications.* Berlin: Springer, 2007.

[42] M. Born and E. Wolf, *Principles of optics: electromagnetic theory of propagation, interference and diffraction of light.* Oxford: Pergamon Pr., 6th ed., 1986.

[43] E. Hecht, *Optik.* De Gruyter Studium, Berlin: De Gruyter, 2018.

[44] L. Novotny and B. Hecht, *Principles of Nano-Optics.* Cambridge University Press, 2 ed., 2012.

[45] E. Wolf and M. Nieto-Vesperinas, “Analyticity of the angular spectrum amplitude of scattered field and some of its consequences,” *J. Opt. Soc. Am. A*, vol. 2, pp. 886–890, 06 1985.

[46] F. M. Grimaldi, *Physico-mathesis de lumine, coloribus et iride.* Bologna, 1665.

[47] L. Bergmann and C. Schaefer, *Optik.* Berlin: De Gruyter, 2018.

[48] S. Lehnen, *Investigation of light propagation in thin-film silicon solar cells by dual-probe scanning near-field optical microscopy.* Ph.D. thesis, RWTH Aachen University, 2015.

[49] Lord Rayleigh, "Investigations in optics, with special reference to the spectroscope," *Philosophical Magazine (5)*, vol. 8, no. 49, pp. 261–274, 1879.

[50] Lord Rayleigh, "On the theory of optical images, with special reference to the microscope," *Philosophical Magazine (5)*, vol. 42, no. 255, pp. 167–195, 1896.

[51] E. Abbe, "Beiträge zur Theorie des Mikroskops und der mikroskopischen Wahrnehmung," *Archiv für Mikroskopische Anatomie*, vol. 9, pp. 413–468, Dec 1873.

[52] J. W. Goodman, *Introduction to Fourier optics.* MacGraw-Hill physical and quantum electronics series, San-Francisco: MacGraw Hill, 1968.

[53] J. M. Vigoureux and D. Courjon, "Detection of nonradiative fields in light of the Heisenberg uncertainty principle and the Rayleigh criterion," *Appl. Opt.*, vol. 31, pp. 3170–3177, Jun 1992.

[54] C. Girard and A. Dereux, "Near-field optics theories," *Reports on Progress in Physics*, vol. 59, no. 5, pp. 657–699, 1996.

[55] L. Novotny, "The History of Near-field Optics," *Progress in Optics*, vol. 50, pp. 137–184, 2008.

[56] H. A. Bethe, "Theory of diffraction by small holes," *Phys. Rev.*, vol. 66, pp. 163–182, Oct 1944.

[57] C. Bouwkamp, "On Bethe's theory of diffraction by small holes," *Philips Research Reports*, vol. 5, pp. 321–332, 1950.

[58] C. Genet and T. W. Ebbesen, "Light in tiny holes," *Nature*, vol. 445, pp. 39–46, 2007.

[59] Y. Leviatan, "Study of near-zone fields of a small aperture," *Journal of Applied Physics*, vol. 60, no. 5, pp. 1577–1583, 1986.

[60] A. Roberts, "Electromagnetic theory of diffraction by a circular aperture in a thick, perfectly conducting screen," *J. Opt. Soc. Am. A*, vol. 4, pp. 1970–1983, Oct 1987.

[61] C. Obermüller and K. Karrai, "Far field characterization of diffracting circular apertures," *Applied Physics Letters*, vol. 67, no. 23, pp. 3408–3410, 1995.

[62] R. Gordon and A. G. Brolo, "Increased cut-off wavelength for a subwavelength

hole in a real metal," *Opt. Express*, vol. 13, pp. 1933–1938, Mar 2005.

[63] B. Hecht, B. Sick, U. P. Wild, V. Deckert, R. Zenobi, O. J. F. Martin, and D. W. Pohl, "Scanning near-field optical microscopy with aperture probes: Fundamentals and applications," *J. Chem. Phys.*, vol. 112, pp. 7761–7774, May 2000.

[64] J. Nelson, *The physics of solar cells.* London: Imperial College Press, 2003.

[65] N. W. Ashcroft and N. D. Mermin, *Solid state physics.* Fort Worth: Harcourt College Publ., 2000.

[66] H. Ibach and H. Lüth, *Solid state physics : an introduction to prinicples of materials science.* Berlin: Springer, 3rd ed., 2003.

[67] C. Kittel, *Introduction to solid state physics.* New York: Wiley, 8th ed., 2005.

[68] A. Polman, M. Knight, E. C. Garnett, B. Ehrler, and W. C. Sinke, "Photovoltaic materials: Present efficiencies and future challenges," *Science*, vol. 352, no. 6283, pp. 307–317, 2016.

[69] C. Battaglia, A. Cuevas, and S. De Wolf, "High-efficiency crystalline silicon solar cells: status and perspectives," *Energy Environ. Sci.*, vol. 9, pp. 1552–1576, 2016.

[70] D. M. Chapin, C. S. Fuller, and G. L. Pearson, "A new silicon p-n junction photocell for converting solar radiation into electrical power," *Journal of Applied Physics*, vol. 25, no. 5, pp. 676–677, 1954.

[71] M. A. Green, "Photovoltaics: coming of age," in *IEEE Conference on Photovoltaic Specialists*, pp. 1–8, 1990.

[72] K. Yoshikawa, H. Kawasaki, W. Yoshida, T. Irie, K. Konishi, K. Nakano, T. Uto, D. Adachi, M. Kanematsu, H. Uzu, and K. Yamamoto, "Silicon heterojunction solar cell with interdigitated back contacts for a photoconversion efficiency over 26%," *Nature Energy*, vol. 2, no. 5, 2017.

[73] M. A. Green, E. D. Dunlop, J. Hohl-Ebinger, M. Yoshita, N. Kopidakis, and A. W. Ho-Baillie, "Solar cell efficiency tables (version 55)," *Progress in Photovoltaics: Research and Applications*, vol. 28, no. 1, pp. 3–15, 2020.

[74] A. Jäger-Waldau, "PV Status Report 2018," European Union, 2008.

[75] J. Meier, J. Spitznagel, U. Kroll, C. Bucher, S. Faÿ, T. Moriarty, and A. Shah, "Potential of amorphous and microcrystalline silicon solar cells," *Thin Solid Films*, vol. 451-452, pp. 518 – 524, 2004. Proceedings of Symposium D on Thin Film and Nano-Structured Materials for Photovoltaics, of the E-MRS 2003 Spring Conference.

[76] P. Würfel, *Physics of solar cells : from basic principles to advanded concepts.* Weinheim: Wiley-VCH, 2nd ed., 2009.

[77] O. Vetterl, F. Finger, R. Carius, P. Hapke, L. Houben, O. Kluth, A. Lambertz, A. Mück, B. Rech, and H. Wagner, "Intrinsic microcrystalline silicon: A new material for photovoltaics," *Solar Energy Materials and Solar Cells*, vol. 62, no. 1, pp. 97–108, 2000.

[78] H. Dersch, J. Stuke, and J. Beichler, "Light-induced dangling bonds in hydrogenated amorphous silicon," *Applied Physics Letters*, vol. 38, no. 6, pp. 456–458, 1981.

[79] D. K. Biegelsen and M. Stutzmann, "Hyperfine studies of dangling bonds in amorphous silicon," *Phys. Rev. B*, vol. 33, pp. 3006–3011, Mar 1986.

[80] F. Finger, P. Hapke, M. Luysberg, R. Carius, H. Wagner, and M. Scheib, "Improvement of grain size and deposition rate of microcrystalline silicon by use of very high frequency glow discharge," *Applied Physics Letters*, vol. 65, no. 20, pp. 2588–2590, 1994.

[81] M. Luysberg, P. Hapke, R. Carius, and F. Finger, "Structure and growth of hydrogenated microcrystalline silicon: Investigation by transmission electron microscopy and raman spectroscopy of films grown at different plasma excitation frequencies," *Philosophical Magazine A*, vol. 75, no. 1, pp. 31–47, 1997.

[82] W. Shockley and H. J. Queisser, "Detailed balance limit of efficiency of p-n junction solar cells," *Journal of Applied Physics*, vol. 32, no. 3, pp. 510–519, 1961.

[83] W. Shockley and W. T. Read, "Statistics of the recombinations of holes and electrons," *Phys. Rev.*, vol. 87, pp. 835–842, Sep 1952.

[84] R. N. Hall, "Electron-hole recombination in germanium," *Phys. Rev.*, vol. 87, pp. 387–387, Jul 1952.

[85] T. Su, P. C. Taylor, G. Ganguly, and D. E. Carlson, “Direct role of hydrogen in the staebler-wronski effect in hydrogenated amorphous silicon,” *Phys. Rev. Lett.*, vol. 89, p. 015502, Jun 2002.

[86] E. Vazsonyi, K. D. Clercq, R. Einhaus, E. V. Kerschaver, K. Said, J. Poortmans, J. Szlufcik, and J. Nijs, “Improved anisotropic etching process for industrial texturing of silicon solar cells,” *Solar Energy Materials and Solar Cells*, vol. 57, no. 2, pp. 179 – 188, 1999.

[87] P. Campbell and M. A. Green, “High performance light trapping textures for monocrystalline silicon solar cells,” *Solar Energy Materials and Solar Cells*, vol. 65, no. 1, pp. 369–375, 2001.

[88] C. Battaglia, C.-M. Hsu, K. Söderström, J. Escarré, F.-J. Haug, M. Charriýre, M. Boccard, M. Despeisse, D. T. L. Alexander, M. Cantoni, Y. Cui, and C. Ballif, “Light trapping in solar cells: Can periodic beat random?,” *ACS Nano*, vol. 6, no. 3, pp. 2790–2797, 2012. PMID: 22375932.

[89] U. W. Paetzold, E. Moulin, D. Michaelis, W. Böttler, C. Wächter, V. Hagemann, M. Meier, R. Carius, and U. Rau, “Plasmonic reflection grating back contacts for microcrystalline silicon solar cells,” *Applied Physics Letters*, vol. 99, no. 18, p. 181105, 2011.

[90] H. Sai, K. Saito, and M. Kondo, “Enhanced photocurrent and conversion efficiency in thin-film microcrystalline silicon solar cells using periodically textured back reflectors with hexagonal dimple arrays,” *Applied Physics Letters*, vol. 101, no. 17, pp. 1–6, 2012.

[91] C. Trompoukis, O. El Daif, V. Depauw, I. Gordon, and J. Poortmans, “Photonic assisted light trapping integrated in ultrathin crystalline silicon solar cells by nanoimprint lithography,” *Applied Physics Letters*, vol. 101, no. 10, pp. 1–5, 2012.

[92] V. Preidel, D. Amkreutz, J. Haschke, M. Wollgarten, B. Rech, and C. Becker, “Balance of optical, structural, and electrical properties of textured liquid phase crystallized Si solar cells,” *Journal of Applied Physics*, vol. 117, no. 22, 2015.

[93] G. Köppel, B. Rech, and C. Becker, “Sinusoidal nanotextures for light manage-

ment in silicon thin-film solar cells," *Nanoscale*, vol. 8, no. 16, pp. 8722–8728, 2016.

[94] M. Smeets, K. Bittkau, F. Lentz, A. Richter, K. Ding, R. Carius, U. Rau, and U. W. Paetzold, "Post passivation light trapping back contacts for silicon heterojunction solar cells," *Nanoscale*, pp. 18726–18733, 2016.

[95] O. Kluth, B. Rech, L. Houben, S. Wieder, G. Schöpe, C. Beneking, H. Wagner, A. Löffl, and H. W. Schock, "Texture etched ZnO:Al coated glass substrates for silicon based thin film solar cells," *Thin Solid Films*, vol. 351, pp. 247–253, 1999.

[96] C. Zhang, M. Meier, A. Hoffmann, W. Zhang, K. Bittkau, G. Jost, U. W. Paetzold, M. Ermes, and T. Merdzhanova, "Influence of interface textures on light management in thin-film silicon solar cells with intermediate reflector," *IEEE Journal of Photovoltaics*, vol. 5, no. 1, pp. 33–39, 2015.

[97] E. Yablonovitch, "Statistical ray optics," *J. Opt. Soc. Am.*, vol. 72, pp. 899–907, Jul 1982.

[98] E. Yablonovitch and G. D. Cody, "Intensity enhancement in textured optical sheets for solar cells," *IEEE Transactions on Electron Devices*, vol. 29, pp. 300–305, Feb 1982.

[99] G. A. Valaskovic and G. H. Morrison, "A simple pneumatic pulling mechanism for the production of micropipettes," *Review of Scientific Instruments*, vol. 63, no. 8, pp. 4018–4019, 1992.

[100] G. A. Valaskovic, M. Holton, and G. H. Morrison, "Parameter control, characterization, and optimization in the fabrication of optical fiber near-field probes," *Applied Optics*, 1995.

[101] D. R. Turner, US patent 4,469,554.

[102] R. Stöckle, C. Fokas, V. Deckert, R. Zenobi, B. Sick, B. Hecht, and U. P. Wild, "High-quality near-field optical probes by tube etching," *Applied Physics Letters*, vol. 75, no. 2, pp. 160–162, 1999.

[103] P. Hoffmann, B. Dutoit, and R. P. Salathé, "Comparison of mechanically drawn and protection layer chemically etched optical fiber tips," *Ultramicroscopy*, vol. 61, no. 1-4, pp. 165–170, 1995.

[104] M. N. Islam, X. K. Zhao, A. A. Said, S. S. Mickel, and C. F. Vail, "High-efficiency and high-resolution fiber-optic probes for near field imaging and spectroscopy," *Applied Physics Letters*, vol. 71, no. 20, pp. 2886–2888, 1997.

[105] L. Novotny, D. W. Pohl, and B. Hecht, "Scanning near-field optical probe with ultrasmall spot size," *Optics Letters*, vol. 20, p. 970, may 1995.

[106] J. A. Veerman, A. M. Otter, L. Kuipers, and N. F. Van Hulst, "High definition aperture probes for near-field optical microscopy fabricated by focused ion beam milling," *Applied Physics Letters*, vol. 72, no. 24, pp. 3115–3117, 1998.

[107] F. Matthes, H. Brückl, and G. Reiss, "Near-field magneto-optical microscopy in collection and illumination mode," *Ultramicroscopy*, vol. 71, no. 1, pp. 243 – 248, 1998.

[108] A. J. Das, R. Shivanna, and K. Narayan, "Photoconductive NSOM for mapping optoelectronic phases in nanostructures," *Nanophotonics*, vol. 3, pp. 19–31, jan 2014.

[109] A. Kaneta, R. Fujimoto, T. Hashimoto, K. Nishimura, M. Funato, and Y. Kawakami, "Instrumentation for dual-probe scanning near-field optical microscopy," *Review of Scientific Instruments*, vol. 83, no. 8, 2012.

[110] S. Lehnen, U. W. Paetzold, M. Ermes, K. Bittkau, R. Carius, I. E. K. Photovoltaics, and F. J. Gmbh, "Analysis of light propagation in thin-film solar cells by dual-probe scanning near-field optical microscopy," in *2014 IEEE 40th Photovoltaic Specialist Conference (PVSC)*, pp. 3347–3351, IEEE, jun 2014.

[111] K. Bittkau and T. Beckers, "Near-field study of light scattering at rough interfaces of a-Si:H/μc-Si:H tandem solar cells," *physica status solidi (a)*, vol. 207, no. 3, pp. 661–666, 2010.

[112] U. W. Paetzold, S. Lehnen, K. Bittkau, U. Rau, and R. Carius, "Nanoscale observation of waveguide modes enhancing the efficiency of solar cells - Supporting Information," *Nano Letters*, vol. 14, no. 11, pp. 6599–6605, 2014.

[113] M. Ermes, S. Lehnen, Z. Cao, K. Bittkau, and R. Carius, "Simulation of light in-coupling through an aperture probe to investigate light propagation in a thin layer for opto-electronic application," *Proceedings of SPIE*, vol. 9526, p. 95260W, 2015.

[114] E. Betzig, J. K. Trautman, T. D. Harris, J. S. Weiner, and R. L. Kostelak, "Breaking the diffraction barrier: Optical microscopy on a nanometric scale," *Science*, vol. 251, pp. 1468–1470, 1991.

[115] T. Beckers, *Untersuchung optischer Nanostrukturen für die Photovoltaik mit Nahfeldmikroskopie*. Ph.D. thesis, RWTH Aachen University, 2010.

[116] C. Lienau, A. Richter, A. Klehr, and T. Elsaesser, "Near-field scanning optical microscopy of polarization bistable laser diodes," *Applied Physics Letters*, vol. 69, no. 17, pp. 2471–2473, 1996.

[117] A. C. Arias, J. D. MacKenzie, R. Stevenson, J. J. Halls, M. Inbasekaran, E. P. Woo, D. Richards, and R. H. Friend, "Photovoltaic performance and morphology of polyfluorene blends: A combined microscopic and photovoltaic investigation," *Macromolecules*, vol. 34, no. 17, pp. 6005–6013, 2001.

[118] T. Gotoh, Y. Yamamoto, Z. Shen, S. Ogawa, N. Yoshida, T. Itoh, and S. Nonomura, "Nanoscale Characterization of Microcrystalline Silicon Solar Cells by Scanning Near-Field Optical Microscopy," *Japanese Journal of Applied Physics*, vol. 48, p. 091202, sep 2009.

[119] E. Betzig, P. L. Finn, and J. S. Weiner, "Combined shear force and near-field scanning optical microscopy," *Applied Physics Letters*, vol. 60, no. 20, pp. 2484–2486, 1992.

[120] K. Karrai and R. D. Grober, "Piezoelectric tip-sample distance control for near field optical microscopes," *Applied Physics Letters*, vol. 66, no. 14, pp. 1842–1844, 1995.

[121] G. Behme, A. Richter, M. Süptitz, and C. Lienau, "Vacuum near-field scanning optical microscope for variable cryogenic temperatures," *Review of Scientific Instruments*, vol. 68, no. 9, pp. 3458–3463, 1997.

[122] A. G. Ruiter, K. O. Van Der Werf, J. A. Veerman, M. F. Garcia-Parajo, W. H. Rensen, and N. F. Van Hulst, "Tuning fork shear-force feedback," *Ultramicroscopy*, vol. 71, no. 1-4, pp. 149–157, 1998.

[123] M. Lippitz, M. Schüttler, H. Giessen, M. Born, and W. W. Rühle, "Bandwidth enhancement of a shear-force-controlled distance regulation in near-field microscopy," *Journal of Applied Physics*, vol. 86, no. 1, pp. 100–106, 1999.

[124] C. Durkan and I. V. Shvets, “Investigation of the physical mechanisms of shear-force imaging,” *Journal of Applied Physics*, vol. 80, no. 10, pp. 5659–5664, 1996.

[125] H. Brückl, F. Matthes, and G. Reiss, “Direct measurement of the oscillation amplitude and criteria for high-quality images in shear forcemicroscopy,” *Applied Physics A: Materials Science and Processing*, vol. 66, no. SUPPL. 1, pp. 345–348, 1998.

[126] K. Bittkau, T. Beckers, S. Fahr, C. Rockstuhl, F. Lederer, and R. Carius, “Nanoscale investigation of light-trapping in a-Si:H solar cell structures with randomly textured interfaces,” *Physica Status Solidi (A) Applications and Materials Science*, vol. 205, pp. 2766–2776, dec 2008.

[127] K. Yee, “Numerical solution of initial boundary value problems involving maxwell’s equations in isotropic media,” *IEEE Transactions on Antennas and Propagation*, vol. 14, no. 3, pp. 302–307, 1966.

[128] A. Taflove, “Application of the Finite-Difference Time-Domain Method to Sinusoidal Steady-State Electromagnetic-Penetration Problems,” *IEEE Transactions on Electromagnetic Compatibility*, vol. 22, no. 3, pp. 191–202, 1980.

[129] K. S. Kunz and R. J. Luebbers, *The Finite Difference Time Domain Method for Electromagnetics.* CRC Press, 1993.

[130] A. Taflove and S. C. Hagness, *Computational Electrodynamics: The Finite-Difference Time-Domain Method, Third Edition.* Artech House, 2005.

[131] S. D. Gedney, *Introduction to the Finite-Difference Time-Domain (FDTD) Method for Electromagnetics.* Morgan & Claypool Publishers, 2011.

[132] C. Rockstuhl, F. Lederer, C. Etrich, T. Pertsch, and T. Scharf, “Design of an Artificial Three-Dimensional Composite Metamaterial with Magnetic Resonances in the Visible Range of the Electromagnetic Spectrum,” *Physical Review Letters*, vol. 99, p. 017401, jul 2007.

[133] J. Dorfmüller, R. Vogelgesang, R. T. Weitz, C. Rockstuhl, C. Etrich, T. Pertsch, F. Lederer, and K. Kern, “Fabry-Pérot Resonances in One-Dimensional Plasmonic Nanostructures,” *Nano Letters*, vol. 9, no. 6, pp. 2372–2377, 2009.

[134] G. Mur, "Absorbing boundary conditions for the finite-difference approximation of the time-domain electromagnetic-field equations," *IEEE Transactions on Electromagnetic Compatibility*, vol. EMC-23, pp. 377–382, Nov 1981.

[135] O. M. Ramahi, "The concurrent complementary operators method for fdtd mesh truncation," *IEEE Transactions on Antennas and Propagation*, vol. 46, pp. 1475–1482, Oct 1998.

[136] J.-P. Berenger, "A perfectly matched layer for the absorption of electromagnetic waves," *Journal of Computational Physics*, vol. 114, no. 2, pp. 185 – 200, 1994.

[137] W. C. Chew and W. H. Weedon, "A 3d perfectly matched medium from modified maxwell's equations with stretched coordinates," *Microwave and Optical Technology Letters*, vol. 7, no. 13, pp. 599–604, 1994.

[138] F. L. Teixeira and W. C. Chew, "Systematic derivation of anisotropic pml absorbing media in cylindrical and spherical coordinates," *IEEE Microwave and Guided Wave Letters*, vol. 7, pp. 371–373, Nov 1997.

[139] S. D. Gedney, "An anisotropic perfectly matched layer-absorbing medium for the truncation of fdtd lattices," *IEEE Transactions on Antennas and Propagation*, vol. 44, pp. 1630–1639, Dec 1996.

[140] A. F. Oskooi, D. Roundy, M. Ibanescu, P. Bermel, J. D. Joannopoulos, and S. G. Johnson, "Meep: A flexible free-software package for electromagnetic simulations by the FDTD method," *Computer Physics Communications*, vol. 181, no. 3, pp. 687–702, 2010.

[141] M. Ermes, S. Lehnen, K. Bittkau, and R. Carius, "Investigation of the influence of the scanning probe on SNOM near-field images using rigorous simulations including the probe," *Proceedings of SPIE*, vol. 9132, p. 91320G, 2014.

[142] Z. Cao, S. Lehnen, R. Carius, and K. Bittkau, "High-resolution photocurrent mapping of thin-film solar cells using scanning near-field optical microscopy," *Proceedings of SPIE*, vol. 9890, p. 98900J, 2016.

[143] Z. Cao, M. Ermes, S. Lehnen, R. Carius, and K. Bittkau, "Effect of topography-dependent light coupling through a near-field aperture on the local photocurrent of a solar cell," *Phys. Chem. Chem. Phys.*, vol. 20, pp. 1098–1104,

2018.

[144] V. Smirnov, W. Böttler, A. Lambertz, H. Wang, R. Carius, and F. Finger, “Microcrystalline silicon n-i-p solar cells prepared with microcrystalline silicon oxide (μc-SiOx:H) n-layer,” in *Physica Status Solidi (C) Current Topics in Solid State Physics*, vol. 7, pp. 1053–1056, 2010.

[145] B. Hecht, H. Bielefeldt, Y. Inouye, D. W. Pohl, and L. Novotny, “Facts and artifacts in near-field optical microscopy,” *Journal of Applied Physics*, vol. 81, pp. 2492–2498, mar 1997.

[146] M. Smeets, V. Smirnov, M. Meier, K. Bittkau, R. Carius, U. Rau, and U. W. Paetzold, “Optimizing the geometry of plasmonic reflection grating back contacts for improved light trapping in prototype amorphous silicon thin-film solar cells,” *Proc. SPIE 9140, Photonics for Solar Energy Systems V,*, vol. 5, p. 91400D, nov 2014.

[147] M. Smeets, V. Smirnov, K. Bittkau, M. Meier, R. Carius, U. Rau, and U. W. Paetzold, “Angular dependence of light trapping in nanophotonic thin-film solar cells.,” *Optics express*, vol. 23, pp. A1575–88, nov 2015.

[148] B. Hopkins, W. Liu, A. E. Miroshnichenko, and Y. S. Kivshar, “Optically isotropic responses induced by discrete rotational symmetry of nanoparticle clusters,” *Nanoscale*, vol. 5, pp. 6395–6403, 2013.

[149] C. H. Seager, D. S. Ginley, and J. D. Zook, “Improvement of polycrystalline silicon solar cells with grain-boundary hydrogenation techniques,” *Applied Physics Letters*, vol. 36, no. 10, pp. 831–833, 1980.

[150] J. D. Zook, “Effects of grain boundaries in polycrystalline solar cells,” *Applied Physics Letters*, vol. 37, no. 2, pp. 223–226, 1980.

[151] C. R. M. Grovenor, “Grain boundaries in semiconductors,” *Journal of Physics C: Solid State Physics*, vol. 18, no. 21, p. 4079, 1985.

[152] J. Wong, J. Huang, S. Varlamov, M. A. Green, and M. Keevers, “The roles of shallow and deep levels in the recombination behavior of polycrystalline silicon on glass solar cells,” *Progress in Photovoltaics: Research and Applications*, 2012.

[153] J. Chen, T. Sekiguchi, D. Yang, F. Yin, K. Kido, and S. Tsurekawa, “Electron-

beam-induced current study of grain boundaries in multicrystalline silicon," *Journal of Applied Physics*, vol. 96, p. 5490, 11 2004.

[154] O. Gref, A.-M. Teodoreanu, R. Leihkauf, H. Lohrke, M. Kittler, D. Amkreutz, C. Boit, and F. Friedrich, "Grain boundary light beam induced current: A characterization of bonded silicon wafers and polycrystalline silicon thin films for diffusion length extraction," *Physica Status Solidi (a)*, vol. 10, pp. 1–10, 2016.

[155] J. Haschke, D. Amkreutz, and B. Rech, "Liquid phase crystallized silicon on glass: Technology, material quality and back contacted heterojunction solar cells," *Japanese Journal of Applied Physics*, vol. 55, p. 04EA04, apr 2016.

[156] J. Haschke, D. Amkreutz, L. Korte, F. Ruske, and B. Rech, "Towards wafer quality crystalline silicon thin-film solar cells on glass," *Solar Energy Materials and Solar Cells*, vol. 128, pp. 190–197, 2014.

[157] S. Kühnapfel, S. Gall, B. Rech, and D. Amkreutz, "Towards monocrystalline silicon thin films grown on glass by liquid phase crystallization," *Solar Energy Materials and Solar Cells*, vol. 140, pp. 86–91, 2015.

[158] S. Kühnapfel, S. Gall, P. Sonntag, N. Schäfer, and D. Abou-Ras, "Direct correlation of microstructure and device performance of liquid phase crystallized Si thin film solar cells on glass," *physica status solidi (RRL) - Rapid Research Letters*, vol. 10, no. 9, pp. 657–661, 2016.

[159] C. Becker, D. Amkreutz, T. Sontheimer, V. Preidel, D. Lockau, J. Haschke, L. Jogschies, C. Klimm, J. J. Merkel, P. Plocica, S. Steffens, and B. Rech, "Polycrystalline silicon thin-film solar cells: Status and perspectives," *Solar Energy Materials and Solar Cells*, vol. 119, pp. 112–123, 2013.

[160] O. Gabriel, T. Frijnts, N. Preissler, D. Amkreutz, S. Calnan, S. Ring, B. Stannowski, B. Rech, and R. Schlatmann, "Crystalline silicon on glass – interface passivation and absorber material quality," *Progress in Photovoltaics: Research and Applications*, vol. 24, no. 12, pp. 1499–1512, 2016.

[161] C. H. Seager, "The determination of grain-boundary recombination rates by scanned spot excitation methods," *Journal of Applied Physics*, vol. 53, no. 8, pp. 5968–5971, 1982.

[162] C. Donolato, "Theory of beam induced current characterization of grain boundaries in polycrystalline solar cells," *Journal of Applied Physics*, vol. 54, no. 3, pp. 1314–1322, 1983.

[163] C. Donolato and R. O. Bell, "Characterization of grain boundaries in polycrystalline solar cells using a computerized electron beam induced current system," *Review of Scientific Instruments*, vol. 54, no. 8, pp. 1005–1008, 1983.

[164] R. Corkish, T. Puzzer, A. B. Sproul, and K. L. Luke, "Quantitative interpretation of electron-beam-induced current grain boundary contrast profiles with application to silicon," *Journal of Applied Physics*, vol. 84, no. 10, pp. 5473–5481, 1998.

[165] G. Micard, G. Hahn, A. Zuschlag, S. Seren, and B. Terheiden, "Quantitative evaluation of grain boundary activity in multicrystalline semiconductors by light beam induced current: An advanced model," *Journal of Applied Physics*, vol. 108, no. 3, pp. 1–13, 2010.

[166] M. A. Green, "Self-consistent optical parameters of intrinsic silicon at 300 K including temperature coefficients," *Solar Energy Materials and Solar Cells*, vol. 92, no. 11, pp. 1305–1310, 2008.

[167] J. Marek, "Light-beam-induced current characterization of grain boundaries," *Journal of Applied Physics*, vol. 55, no. 2, pp. 318–326, 1984.

[168] W. D. Sawyer, "An improved method of light-beam-induced current characterization of grain boundaries," *Journal of Applied Physics*, vol. 59, no. 7, pp. 2361–2363, 1986.

[169] A. Mittiga and M. Capizzi, "Fourier transform analysis of light-beam-induced current profiles," *Journal of Applied Physics*, vol. 62, no. 8, pp. 3443–3445, 1987.

[170] H. J. Fitting, H. Glaefeke, and W. Wild, "Electron penetration and energy transfer in solid targets," *Physica Status Solidi (a)*, vol. 43, no. 1, pp. 185–190, 1977.

[171] C. Donolato, "An analytical model of SEM and STEM charge collection images of dislocations in thin semiconductor layers: I. Minority carrier generation, diffusion, and collection," *Physica Status Solidi (a)*, vol. 65, no. 2, pp. 649–

658, 1981.

[172] O. Von Roos and K. L. Luke, “Analysis of the electron-beam-induced current of a polycrystalline p-n junction when the diffusion lengths of the material on either side of a grain boundary differ,” *Journal of Applied Physics*, vol. 55, no. 12, pp. 4275–4279, 1984.

[173] T. Markvart, “Relationship between Dark Carrier Distribution and Photogenerated Carrier Collection in Solar Cells,” *IEEE Transactions on Electron Devices*, vol. 43, no. 6, pp. 1034–1036, 1996.

[174] C. Donolato, “A reciprocity theorem for charge collection,” *Applied Physics Letters*, vol. 46, no. 3, pp. 270–272, 1985.

[175] M. A. Green, “Generalized relationship between dark carrier distribution and photocarrier collection in solar cells,” *Journal of Applied Physics*, vol. 81, no. 1, pp. 268–271, 1997.

[176] M. Schöfthaler, U. Rau, W. Fussel, and J. H. Werner, “Optimization of the back contact geometry for high efficiency solar cells,” in *Conference Record of the Twenty Third IEEE Photovoltaic Specialists Conference - 1993*, p. 315, 1993.

[177] M. Schöfthaler, U. Rau, and J. H. Werner, “Direct observation of a scaling effect on effective minority carrier lifetimes,” *Journal of Applied Physics*, vol. 76, no. 7, pp. 4168–4172, 1994.

[178] D. Amkreutz, J. Haschke, T. Häring, F. Ruske, and B. Rech, “Conversion efficiency and process stability improvement of electron beam crystallized thin film silicon solar cells on glass,” *Solar Energy Materials and Solar Cells*, vol. 123, pp. 13–16, 2014.

[179] S. Kühnapfel, J. Huang, A. Teal, H. Kampwerth, D. Amkreutz, S. Gall, and S. Varlamov, “Lifetime analysis of laser crystallized silicon films on glass,” *Journal of Applied Physics*, vol. 118, no. 5, 2015.

[180] M. Berginski, J. Hüpkes, M. Schulte, G. Schöpe, H. Stiebig, B. Rech, and M. Wuttig, “The effect of front ZnO:Al surface texture and optical transparency on efficient light trapping in silicon thin-film solar cells,” *Journal of Applied Physics*, vol. 101, no. 7, p. 074903, 2007.

[181] M. Python, O. Madani, D. Dominé, F. Meillaud, E. Vallat-Sauvain, and C. Ballif, "Influence of the substrate geometrical parameters on microcrystalline silicon growth for thin-film solar cells," *Solar Energy Materials and Solar Cells*, vol. 93, no. 10, pp. 1714–1720, 2009.

[182] H. B. Li, R. H. Franken, J. K. Rath, and R. E. Schropp, "Structural defects caused by a rough substrate and their influence on the performance of hydrogenated nano-crystalline silicon n-i-p solar cells," *Solar Energy Materials and Solar Cells*, vol. 93, no. 3, pp. 338–349, 2009.

[183] G. Bugnon, G. Parascandolo, T. Söderström, P. Cuony, M. Despeisse, S. Hänni, J. Holovský, F. Meillaud, and C. Ballif, "A new view of microcrystalline silicon: The role of plasma processing in achieving a dense and stable absorber material for photovoltaic applications," *Advanced Functional Materials*, vol. 22, pp. 3665–3671, sep 2012.

[184] J. Hüpkes, J. Owen, E. Bunte, H. Zhu, S. Pust, J. Worbs, and G. Jost, "New texture etching of zinc oxide: Tunable light trapping for si thin film solar cells," *Proceedings of the 25th European Photovoltaic Solar Energy Conference*, pp. 3224–3227, 01 2010.

[185] C. Zhang, M. Meier, A. Lambertz, V. Smirnov, B. Holländer, A. Gordijn, and T. Merdzhanova, "Optical and electrical effects of p-type c-SiOx: H in thin-film silicon solar cells on various front textures," *International Journal of Photoenergy*, vol. 2014, 2014.

[186] S. Hänni, D. T. Alexander, L. Ding, G. Bugnon, M. Boccard, C. Battaglia, P. Cuony, J. Escarré, G. Parascandolo, S. Nicolay, M. Cantoni, M. Despeisse, F. Meillaud, and C. Ballif, "On the interplay between microstructure and interfaces in high-efficiency microcrystalline silicon solar cells," *IEEE Journal of Photovoltaics*, vol. 3, no. 1, pp. 11–16, 2013.

[187] M. Sever, B. Lipovšek, J. Krč, A. Čampa, G. Sánchez Plaza, F. J. Haug, M. Duchamp, W. Soppe, and M. Topič, "Combined model of non-conformal layer growth for accurate optical simulation of thin-film silicon solar cells," *Solar Energy Materials and Solar Cells*, vol. 119, pp. 59–66, 2013.

[188] M. Sever, J. Krč, and M. Topič, "Prediction of defective regions in optimisation

of surface textures in thin-film silicon solar cells using combined model of layer growth," *Thin Solid Films*, vol. 573, pp. 176–184, 2014.

[189] D. Y. Kim, R. Santbergen, K. Jäger, M. Sever, J. KrcÌŒ, M. TopicÌŒ, S. Hänni, C. Zhang, A. Heidt, M. Meier, R. A. C. M. M. Van Swaaij, and M. Zeman, "Effect of substrate morphology slope distributions on light scattering, nc-Si:H film growth, and solar cell performance," *ACS Applied Materials and Interfaces*, vol. 6, no. 24, pp. 22061–22068, 2014.

[190] D. Y. Kim, S. Hänni, J. W. Schüttauf, R. A. Van Swaaij, and M. Zeman, "Quantification of Valleys of Randomly Textured Substrates as a Function of Opening Angle: Correlation to the Defect Density in Intrinsic nc-Si:H," *ACS Applied Materials and Interfaces*, vol. 8, no. 32, pp. 20660–20666, 2016.

[191] M. Grätzel, "The light and shade of perovskite solar cells," *Nature Materials*, vol. 13, no. 9, pp. 838–842, 2014.

[192] P. Gao, M. Grätzel, and M. K. Nazeeruddin, "Organohalide lead perovskites for photovoltaic applications," *Energy and Environmental Science*, vol. 7, no. 8, pp. 2448–2463, 2014.

[193] M. A. Green, A. Ho-Baillie, and H. J. Snaith, "The emergence of perovskite solar cells," *Nature Photonics*, vol. 8, no. 7, pp. 506–514, 2014.

[194] S. De Wolf, J. Holovsky, S.-J. Moon, P. Löper, B. Niesen, M. Ledinsky, F.-J. Haug, J.-H. Yum, and C. Ballif, "Organometallic halide perovskites: Sharp optical absorption edge and its relation to photovoltaic performance," *The Journal of Physical Chemistry Letters*, vol. 5, no. 6, pp. 1035–1039, 2014. PMID: 26270984.

[195] G. Xing, N. Mathews, S. S. Lim, N. Yantara, X. Liu, D. Sabba, M. Grätzel, S. Mhaisalkar, and T. C. Sum, "Low-temperature solution-processed wavelength-tunable perovskites for lasing," *Nature Materials*, vol. 13, no. 5, pp. 476–480, 2014.

[196] J. H. Noh, S. H. Im, J. H. Heo, T. N. Mandal, and S. I. Seok, "Chemical management for colorful, efficient, and stable inorganic-organic hybrid nanostructured solar cells," *Nano Letters*, vol. 13, no. 4, pp. 1764–1769, 2013.

[197] A. Kojima, K. Teshima, Y. Shirai, and T. Miyasaka, "Organometal halide

perovskites as visible-light sensitizers for photovoltaic cells," *Journal of the American Chemical Society*, vol. 131, no. 17, pp. 6050–6051, 2009.

[198] Y. Zhou, A. L. Vasiliev, W. Wu, M. Yang, S. Pang, K. Zhu, and N. P. Padture, "Crystal morphologies of organolead trihalide in mesoscopic/planar perovskite solar cells," *Journal of Physical Chemistry Letters*, vol. 6, no. 12, pp. 2292–2297, 2015.

[199] Y. Shao, Y. Fang, T. Li, Q. Wang, Q. Dong, Y. Deng, Y. Yuan, H. Wei, M. Wang, A. Gruverman, J. Shield, and J. Huang, "Grain boundary dominated ion migration in polycrystalline organic-inorganic halide perovskite films," *Energy Environ. Sci.*, vol. 9, pp. 1752–1759, 2016.

[200] Y. Kutes, Y. Zhou, J. L. Bosse, J. Steffes, N. P. Padture, and B. D. Huey, "Mapping the Photoresponse of CH3NH3PbI3 Hybrid Perovskite Thin Films at the Nanoscale," *Nano letters*, vol. 16, pp. 3434–3441, apr 2016.

[201] Q. Chen, H. Zhou, Z. Hong, S. Luo, H.-S. Duan, H.-H. Wang, Y. Liu, G. Li, and Y. Yang, "Planar heterojunction perovskite solar cells via vapor-assisted solution process," *Journal of the American Chemical Society*, vol. 136, no. 2, pp. 622–625, 2014. PMID: 24359486.

[202] D. W. deQuilettes, W. Zhang, V. M. Burlakov, D. J. Graham, T. Leijtens, A. Osherov, V. Bulovic, H. J. Snaith, D. S. Ginger, and S. D. Stranks, "Photo-induced halide redistribution in organic-inorganic perovskite films," *Nature Communications*, vol. 7, 2016.

List of Publications

1. M. Ermes, S. Lehnen, **Z. Cao**, K. Bittkau, and R. Carius, "Simulation of light in-coupling through an aperture probe to investigate light propagation in a thin layer for opto-electronic application," *Proceedings of SPIE*, vol. 9526, p. 95260W, 2015.
2. **Z. Cao**, S. Lehnen, R. Carius, and K. Bittkau, "High-resolution photocurrent mapping of thin-film solar cells using scanning near-field optical microscopy," *Proceedings of SPIE*, vol. 9890, p. 98900J, 2016.
3. K. Bittkau, S. Lehnen, **Z. Cao**, and R. Carius, "Electro-optical characterization of solar cells with scanning near-field optical microscopy," *2016 IEEE 43rd Photovoltaic Specialists Conference (PVSC)*, pp. 1317 − 1322, 2016.
4. **Z. Cao**, M. Ermes, S. Lehnen, R. Carius, and K. Bittkau, "Effect of topography-dependent light coupling through a near-field aperture on the local photocurrent of a solar cell," *Phys. Chem. Chem. Phys.*, vol. 20, pp. 1098 − 1104, 2018.

Acknowledgments

Finally, it is time to offer up my infinite thanks to the people who, in one way or another, have made this wonderful journey possible.

I would like to start by thanking my doctoral supervisor **Prof. Dr. Thomas Taubner** for his genuine interest in my work. Whenever we met for exchange, be it in the plasmonics meeting, or in a progress report session, his never ceasing enthusiasm for science (especially for nano-optics, of course) and positive attitude have always been inspiring and encouraging.

I'll be forever thankful to **Prof. Dr. Uwe Rau**, who is also the second examiner of this thesis, for the opportunity to conduct my doctoral research at the IEK-5:Photovoltaics. His valuable, sometimes critical inputs have greatly improved the quality of this thesis, especially from a quantitative perspective. The electrical modeling he has contributed constitutes an integral part of the Chapter 5.

My biggest debt of gratitude goes without a doubt to my direct supervisor **Dr. Karsten Bittkau**: for the great freedom he granted me to explore various research ideas and for always being available for discussions, be it about theoretical questions or about experimental challenges. Thanks to his distinguished expertise in optics, he was always able to help when the sometimes truly puzzling results from the optical simulations were causing me serious headaches. I will also miss our (sometimes lengthy) conversations about all kinds of topics in life (travels, politics, weather in Hamburg...you name it) immensely, although I did miss my last bus back to Aachen afterward for a few times:-)

I obviously also owe a tremendous debt of gratitude to my SNOM colleagues **Dr. Stephan Lehnen** and **Dr. Alexander Markus Ermes**. Stephan has helped me in so many aspects with regard to the experiment. From the setup to the measurement, I have profited enormously from his profound knowledge about all

the trickiness, the dos and don’ts around SNOM. Markus, on the other hand, has paved the way for all the optical simulations I performed in this work with his preceding development of the simulation software. Heartfelt thanks go as well to **Prof. Dr. Reinhard Carius** for generously sharing his comprehensive knowledge about experimental setup and characterization techniques, for the dedicated proof-reading of my first paper and for a couple of surprise visits late Friday afternoon in the SNOM lab. Special thanks also go to **Prof. Dr. Thomas Kirchartz** (when I look back to the very beginning of this journey, well, actually even earlier than the beginning...) for forwarding my initial application to Karsten, which opened up the possibility to get in touch with Karsten at the first place, and for introducing me to the exciting world of perovskite solar cells. Additionally, gigantic thanks to all of you, as well as to **Michael Smeets** and **Dr. André Hoffmann**, for plenty of constructive and fruitful discussions.

I am deeply grateful for the abundant technical help I received during the years, which were instrumental for the success of this work. I thank **Ulrike Gerhards**, **Hildegard Siekmann** and **Joachim Kirchhoff** for the preparation of the μc-Si:H thin-film solar cells which contributed to two of the three result chapters of this thesis, **Josef Klomfaß** for the numerous advice with special regard to electronic components, **Oliver Thimm** for the constantly friendly helpfulness whenever I was showing up at his door with a technical issue or purchase orders for various lab supplies, **Hassan Jaajouhi** for building the electronic parts when they are not available for purchase, **Markus Hülsbeck** for providing diverse optical components for the SNOM setup and for the Raman measurements, **Pascal Foucart** for the AFM measurements of the textured μc-Si:H thin-film solar cell, **Sabine Kaspers** for always being helpful whenever I needed some parts from the electronics lab, **Dr. Benjamin Klingebiel** for providing me with just the right chemicals for various purposes in the operation of SNOM, **Christoph Zahren** for the instruction to the solar simulator and **Wilfried Reetz** for the instruction to the LED-QE measurement system. Huge thanks also go to **Dr. Florian Lentz**, **Sandra Moll**, **Gunnar Schöpe**, **Frank Pennartz**, **Irina Kühn** and **Ralf Schmitz** for all the technical advice and assistance now and then. Furthermore, I would like to thank **Petra Lorbach** ,**Andrea Mülheims**, **Astrid Nogga** and **Gina Frings** for all kinds of administrative support throughout the years.

I want to thank the group of **Prof. Dr. Christiane Becker** from the Helmholtz-Zentrum Berlin for providing the flat LPC thin-film solar cell for the SNOM local photocurrent measurements, which vividly demonstrated the sensitivity of this characterization method to the electrical effects. Many thanks to **David Grabowski** for the preparation of the perovskite solar cells and **Dr. Manuel Pomaska** for providing the c-Si solar cells for trial measurements with SNOM, although the results didn't make it into this thesis, unfortunately.

From the bottom of my heart, I would like to thank all my friends and peers at the IEK-5 for the lunches together, the lovely coffee breaks, the enjoyable times outside of the institute, the cozy chats, the rides home after work, the cozy chats during the rides home after work and many, many more. **Michael Smeets**, **Florian Staub**, **Jinane Haddad**, **Dr. Paolo Cadiz-Bedini**, **Dr. Félix Urbain**, **Beatrix Blank**, **Dr. Weiyuan Duan**, **Yong Liu**, **Huimin Li**, **Samia Nadi**, **Dr. Alexei Richter**, **Dr. Manuel Pomaska**, **Dr. Claudia Maurer**, **Dr. Jan Mock**, **Dr. Jan Flohre**, **Dr. Vito Huhn**, **Christine Leidinger**, **Niloofar Hamzelui** and **Aryak Singh**: thank you so much!

I would like to express my profound gratitude to the amazing graduate school **HITEC** for a variety of excellent training programs and for financing the two-week International Summer University on Energy, as well as the trip to visit my external mentor in China. My sincere appreciation also goes to my external mentor **Dr. Rong Yang** for the warm welcome, the organization of my visiting programs and for granting me a deep and extensive insight into the everyday operations of PV manufacturer. I would also like to acknowledge the financial support from the European Union Seventh Framework Programme (FP7/2007-2013) under grant agreement no. 609788 (CHEETAH).

A special brand of thanks goes to THE special one: **Jianing Liu**. There are infinite reasons for me to be grateful to have you in my life. Still, every day a new one comes to mind.

Finally, my wholehearted thanks and tons of love to my family. My parents **Min Cao** and **Yiyong Liu**, thank you for EVERYTHING! My dearest sister **Lili Cao**, you're the best! I know we fight a lot, but hey, what are brother and sister for, right?;-)

Eidesstattliche Erklärung

Zhao Cao

erklärt hiermit, dass diese Dissertation und die darin dargelegten Inhalte die eigenen sind und selbstständig, als Ergebnis der eigenen originären Forschung, generiert wurden.

Hiermit erkläre ich an Eides statt

1. Diese Arbeit wurde vollständig oder größtenteils in der Phase als Doktorand dieser Fakultät und Universität angefertigt;
2. Sofern irgendein Bestandteil dieser Dissertation zuvor für einen akademischen Abschluss oder eine andere Qualifikation an dieser oder einer anderen Institution verwendet wurde, wurde dies klar angezeigt;
3. Wenn immer andere eigene- oder Veröffentlichungen Dritter herangezogen wurden, wurden diese klar benannt;
4. Wenn aus anderen eigenen- oder Veröffentlichungen Dritter zitiert wurde, wurde stets die Quelle hierfür angegeben. Diese Dissertation ist vollständig meine eigene Arbeit, mit der Ausnahme solcher Zitate;
5. Alle wesentlichen Quellen von Unterstützung wurden benannt;
6. Wenn immer ein Teil dieser Dissertation auf der Zusammenarbeit mit anderen basiert, wurde von mir klar gekennzeichnet, was von anderen und was von mir selbst erarbeitet wurde;
7. Ein Teil oder Teile dieser Arbeit wurden zuvor veröffentlicht und zwar in:

   [1] **Z. Cao**, S. Lehnen, R. Carius, and K. Bittkau, “High-resolution photocurrent mapping of thin-film solar cells using scanning near-field optical microscopy,” *Proceedings of SPIE*, vol. 9890, p. 98900J, 2016.

[2] **Z. Cao**, M. Ermes, S. Lehnen, R. Carius, and K. Bittkau, “Effect of topography-dependent light coupling through a near-field aperture on the local photocurrent of a solar cell,” *Phys. Chem. Chem. Phys.*, vol. 20, pp. 1098 – 1104, 2018.

Aachen, den 27. August 2020

Band / Volume 522
Towards a Generalized Framework for the Analysis of Solar Cell Performance based on the Principle of Detailed Balance
B. J. Blank (2020), iv, 142 pp
ISBN: 978-3-95806-514-7

Band / Volume 523
A Robust Design of a Renewable European Energy System Encompassing a Hydrogen Infrastructure
D. G. Çağlayan (2020), xxii, 312 pp
ISBN: 978-3-95806-516-1

Band / Volume 524
Control and Optimization of a Lorentz Force Based Actuator System for External Flow
M. F. Seidler (2020), xii, 136 pp
ISBN: 978-3-95806-518-5

Band / Volume 525
ETV Online Tagung 2020
Industrielle Groß- und Hochtemperaturwärmepumpen im Energiesystem
D. Stolten, G. Markowz (Hrsg.) (2020), ca. 71 pp
ISBN: 978-3-95806-519-2

Band / Volume 526
Atmospheric Trace Gas Measurements Using Chemical Ionisation Time-of-Flight Mass Spectrometry
Y. Li (2020), xi, 110 pp
ISBN: 978-3-95806-520-8

Band / Volume 527
Uranium accumulation in agricultural soils as derived from long-term phosphorus fertilizer applications
Y. Sun (2020), XII, 136 pp
ISBN: 978-3-95806-521-5

Band / Volume 528
Entwicklung von Schutzschichten für nicht-oxidische Faserverbundwerkstoffe
M. Wolf (2021), VI, 150, 2 pp
ISBN: 978-3-95806-524-6

Band / Volume 529
Mechanical reliability and oxygen permeation of $Ce_{0.8}Gd_{0.2}O_{2-\delta}$-$FeCo_2O_4$ dual phase membranes
F. Zeng (2021), IV, VI, 222 pp
ISBN: 978-3-95806-527-7

Band / Volume 530
Capacitance-Based Methods to Study Charge Transport and Recombination in Organic Solar Cells
I. Zonno (2021), vi, 153 pp
ISBN: 978-3-95806-528-4

Band / Volume 531
Einflüsse von Klimavariabilität und -wandel auf Ausbau und Erzeugung im Europäischen Stromsystem
F. P. Gotzens (2021), XXIII, 231 pp
ISBN: 978-3-95806-530-7

Band / Volume 532
Weltweite Infrastruktur zur Wasserstoffbereitstellung auf Basis erneuerbarer Energien
P.-M. Heuser (2021), VII, 231 pp
ISBN: 978-3-95806-531-4

Band / Volume 533
Mechanische Eigenschaften von katalysatorbeschichteten Membranen für die Polymer-Elektrolyt-Membran Elektrolyse
E. Borgardt (2021), viii, 181 pp
ISBN: 978-3-95806-533-8

Band / Volume 534
Techno-economic Assessment of Hybrid Post-combustion Carbon Capture Systems in Coal-fired Power Plants and Steel Plants
Y. Wang (2021), IV, xx, 230 pp
ISBN: 978-3-95806-545-1

Band / Volume 535
Wissenschaftliche Begleitstudie der Wasserstoff Roadmap Nordrhein-Westfalen
S. Cerniauskas, P. Markewitz, J. Linßen, F. Kullmann, T. Groß,
P. Lopion, P-M. Heuser, T. Grube, M. Robinius und D. Stolten
(2021), IV, 89 pp
ISBN: 978-3-95806-547-5

Band / Volume 536
High-Resolution Photocurrent Mapping of Thin-Film Silicon Solar Cells Using Scanning Near-Field Optical Microscopy
Z. Cao (2021), xiii, 148 pp
ISBN: 978-3-95806-548-2

Weitere ***Schriften des Verlags im Forschungszentrum Jülich*** unter
http://wwwzb1.fz-juelich.de/verlagextern1/index.asp

Energie & Umwelt / Energy & Environment
Band / Volume 536
ISBN 978-3-95806-548-2

Mitglied der Helmholtz-Gemeinschaft

JÜLICH
Forschungszentrum